HOKKAIDO UNIVERSITY

Title	Effect of increased near-fault fracture stiffness on seismic source parameters of induced seismicity
Author(s)	Mingwei, Gang
Degree Grantor	北海道大学
Degree Name	博士(工学)
Dissertation Number	甲第16856号
Issue Date	2026-03-25
DOI	https://doi.org/10.14943/doctoral.k16856
Doc URL	https://hdl.handle.net/2115/99701
Type	doctoral thesis
File Information	Mingwei_Gang.pdf, 全文

Hokkaido University Collection of Scholarly and Academic Papers : HUSCAP

Effect of increased near-fault fracture stiffness on seismic source parameters of induced seismicity

Dissertation for the Degree of Doctor of Engineering

Mingwei Gang

Division of Sustainable Resources Engineering
Graduate School of Engineering
Hokkaido University, Japan

January 2026

Effect of increased near-fault fracture stiffness on seismic source parameters of induced seismicity
(断層近傍のき裂剛性増加が誘発地震の震源パラメータに与える影響)

By

Mingwei Gang

A dissertation submitted in partial fulfillment of the requirements for the Degree of Doctor of Engineering

Division of Sustainable Resources Engineering

Graduate School of Engineering

Hokkaido University

Japan

January 2026

Copyright 2026

by

Mingwei Gang

ALL RIGHTS RESERVED

Declaration

I, Mingwei Gang, declare that this dissertation titled "Numerical and analytical studies on increasing near-fault fracture stiffness to control induced seismicity" is an original report of my study and was carried out entirely under the supervision of Professor Jun-ichi Kodama. It was written by me and references have been duly provided on all supporting literature and resources. I also declare that this dissertation has not been submitted previously, either in whole or part, for application of any degree.

Acknowledgements

As I look back, it has now been almost four years since I came to Japan. These years have taken me from being a new graduate in an unfamiliar country to standing at the end of my doctoral journey. This dissertation is not only the record of my research, but also a milestone in my life, filled with effort, challenges, and growth. I would like to take this opportunity to express my sincere gratitude to all those who have supported me along the way.

First and foremost, I wish to express my deepest gratitude to my parents. Although we have been separated by distance, your unconditional love, understanding, and constant encouragement have always been my greatest strength. Without your support and trust, I would never have had the courage to study abroad or the perseverance to complete this work.

I am profoundly grateful to my supervisor, Professor Jun-ichi Kodama, for his continuous guidance, patience, and encouragement throughout my doctoral studies. He has not only provided invaluable advice on research, but also taught me how to think logically, approach problems independently, and maintain humility as a researcher. I am also sincerely thankful to Professor Atsushi Sainoki for his insightful comments, careful guidance, and generous support. His expertise and warm supervision greatly helped me deepen my understanding of rock mechanics and numerical modelling.

I would also like to thank all the members of the Global Development Information (GDI) Laboratory at Hokkaido University and Underground Space Engineering Laboratory at Kumamoto University. The stimulating discussions, technical assistance, and friendly atmosphere in the laboratory made my research life both productive and enjoyable. I am grateful to the professors, staff, and fellow students who helped me with experiments, simulations, and daily life in Japan.

Finally, I would like to express my heartfelt thanks to my friends, both in Japan and abroad. Your companionship, encouragement, and understanding have given me strength in difficult times and joy in ordinary days. The memories we share will always remain a precious part of my life.

To everyone who has supported me during this journey, directly or indirectly, I offer my sincere thanks. This dissertation is dedicated to all of you.

Abstract

Induced seismicity associated with underground resource extraction, geothermal development, and fluid-injection operations poses significant risks to mine safety and infrastructure. In deep mines, seismic events often occur not only near active excavations but also at considerable distances, largely due to the complex mechanical behavior and the heterogeneous stress conditions within natural structures. Although mitigation methods such as microseismic monitoring, destress blasting, hydraulic fracturing, and traffic-light systems are widely applied, their effectiveness remains limited because they do not explicitly consider the strong stress heterogeneity caused by these geological structures.

Especially faults, consisting of a narrow core and a wider damage zone with densely fractured rock, play a central role in stress redistribution and seismic slip. Prior theoretical, numerical, and experimental studies suggest that increasing the stiffness of surrounding rock can reduce radiated seismic energy and thus suppress seismic intensity. However, a comprehensive framework that integrates experimental evidence of damage-zone mechanical heterogeneity with multiscale numerical modeling is still lacking. In particular, the internal stress-strain states within fault damage zones and their implications for stiffness-based mitigation strategies remain insufficiently understood, mainly due to the difficulty of characterizing fractures embedded within the rock mass. To address these gaps, this study examines the mechanical complexity and heterogeneous stress-strain states within fault damage zones through a new experimental method, while investigating the effectiveness of enhancing near-fault fracture stiffness in controlling induced seismicity using two complementary numerical modeling approaches. The specific contents of each chapter are as follows:

Chapter 1 introduces the fundamental background and significance of induced seismicity in mining and other subsurface engineering fields. The limitations of existing mitigation approaches are reviewed. This chapter also presents the objectives and overall structure of the thesis.

Chapter 2 establishes the theoretical basis for a stiffness-based mitigation strategy using the slip-weakening framework. The relationship between system stiffness, fault slip behavior, and seismically radiated energy is examined, and a parametric analysis is conducted to verify the theoretical feasibility of reducing seismic intensity through fracture stiffness enhancement. This chapter provides the theoretical foundation for the subsequent numerical investigations.

Chapter 3 presents experimental investigations to demonstrate the internal mechanical complexity of fault damage zones. An X-ray computed tomography (CT)- and digital image correlation (DVC)-based experimental methodology using 3D-printed rock-like specimens is developed to visualize and quantify heterogeneous internal strain states within damage zone analogues. The experimental results are used to characterize deformation patterns and strain distributions within fractured media, thereby providing physical evidence of damage zone heterogeneity and a realistic basis for the numerical modeling approaches adopted in the subsequent chapters.

Chapter 4 develops a discrete element method (DEM) model that explicitly represents a damage zone using a statistically generated discrete fracture network (DFN). Fractures are modeled as disk-shaped discontinuities with independently assigned normal and shear stiffness. Parametric studies are conducted to investigate the effects of fracture stiffness, as well as the individual contributions of normal and shear stiffness, on fault slip process and seismic source parameters. This chapter provides fracture-scale insight that supports the stiffness-based mitigation strategy.

Chapter 5 introduces a mine-scale continuum numerical model based on crack tensor theory, in which the heterogeneous damage zone is represented as an equivalent anisotropic continuum. To overcome the computational limitations of DEM for damage zones with dense fractures, this model reproduces heterogeneous in-situ stress conditions and mining-induced fault slip, enabling systematic evaluation of stiffness-based mitigation effectiveness at the macroscopic scale. Using this framework, the influence of fracture stiffness, fracture density and distance from the fault on seismic source parameters is quantitatively studied.

Chapter 6 provides an overall synthesis of the main outcomes of this thesis including discussion on their implications for seismic hazard mitigation in deep underground settings. The benefits and limitations of the stiffness-based approach, as well as those of the numerical and experimental methods used, are also summarized. Furthermore, this chapter outlines future research directions and potential applications of stiffness enhancement in practical mine design and seismic risk management.

Contents

Acknowledgements i

Abstract ii

Contents iv

List of Figures vii

List of Tables ix

1. Introduction 1

1.1 Background 1

1.2 Literature review 1

1.2.1 Mitigation methods for induced seismicity 1

1.2.2 Heterogeneity of damage zones and experimental challenges 2

1.2.3 Numerical modeling approaches for heterogeneous fault damage zones 3

1.3 Objectives 5

1.4 Content of research 6

2. Theoretical basis for stiffness-based mitigation strategy 9

2.1 Inrtoduction 9

2.2 Slip-weakening concept 9

2.3 Theoretical verification 10

3. Experimental investigation of heterogeneous stress-strain states in damage zone using 3D-printed specimens 15

3.1 Introduction 15

3.2 Sample preparation and experimental design 15

3.2.1 Preparation of samples containing internal prefabricated discontinuities 15

3.2.2 3DP manufacturing procedure of rock-like samples 18

3.2.3 CT-scanning set-up 19

3.3 Experimental results and discussion 22

3.3.1 Accuracy verification 22

3.3.2 Calculation methodology 24

3.3.3 Strain distribution in damage zone 26

3.4 Concluding marks 29

4. Numerical investigations on the impacts of fracture stiffness on seismic source parameters at the fracture scale 31

4.1 Introduction 31
4.2 Numerical model with discrete fracture network 31
4.3 Verification of the model 33
4.4 Input parameters 35
4.5 Numerical analysis 35
4.5.1 Analysis procedure 35
4.5.2 Calculation of seismic source parameters 37
4.6 Simulation results and discussion 37
4.6.1 Effect of fracture stiffness on seismic source parameters 37
4.6.2 Effect of fracture stiffness on slip process 41
4.6.3 Comparative influence of normal and shear fracture stiffness 41
4.7 Concluding remarks 43

5. Numerical investigations on the impacts of near-fault fracture stiffness on seismic source parameters at the mine scale 44

5.1 Introduction 44
5.2 Distribution of fractures in a fault damage zone 44
5.3 Generation of discrete fracture network (DFN) model 45
5.4 Overall Procedure 47
5.5 Model input parameters 50
5.6 Fault damage zone cases 52
5.7 Numerical analysis 54
5.7.1 Analysis procedure 54
5.7.2 Calculation of seismic source parameters 56
5.8 Simulation results 58
5.8.1 Effect of fracture stiffness for each case and its verification 58
5.8.2 Results of model parametric study 63
5.8.3 Effect of fracture stiffness using different near-fault fracture densities 64
5.8.4 Effect of fracture stiffness using different distances from the fault 66
5.8.5 Effect of fracture stiffness using different thicknesses of enhanced fractures 67

5.9 Discussion 70
5.9.1 Potential for the proposed method to mitigate the intensity of seismicity 70
5.9.2 The role of the damage zone strength and stiffness 71
5.10 Concluding remarks 72
6. Conclusions and recommendations 74
6.1 Conclusions 74
6.2 Recommendations 75
References 77

List of Figures

Fig. 2.1: Schematic representation of energy release based on slip-weakening model. 10
Fig. 2.2: Theoretical verification for (a) base case, (b) doubled initial stiffness, (c) static friction of 0.7, and (d) kinetic friction of 0.3 14
Fig. 3.1: Specimens with prefabricated flaws by casting method. 16
Fig. 3.2: Design of specimens with various fracture patterns. 17
Fig. 3.3: Composition of 3DP specimens. 18
Fig. 3.4: Printing process of 3DP specimens. 19
Fig. 3.5: Experimental device set-up. 20
Fig. 3.6: Loading stage. 21
Fig. 3.7: Cross-sectional images of 3DP specimen. 22
Fig. 3.8: Geometry and internal discontinuity of the 3D-printed specimen. 23
Fig. 3.9: CT images acquired at different loading stages. 24
Fig. 3.10: Calculation region and deviatoric strain distribution. 24
Fig. 3.11: Hierarchical subvolume selection from X-ray CT images. 26
Fig. 3.12: Three-dimensional strain distributions in cylindrical specimens with different damage-zone fracture densities. 27
Fig. 3.13: Strain distribution within the extracted damage-zone subvolume for different fracture densities. 28
Fig. 4.1: Model construction. 32
Fig. 4.2: Stress reduction on the fault for fractures attached to the fault. 33
Fig. 4.3: (a) Stress reduction on the fault and (b) slip in this region. 35
Fig. 4.4: Stress reduction on the fault for fractures located 1 m away from the fault. 36
Fig. 4.5: Seismic source parameters change for the base case. 39
Fig. 4.6: (a) shear displacement and (b) peak particle velocity distribution on the fault. 40
Fig. 4.7: Slip increment under different stiffness conditions. 41
Fig. 4.8: Changes in normalized seismically radiated energy with normal and shear stiffness. 42
Fig. 5.1: Fault damage zone. 45
Fig. 5.2: Fracture distribution in a fault damage zone. 47
Fig. 5.3: Equivalent continuum model construction. 48

Fig. 5.4: Numerical model showing zones with anisotropic or isotropic compliance tensor. 50
Fig. 5.5: Distance from the fault core. 53
Fig. 5.6: Analysis procedure. 54
Fig. 5.7: (a) Stresses applied to the model boundaries (cross-sectional view), (b) displacement constraint conditions, (c) and effective normal stress reduction to induce seismic events on the fault 56
Fig. 5.8: Initial stress state of the model. 56
Fig. 5.9: Schematic diagram of energy during earthquake. 58
Fig. 5.10: Normalized seismic source parameters change under base case. 59
Fig. 5.11: Near-fault peak particle velocity for (a) base case, (b) near-fault fracture density coefficient of 5, and (c) distance of 30 m. 60
Fig. 5.12: Shear displacement increment on the fault for (a) base case, (b) near-fault fracture density coefficient of 5, and (c) distance of 30 m. 61
Fig. 5.13: Effect of damage zone stiffness on seismic source parameters. 62
Fig. 5.14: Spatial distribution of the first component (E_{11}) of the equivalent elastic matrix calculated using crack tensor theory under various fracture stiffness conditions. 63
Fig. 5.15: Normalized seismic source parameters under various conditions. 64
Fig. 5.16: Normalized seismic source parameters using fracture density coefficient of (a) 5, and (b) 30..... 66
Fig. 5.17: Normalized damage zone stiffness for (a) different near-fault fracture density coefficient, and (b) fracture surface areas. 66
Fig. 5.18: Normalized seismic source parameters using increased fracture stiffness that are (a) 0 m, and (b) 30 m from the fault core. 67
Fig. 5.19: The thickness of the fracture with increased stiffnesses. 68
Fig. 5.20: Seismic source parameters under different thicknesses. 68
Fig. 5.21: PPV distribution under different thicknesses of the enhanced fracture. 69

List of Tables

Table 3.1: Geometric characteristics of 3DP specimens. 17
Table 5.1: Damage zone mechanical properties. 52
Table 5.2: Various cases of the fault damage zone. 53

1. Introduction

1.1 Background

Induced seismicity, also known as anthropogenic seismicity, has become a significant scientific topic and social issue (Suckale. 2009; Grigoli et al., 2017). It is triggered by disturbances in in-situ stress resulting from various underground development and utilization projects, such as mining activities and fluid injection. Induced seismicity can lead to production losses, damage to equipment, collapse, economic losses, and in severe cases, loss of life. It is also likely to persist in the upcoming decades due to mining progressing deeper (Panel. 2006; Majer et al., 2007), subsurface gas reservoirs (Bachu. 2006; Bickle. 2009), etc. The frequency and magnitude of induced seismicity are increasing, with the potential for more severe cases and significant damage to underground infrastructure (Li et al., 2007; Foulger et al., 2018). In particular, driven by the rising demand for mineral and energy resource extraction, mining-induced seismicity has been studied for decades and continues to draw public attention due to the associated seismic risks. Although mining-induced seismicity releases less energy compared to natural earthquakes, they occur more frequently and typically at shallow depths, within a few kilometers (Li et al., 2007). Mining-induced seismicity may lead to structural damage, equipment malfunction, collapse of tunnels and stopes, and in severe cases, loss of life. Consequently, developing effective mitigation methods is critical to reducing seismic risks and ensuring the long-term sustainability of underground mining activities.

1.2 Literature review

1.2.1 Mitigation methods for induced seismicity

To better understand the current status and limitations of mitigation strategies, this section first reviews conventional methods used to reduce the risks associated with induced seismicity. Mining-induced seismicity has been identified as a hazard to underground miners and has intensified significantly with the progression of modern mining activities. Many methods have been developed and implemented to mitigate mine-induced seismic risks, e.g., microseismic (MS) monitoring technique (Wang et al., 2008; Leśniak et al., 2009; Liu et al., 2019); destress rock blasting (Dvorsky et al., 2005; Konicek et al., 2013); using stiff tunnel lining; rock support; and placement of coal pillars (Li et al., 2007). Furthermore, with the development of shale gas and

geothermal energy, fluid-injection induced seismicity has become more frequent and larger enough to cause damage (Evans et al., 2012; Zang et al., 2014; Rubinstein et al., 2015). Many methods have also been developed to mitigate the damage caused by induced seismicity due to fluid injection, such as the seismic traffic light system (Häring et al., 2008; Mena et al., 2013; Maxwell et al., 2015) and cyclic injection (Zang et al., 2019; Zhu et al., 2021). These methods have the potential to reduce the magnitude of induced seismicity; however, their effectiveness is limited because they primarily rely on monitoring or operational controls and do not explicitly address the mechanical origin of seismic events. (Sainoki et al., 2017; 2019). In particular, they fail to account for the strong stress heterogeneity and complex mechanical behavior underground, where densely distributed fractures significantly influence stress redistribution and energy accumulation (Sainoki et al., 2021). As a result, even relatively small stress perturbations may trigger unexpectedly large seismic events in regions distant from active excavations. Therefore, more efficient and effective seismic mitigation strategies that consider the geological-structure-induced stress heterogeneity should be implemented.

Furthermore, seismic events in deep underground mines are often spatially distributed, occurring not only near active mining areas but also at significant distances from underground workings. Pre-existing geological structures are widely recognized as key contributors to the spatial distribution of seismicity (Ma et al., 2019; Wang et al., 2019). In particular, structures such as dykes, high-stiffness regions, and faults can significantly alter the in-situ stress field, increasing the potential for intense seismic events (Sainoki et al., 2016). Consequently, accurate characterization of these structures is essential for assessing seismic hazards and designing effective mitigation strategies. Among them, faults are known to be the most critical, as fault slip can generate the most damaging seismic events (Blake and Hedley. 2003). Therefore, this study focuses on fault zones and their mechanical behaviour. A fault zone typically consists of a narrow fault core surrounded by a wider damage zone of highly fractured rock mass. The detailed structure of fault zones is further discussed in Section 4.2.

1.2.2 Heterogeneity of damage zones and experimental challenges

It should be noted that fault damage zones in nature are inherently heterogeneous, and this heterogeneity strongly influences stress redistribution, deformation processes, and the mechanical effectiveness of mitigation strategies. Most previous laboratory studies use surface-breaking or

artificially induced fractures to represent complexity of rocks and compute the stress-strain states commonly through direct shear tests, compression tests, and loading-unloading experiments on pre-cut specimens (Goodman, 1976; Bandis et al., 1983; Barton & Choubey, 1977; Zhao et al., 2022; Gao et al., 2023). While these methods reveal useful empirical stiffness-closure relationships, they cannot represent the behavior of natural fractures embedded in fault damage zones.

Natural fractures in fault damage zones exhibit complex morphology, roughness, aperture distribution, filling materials, and stress conditions that differ significantly from surface fractures (Chester et al., 1993; Faulkner et al., 2010; Savage & Brodsky, 2011; Mitchell & Faulkner, 2012). These internal features strongly influence fracture compliance and energy dissipation during fault slip (Hickman et al., 1995; Lockner et al., 1991; Ohnaka, 2003). Therefore, laboratory measurements based solely on exposed surfaces or artificially discontinuities cannot provide realistic situations for internal fracture networks within fault damage zones (Yin et al., 2022; Li et al., 2018; Wang et al., 2021).

To overcome this limitation, 3D printing (3DP) technology has been widely applied in the field of rock mechanics. By fabricating rock-like specimens with predefined internal fracture geometries, 3DP samples enable precise control over fracture morphology, spacing, orientation, and connectivity, which are difficult to reproduce using conventional specimen preparation methods. Moreover, CT scanning enables three-dimensional reconstruction of fracture geometry and aperture evolution under load without destructive preparation (Ketcham & Carlson, 2001; Liu et al., 2016). When combined with digital image volume correlation (DVC) method, high-resolution strain fields can be obtained, allowing calculation of internal fracture normal and shear stiffness based on measured deformation (Hall, 2006; Sutton et al., 2009; Huo et al., 2020). Overall, existing experimental techniques cannot characterize the mechanical properties of natural damage zones, whereas CT- and DVC-based analysis of 3DP specimens enables direct quantification of strain distribution of internal fractures. This methodology provides direct experimental insight into the complex stress-strain states within fault damage zones, thereby establishing a physical basis for subsequent numerical modeling.

1.2.3 Numerical modeling approaches for heterogeneous fault damage zones

Numerical modeling has been widely used in rock mechanics to investigate complex deformation and failure processes that are difficult to reproduce or monitor directly in laboratory

and field experiments. In recent decades, numerical investigations into the stability of causative faults influenced by mining operations have been largely analysed on models incorporating a persistent and prominent slip surface. However, conventional continuum numerical analyses that assume isotropic and homogeneous rock mass mechanical properties are unable to adequately capture the formation of seismic clusters or the complex stress states in such regions distant from active mining areas. Assuming the homogeneity of rock mass in numerical simulations may lead to inaccurate stress states, making it essential to consider rock mass heterogeneity when assessing seismic hazards (Sainoki and Mitri. 2014). Recent studies based on a numerical modeling approach with the discrete element method (DEM) that a fracture network in a local shear zone away from active mining areas contributes to the generation of abnormal stress state and intense seismic activity whilst quantifying strain energy accumulated and resultant burst-prone potential (Sainoki et al., 2019; Sainoki, Tabata, et al., 2017). Such studies provided insight into the influence of densely fractured local region on the heterogeneous characteristic of in-situ stress state with highly stressed regions, emphasizing the importance of considering a fracture network in simulating pre-mining stress state and evaluating the risk for severe seismic activity. However, a seismic event taking place in a fault damage zone extends from dozens of meters to hundreds of meters, whereas the edge length of the DEM model constructed in previous studies is less than 10 m. This illustrates the difficulty in explicitly modeling a whole fracture network in a fault region that presumably contains millions of fractures or more with various dimensions.

Overall, the above discussion highlights the inherent limitations of existing numerical approaches when applied independently. Continuum-based models are capable of simulating large-scale stress redistribution associated with mining activities, but their reliance on isotropic and homogeneous representations prevents them from capturing the complex stress states that develop within fault damage zones containing densely distributed fractures. Conversely, discontinuum-based models with explicit fracture networks can reproduce abnormal stress states and intense seismic activity at the local scale, yet their application is restricted by computational constraints and limited spatial extent.

Taken together, these limitations indicate that no single numerical approach is sufficient to capture both the mine-scale stress distribution and the mechanical behavior of fault damage zones at the fracture-scale. In particular, there is a need to develop approaches that are capable of representing the heterogeneous stress fields associated with fault damage zones at the mine scale,

while remaining consistent with the fracture-scale mechanisms governing localized deformation and instability. Addressing this challenge is essential for improving the physical realism of numerical analyses of fault-related seismicity and forms the basis for the research objectives defined in the following section.

1.3 Objectives

Previous studies have demonstrated the importance of numerical modeling in investigating mining-induced seismicity and fault stability. However, as reviewed in the previous section, existing approaches face inherent limitations when applied independently. Continuum-based models are capable of simulating large-scale stress redistribution but rely on simplified isotropic and homogeneous representations that cannot adequately capture the complex stress states within fault damage zones. In contrast, discontinuum-based models with explicit fracture networks provide valuable insight into localized deformation and abnormal stress states, yet their application is restricted to relatively small spatial scales due to computational constraints. Moreover, direct experimental evidence characterizing the internal mechanical complexity and heterogeneous stress-strain states within fault damage zones remains limited. These limitations highlight the need for a comprehensive framework that can integrate experimental observation with multiscale numerical analysis. Based on the above considerations, the main objectives of this thesis are as follows:

1. To establish and theoretically verify a stiffness-based seismicity mitigation strategy using the slip-weakening framework, clarifying the relationship between damage zone stiffness and seismically radiated energy.

2. To experimentally elucidate the mechanical complexity and heterogeneous strain states within fault damage zones using an X-ray computed tomography (CT)- and digital image correlation (DVC)-based approach on 3D-printed rock-like specimens, and to provide physical insight into the internal strain states of damage zones for subsequent numerical modeling.

3. To construct a fracture-scale numerical model incorporating explicitly generated discrete fracture networks (DFN), with the primary objective of elucidating how increasing fracture stiffness controls fault-slip behavior and seismic source parameters, thereby complementing and verifying the mine-scale equivalent continuum analyses.

4. To develop a mine-scale equivalent continuum numerical model based on crack tensor

theory, capable of reproducing the complex stress fields associated with fault damage zones, and to investigate how increasing fracture stiffness within the fault damage zone influences fault-slip behavior and seismic source parameters under mining-induced conditions.

1.4 Content of research

In this study, a stiffness-based mitigation strategy is proposed to reduce the intensity of induced seismicity by increasing the stiffness of fractures within fault damage zones. The effectiveness of this strategy is quantitatively evaluated through multiscale numerical modelling and laboratory characterization. First, the inherent mechanical complexity of fault damage zones is examined experimentally. A CT- and DVC-based experimental approach using 3D-printed rock-like specimens is developed to visualize and quantify the internal stress-strain states within damage zone analogues. These observations establish a physical basis for subsequent numerical modelling and motivate the need to explicitly consider damage-zone heterogeneity in simulations. To investigate the proposed stiffness-based mitigation strategy across different spatial scales, numerical simulations are conducted from two complementary perspectives. At the mine scale, an equivalent continuum model based on the crack tensor theory is developed to reproduce heterogeneous stress conditions around a fault and to assess how increased near-fault stiffness influences seismic source parameters. Besides, a discrete element method (DEM) model incorporating an explicit discrete fracture network (DFN) is constructed to investigate the mechanical role of fracture normal and shear stiffness in controlling fault-slip behavior and energy release at the fracture scale. Therefore, both a finite-difference continuum model (FLAC3D) and a distinct-element model (3DEC) are employed to investigate the effect of increasing fracture stiffness on induced seismicity. The continuum model allows us to simulate a large-scale fault system under complex geological and mining conditions with a heterogeneous stress field, and to represent the fault damage zone by an equivalent stiffness. However, fractures are treated implicitly in this framework, and individual discontinuities are not geometrically resolved. In contrast, the distinct-element model explicitly represents fractures as discontinuities within a DFN and can capture localized slip, opening and block rotation at the fracture scale, although the model size is more limited due to computational cost. By combining these two approaches, the continuum model provides large-scale trends and engineering implications of stiffness enhancement, while

the distinct-element model offers a mechanistic verification at the fracture scale, thereby strengthening the overall conclusions of this thesis.

In Chapter 1, the background and significance of induced seismicity in mining and related subsurface engineering are introduced. The limitations of conventional mitigation methods are reviewed. The objectives and overall framework of the thesis are also presented.

In Chapter 2, the theoretical basis for stiffness-based mitigation is established using the slip-weakening framework. The relationship between system stiffness, fault slip behaviour, and seismically radiated energy is examined, and a parametric analysis is conducted to verify the theoretical feasibility of reducing seismic intensity through stiffness enhancement. This chapter provides the theoretical foundation for the subsequent numerical investigations.

In Chapter 3, experimental investigations are conducted to examine the internal mechanical complexity of fault damage zones. A CT- and DVC-based experimental methodology using 3D-printed rock-like specimens is developed to visualize and quantify internal strain states within damage zone analogues. The experimental results are used to characterize deformation patterns and strain distributions within fractured media, providing a physical basis for the numerical modelling approaches adopted in the subsequent chapters.

In Chapter 4, a discrete element method (DEM) model incorporating an explicitly generated discrete fracture network (DFN) is constructed to further investigate the effects of stiffness-based mitigation at the fracture scale. Fractures within the fault damage zone are modelled as disk-shaped discontinuities with prescribed normal and shear stiffness. Parametric studies are conducted by varying fracture stiffness and independently increasing normal and shear stiffness to clarify their relative contributions to seismic source parameters and slip behaviours.

In Chapter 5, an equivalent continuum model based on the crack tensor theory is developed to simulate a mine-scale fault system with an anisotropic fault damage zone. The model reproduces heterogeneous in-situ stress conditions and mining-induced fault-slip, enabling quantitative evaluation of seismic source parameters, and slip behaviours under different stiffness conditions. The influence of increasing near-fault fracture stiffness is systematically examined for various geometric and mechanical configurations, and the effectiveness of the proposed mitigation strategy is assessed at the macroscopic scale.

Chapter 6 summarizes the main findings of this thesis and discusses their implications for the mitigation of induced seismicity in deep underground mines. The advantages and limitations of

the proposed stiffness-based strategy, as well as the numerical and experimental approaches, are highlighted. Recommendations for future research and potential applications to practical mine design and seismic risk management are also provided.

2. Theoretical basis for stiffness-based mitigation strategy

2.1 Inrtoduction

This chapter reviews the slip-weakening law as a fundamental framework for fault instability and seismic energy release.

Based on this theory, it is shown that increasing the stiffness of the surrounding rock mass can effectively reduce seismic energy release during fault slip. Motivated by this insight, this study proposes a stiffness-based mitigation strategy that enhances the mechanical stiffness of the fault damage zone to suppress induced seismicity, which is subsequently examined through numerical simulations in the following chapters.

2.2 Slip-weakening concept

Given the limitations of conventional methods, a novel concept based on stiffness enhancement has been proposed in this study. According to the slip-weakening model (Li et al., 1986; Venkataraman et al., 2004), during the stress relaxation process, the stress acting on the fault decreases to a constant level after an earthquake, while the stress in the rock mass surrounding the fault linearly decreases from τ_1 to the final stress state τ_2 (Fig. 2.1). When the stress of the fault reaches static equilibrium (intersection of the fault traction with the stress of the rock), the slip does not stop. As soon as the slip stops, the stress drops to the final stress state (Kanamori et al., 2006). The slope of the dotted line denotes the stiffness of the rock mass surrounding the fault, and the striped region represents the radiated energy. It is thus plausible to assume that if the stiffness of the rock mass surrounding the fault increases, the radiated energy can be reduced. Based on this assumption, this study examines the effectiveness of increasing the rock mass stiffness surrounding the fault for controlling the intensity of induced seismicity.

This theoretical inference is consistent with field observations and numerical studies. Field observations from the Copper Cliff mine show that aseismic fault-slip can occur when a weak fault core is embedded in high-stiffness surrounding rock. Sainoki et al. (2017) successfully reproduced this behaviour, demonstrating that fault slip within a stiffer damage zone does not always lead to severe seismic events. This field example supports the idea that stiffer damage zone stiffness plays a key role in controlling the intensity of seismicity. Additional support for this concept comes from laboratory experiments (Zhao et al., 2022; Yin et al., 2022; Gao et al., 2023). For example, Yin et al. (2022) conducted laboratory tests on sandstone specimens using a modified stiffness loading

system and found that lower system stiffness resulted in more brittle failure behaviour. Ma et al. (2024) performed experiments on coal specimens using a loading system with adjustable stiffness. The results showed that lower loading system stiffness led to more abrupt post-peak failure, increased fragment ejection, and significantly higher kinetic energy release. These results highlight a mechanical principle that is also relevant at the geological scale. In particular, the loading system in the experimental setup can be regarded as an analogue to the fault damage zone, which controls the energy dissipation and dynamic behaviour during failure. These findings suggest that enhancing the stiffness of fractures within the fault damage zone could effectively suppress the magnitude and intensity of induced seismicity. This theoretical foundation forms the basis for the stiffness-enhancement strategy examined in this study. It is emphasized that the purpose of this theoretical analysis is not to develop a new friction law, but to clarify the physical mechanism by which damage-zone stiffness influences seismically radiated energy within the slip-weakening framework.

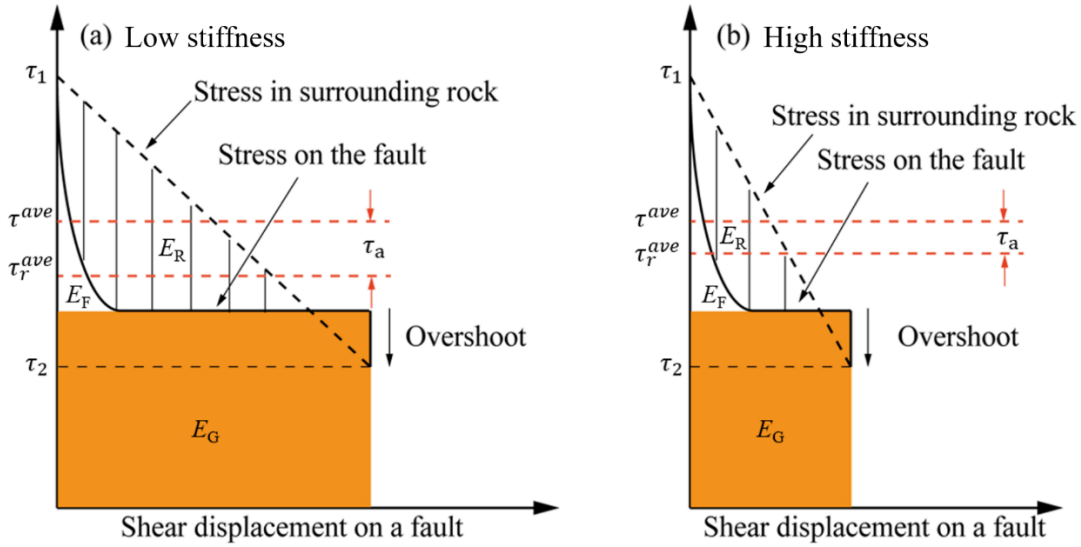

Fig. 2.1: Schematic representation of energy release based on slip-weakening model.

2.3 Theoretical verification

To verify the theoretical relationship between damage zone stiffness and seismically radiated energy, a parametric study is conducted using a linear slip-weakening model as expressed below (Bizzarr. 2011):

$$\tau=\begin{cases}\left[\mu_u-\left(\mu_u-\mu_f\right)\dfrac{u}{D_c}\right]\sigma_n\ \left(u<D_c\right)\\ \mu_f\sigma_n\ \left(u\geq D_c\right)\end{cases} \tag{2.1}$$

where τ and σ_n represents the shear and normal stresses acting on the fault; μ_u and μ_f denote the coefficients of static and kinetic friction; u and D_c are the dynamic relative shear displacement and characteristic slip-weakening distance, respectively. Since the mechanical behaviour of the surrounding rock also plays a crucial role in this process, the following analysis aims to theoretically demonstrate that an increase in system stiffness leads to a reduction in the seismically radiated energy. This provides a basis for the subsequent numerical modelling.

According to Kanamori (2007), for a simple shear fault where the shear stress and slip are assumed to be uniform over a fault area A, the radiated energy during an earthquake can be written as:

$$E_R=\frac{1}{2}\left(\tau_1+\tau_2\right)\mu A-A\int_0^{\mu}\tau d\mu \tag{2.2}$$

where τ is the shear stress acting on the fault; $\tau_1$and τ_2 represent the initial and residual stresses on the fault, respectively; μ and A are the shear displacement and fault area, respectively. The seismically radiated energy can be approximated as the area of the trapezoid defined by the shear stress–slip curve of the surrounding rock minus the area under the shear stress-slip curve of the fault. Based on this assumption, this theoretical framework assumes that the stress on the fault decreases from an initial value to a final residual value during slip. In the simplest case, assuming a constant final stress, the seismically radiated energy can be approximated as the area enclosed between the stress-slip curves of the surrounding rock and the fault core, as illustrated in Fig. 2.1 This area can be typically computed as the integral of the stress difference over displacement:

$$E=\int_0^{u_f}\left(\tau_R-\tau_F\right)du \tag{2.3}$$

where u_f represents the shear displacement on the fault; τ_R and τ_F denote the stress on the surrounding rock and fault core, respectively. As shown in previous studies (Scholz, 1998), the loading system stiffness is inversely proportional to the rupture size and is proportional to the shear modulus of the rock mass as below.

$$k = \frac{\alpha G}{L} \tag{2.4}$$

where α, G, and L denote the geometrical constant, shear modulus of the surrounding rock mass, and the size of the slip area.

To examine the relation between damage zone stiffness and seismically radiated energy, a base case assumes a circular slip region with a diameter of 10 m and 7 GPa as the shear modulus of the surrounding rock mass, which yields 0.7 GPa/m as the loading system stiffness, according to Eq. (2.4) with the assumption of $\alpha = 1.0$. Provided that the confining stress acting on the fault is 35 MPa with the static and kinetic friction coefficients of 0.6 and 0.4, respectively, the total slip is calculated as 10 mm, assuming the simplest case where the slip terminates at the static equilibrium point without over- or undershoot (Kanamori, 2007). It is to be noted that the static and kinetic friction coefficients were numerically verified in terms of slip rate and seismic efficiency by simulating an induced seismic event under dynamic conditions (Sainoki et al., 2020). Additionally, the confining stress approximately corresponds to stress states at depths ranging from 1000 m to 2000 m, where severe mining-induced seismicity is frequently reported (Larsson and Kristina, 2004; Wagner, 2019); and the shear modulus of 7 GPa was roughly estimated with the equation proposed by Hoek and Diederichs (2006) whilst assuming an elastic modulus of 60 GPa, Poisson's ratio of 0.2 and Geological Strength Index (GSI) (Marinos and Hoek, 2000; Marinos et al., 2005) of 50. The elastic parameters are considered to be typical values as those of stiff, plutonic rocks (Malek et al., 2009; Sosna. 2011; Sainoki et al., 2021). It is to be noted that although GSIs of fault zones are sometimes estimated to be less than 30 (Gábor Somodi et al., 2018) in the vicinity of the fault core, GSI would increase in the surrounding rock mass with the distance from the core as indicated by the study (Mirabedini et al., 2022). Considering this, the GSI of 50 was estimated for the base case. Then, a slip-weakening distance D_c of 1 mm is assumed for the base case. The validity of the D_c can be assessed as follows. The seismic moment and moment magnitude of the event are calculated as 5.50×10^9 N·m and 0.46, respectively, with the following equations (Aki, 1966; Kanamori. 1978).

$$M_0 = G \cdot D \cdot S \tag{2.5}$$

$$M_w = \frac{2}{3}\left(\log M_0\right) - 10.7 \left(M_0 \text{ in dyn-cm}\right) \tag{2.6}$$

where G, D, and S are the shear modulus of the surrounding rock mass, slip amount averaged and the slip area; M_0 and M_w are the seismic moment and moment magnitude, respectively. The magnitude falls within a reasonable range of induced seismic events (Richardson. 2022). Then, D_c of the event can be roughly estimated using the equation proposed by Ohnaka (2000) as Eq. (2.7). It is to be noted that this equation represents an empirical correlation between the seismic moment (M_0) and the slip-weakening distance (D_c), which is employed to examine the validity of the assumed D_c for the simulation.

$$D_c = \sqrt[3]{M_0 / 10^{19}} \tag{2.7}$$

The equation yields a D_c of 0.82 mm. Moreover, other studies indicate that D_c is approximately 10% of the total slip (Andrews. 2005; Norini et al., 2009), resulting in a D_c of 1 mm. Hence, the D_c assumed for the base case is deemed quite reasonable. Note that the D_c is varied in the following parametric study to elucidate its influence on the proposed method.

Fig. 2.2b-d illustrate variations from the base case, including (b) a case with doubled fracture stiffness, (c) increased static friction of 0.7, and (d) decreased kinetic friction of 0.3. In all cases, the critical slip-weakening distance D_c and the normalized damage zone shear stiffness were systematically varied, with D_c ranging from 1 mm to 4 mm and the normalized stiffness varying from 1 to 2. The results reveal a consistent trend across all subplots: an increase in the normalized damage zone shear stiffness and slip-weakening distance leads to a significant reduction in seismically radiated energy. More specifically, when the normalized damage zone stiffness increases from 1 to 2, the seismically radiated energy decreases by over 50% at each D_c level. Likewise, increasing D_c from 1 to 4 mm results in an energy reduction of up to 60%, regardless of the stiffness level. This inverse relationship is especially evident between Fig. 2a and 2b, where increasing the damage zone stiffness constrains fault slip and suppresses radiated energy. Similarly, regardless of the changes in frictional parameters in Fig. 2.2c and 2.2d, the decreasing trend of seismically radiated energy with increasing damage zone shear stiffness remains consistent.

In summary, these theoretical results demonstrate that increasing the stiffness of damage zone can effectively reduce the seismically radiated energy. This provides a solid theoretical foundation for the subsequent numerical simulations, where such mitigation strategies are further explored under more realistic conditions.

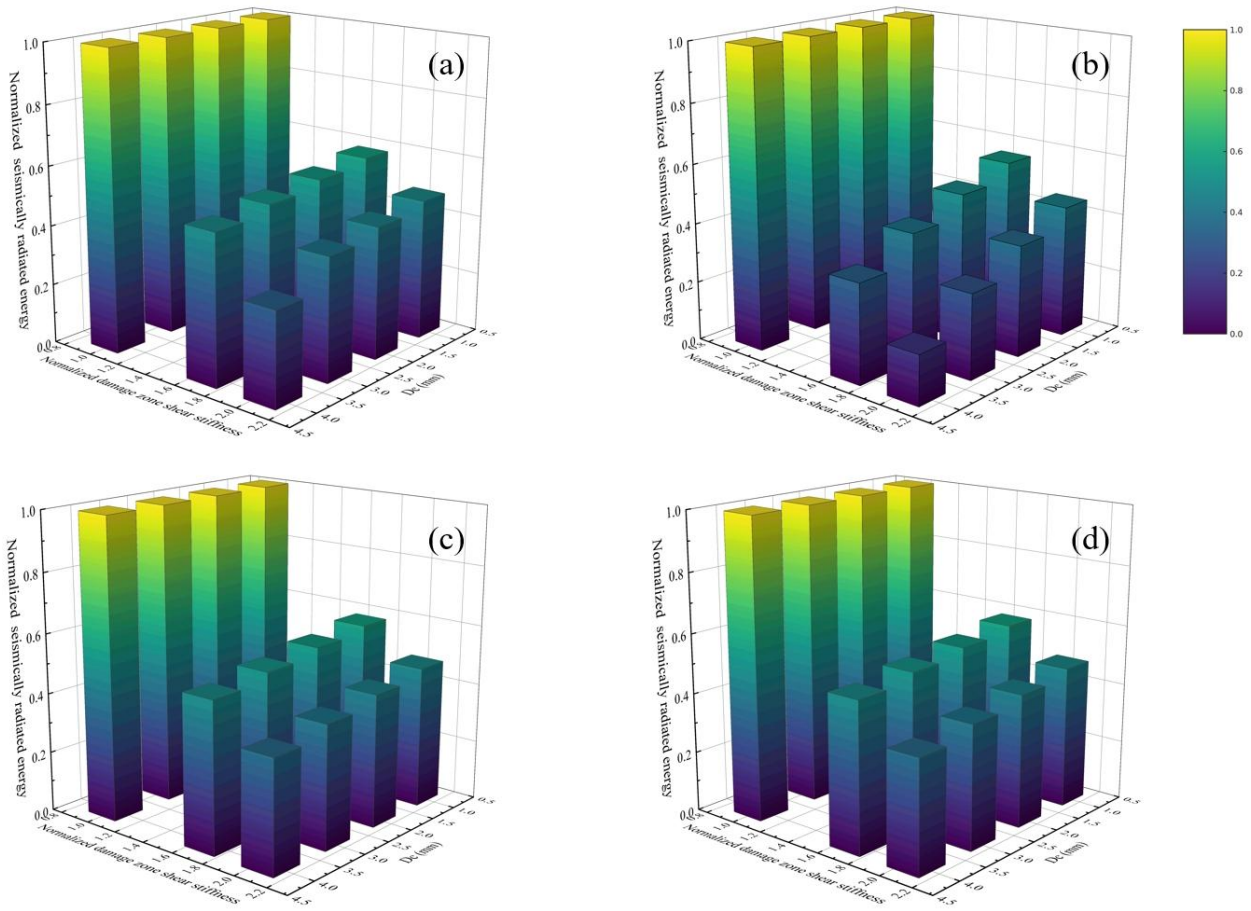

Fig. 2.2: Theoretical verification for (a) base case, (b) doubled initial stiffness, (c) static friction of 0.7, and (d) kinetic friction of 0.3

3. Experimental investigation of heterogeneous stress-strain states in damage zone using 3D-printed specimens

3.1 Introduction

As discussed in Chapter 1, fault damage zones are characterized by complex internal structures and heterogeneous stress-strain states, which cannot be fully captured by simplified or homogeneous mechanical representations. Understanding such internal heterogeneity is essential for establishing a realistic physical basis for modelling fault behaviour and evaluating stiffness-based mitigation strategies for induced seismicity.

In this chapter, an X-ray computed tomography (CT)- and digital image correlation (DVC)-based experimental approach is developed using 3D-printed rock-like specimens to investigate the internal deformation behaviour of fractured fault damage zone analogues. By visualizing three-dimensional strain localization and displacement discontinuities within the specimens, the heterogeneous strain states arising from internal fractures are quantitatively characterized.

The experimental results provide direct insight into the mechanical complexity of fault damage zones and demonstrate the strongly non-uniform nature of deformation within fractured media. Based on these observations, the key deformation features and internal heterogeneity of the fractured medium are characterized, providing a reality-based foundation for numerical modelling presented in subsequent chapters, at both the mine and the fracture scales.

3.2 Sample preparation and experimental design

3.2.1 Preparation of samples containing internal prefabricated discontinuities

Traditionally, rock analog specimens with prefabricated flaws are manufactured by casting with molds. Although this method is simple and widely used, it can only produce throughgoing flaws, and it is practically impossible to create internal, non-throughgoing discontinuities with prescribed geometry (Fig. 3.1). In contrast, additive manufacturing (3DP) currently provides the only practical means of fabricating specimens with internal fractures or discontinuities whose position, orientation, and size can be accurately controlled. For this reason, 3DP is adopted in this study to prepare rock-like specimens containing a single internal discontinuity at a well-defined location.

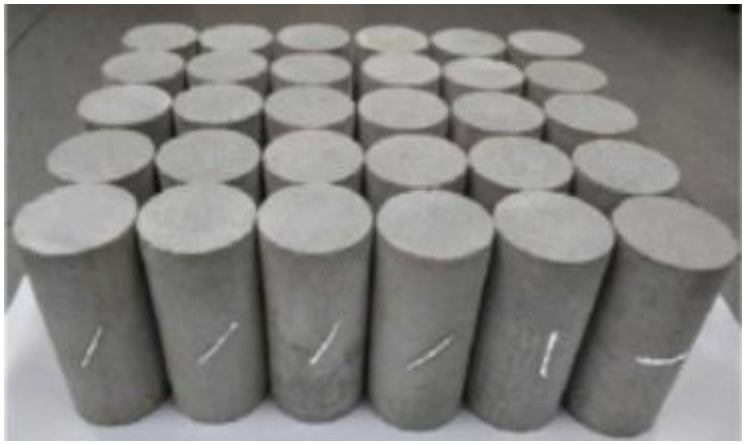

Fig. 3.1: Specimens with prefabricated flaws by casting method.

Figure 3.2 illustrates the geometry and internal configuration of the 3D-printed specimens designed to emulate a simplified fault damage zone structure. The specimens consist of a cylindrical host body containing a planar fault core embedded within a surrounding damage zone analogue. The fault core is inclined at an angle of 60° with respect to the specimen axis and is represented by a prefabricated discontinuity with controlled geometry. Surrounding the fault core, a population of smaller discontinuities is distributed to mimic the fractured nature of fault damage zones observed in natural systems.

To represent fault damage zones with different degrees of internal structural complexity, the surrounding fracture network is systematically varied in terms of fracture density, while the geometry of the fault core is kept identical for all specimens. The damage zone is characterized by an explicitly defined discrete fracture network (DFN), in which the fracture density is quantified using the three-dimensional fracture intensity parameter P32, defined as the total fracture surface area per unit volume (m^{-1}). The configurations of internal discontinuities considered in this study are summarized in Table 3.1. Sample A represents a reference case containing only a single fault core with a length of 30 mm and no additional distributed fractures in the surrounding damage zone. Samples B, C, and D incorporate progressively denser fracture networks in addition to the fault core, with P32 values of 10, 20, and 30, respectively. By increasing P32 while keeping the fracture size constant, the density of fractures within the damage zone is systematically increased. The individual fractures are represented by disk-shaped discontinuities with diameters ranging from 4 to 8 mm, which are identical across all configurations. By varying the fracture density parameter P32 while maintaining identical fault-core geometry, fracture size distribution, and

overall specimen dimensions, a family of specimens with increasing degrees of damage-zone complexity is obtained. This design isolates the mechanical influence of damage-zone fracture density from that of fault-core geometry and material properties, allowing the role of distributed internal discontinuities in controlling deformation behavior and apparent stiffness characteristics to be systematically examined. As such, the specimens provide a simplified physically consistent analogue for investigating the mechanical heterogeneity of natural fault damage zones.

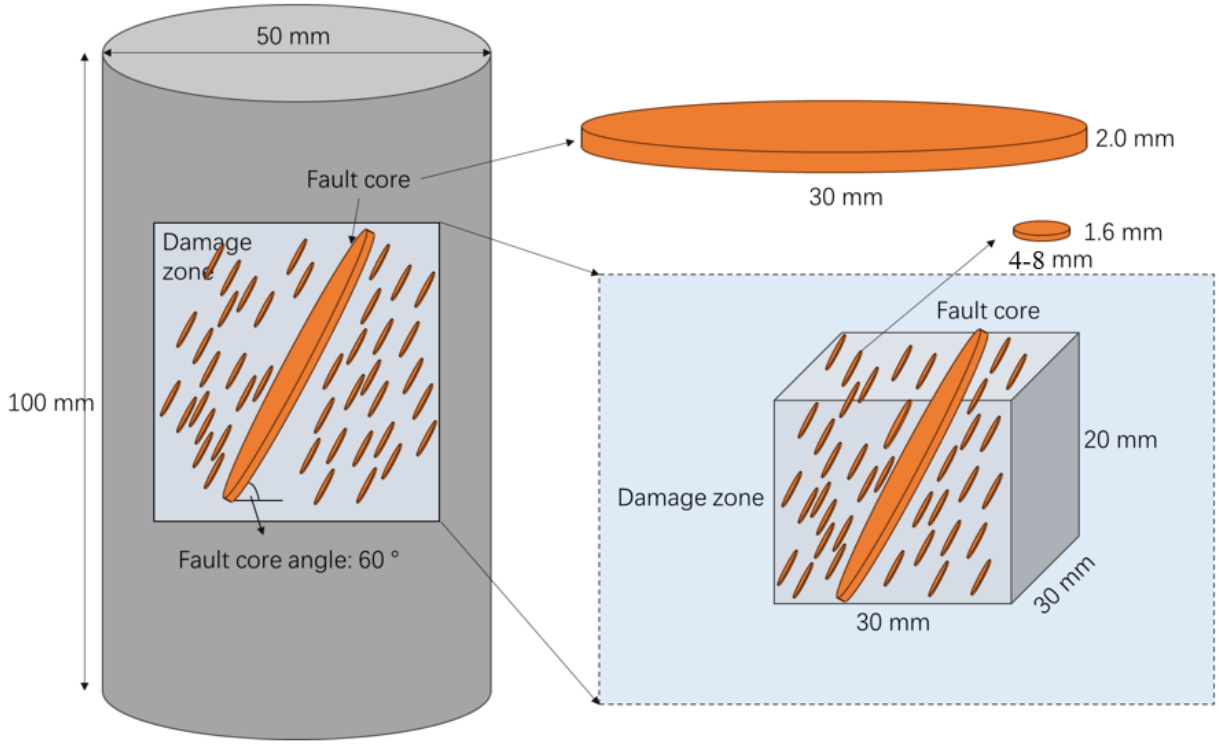

Fig. 3.2: Design of specimens with various fracture patterns.

Table 3.1: Geometric characteristics of 3DP specimens.

Sample id	Fault core length (mm)	Fracture length (mm)	P32 (m^{-1})
A	30	4-8	0
B	30	4-8	10
C	30	4-8	20
D	30	4-8	30

3.2.2 3DP manufacturing procedure of rock-like samples

First, the model designed in CAD or SolidWorks is imported into the printing system. After the geometrical models of the specimens had been generated, they were imported into an Easy-3DP-S450 sand-powder 3D printer, and the printing process was initiated. In this study, GS19 silica sand activated by an acid hardener was used as the base powder, and a furan resin was adopted as the liquid binder (Fig. 3.3). The digital models were first sliced into a series of cross-sectional layers by the printer software, and the corresponding control commands were transferred to the built-in computer of the printer.

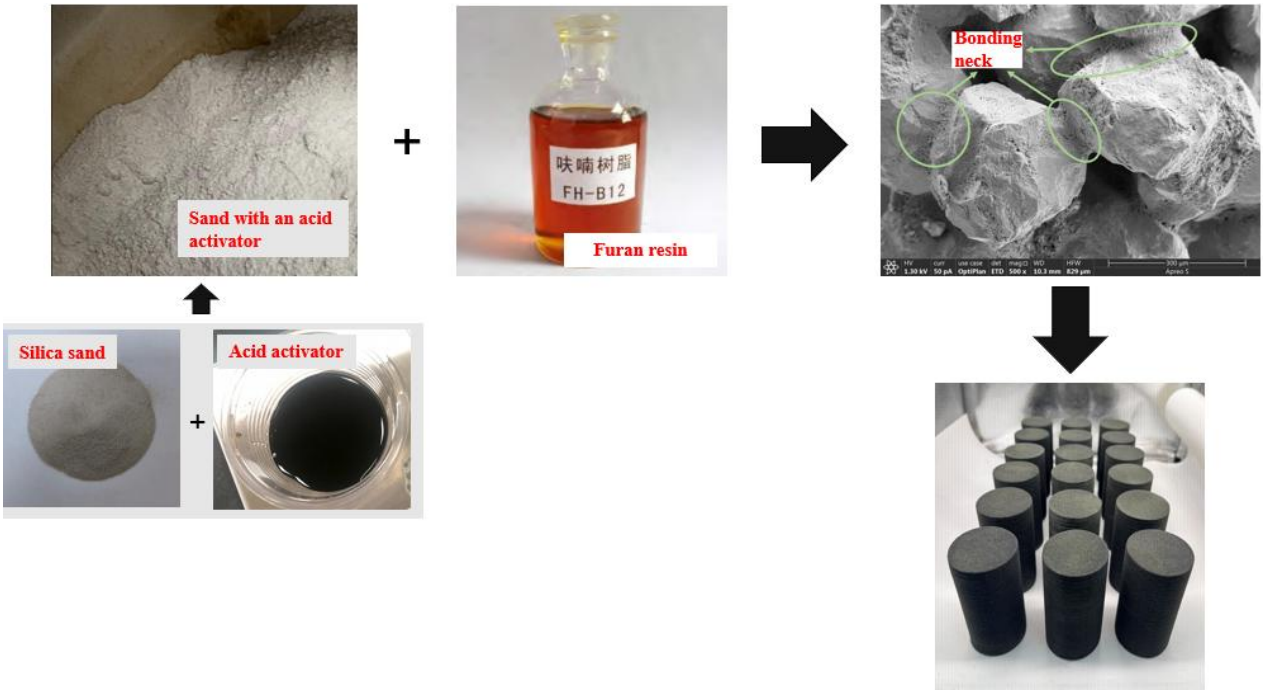

Fig. 3.3: Composition of 3DP specimens.

During fabrication, the print head moved according to these commands and selectively jetted the furan resin onto the powder bed along the contour of each sliced cross-section. After one layer was completed, the build platform was lowered by one layer thickness, the feed platform was raised by the same increment, and a roller spread a fresh, uniform layer of GS19 sand over the build area. The print head then performed the next pass of selective binder deposition. By repeating this sequence of powder spreading and binder jetting, the cylindrical specimens were gradually formed in a layer-by-layer manner, as shown in Fig. 3.4.

To realize internal, non-throughgoing discontinuities, the printer was programmed not to

dispense binder within the regions corresponding to the prefabricated fractures. Along the scan paths that passed over these regions, only loose, non-cemented sand powder was left in place while the surrounding matrix was solidified by the furan resin. Since all prefabricated fractures were fully embedded inside the specimens and did not intersect the outer surface, only the residual sand powder on the exterior was removed after printing, whereas the loose powder inside the flaws was preserved as internal discontinuities.

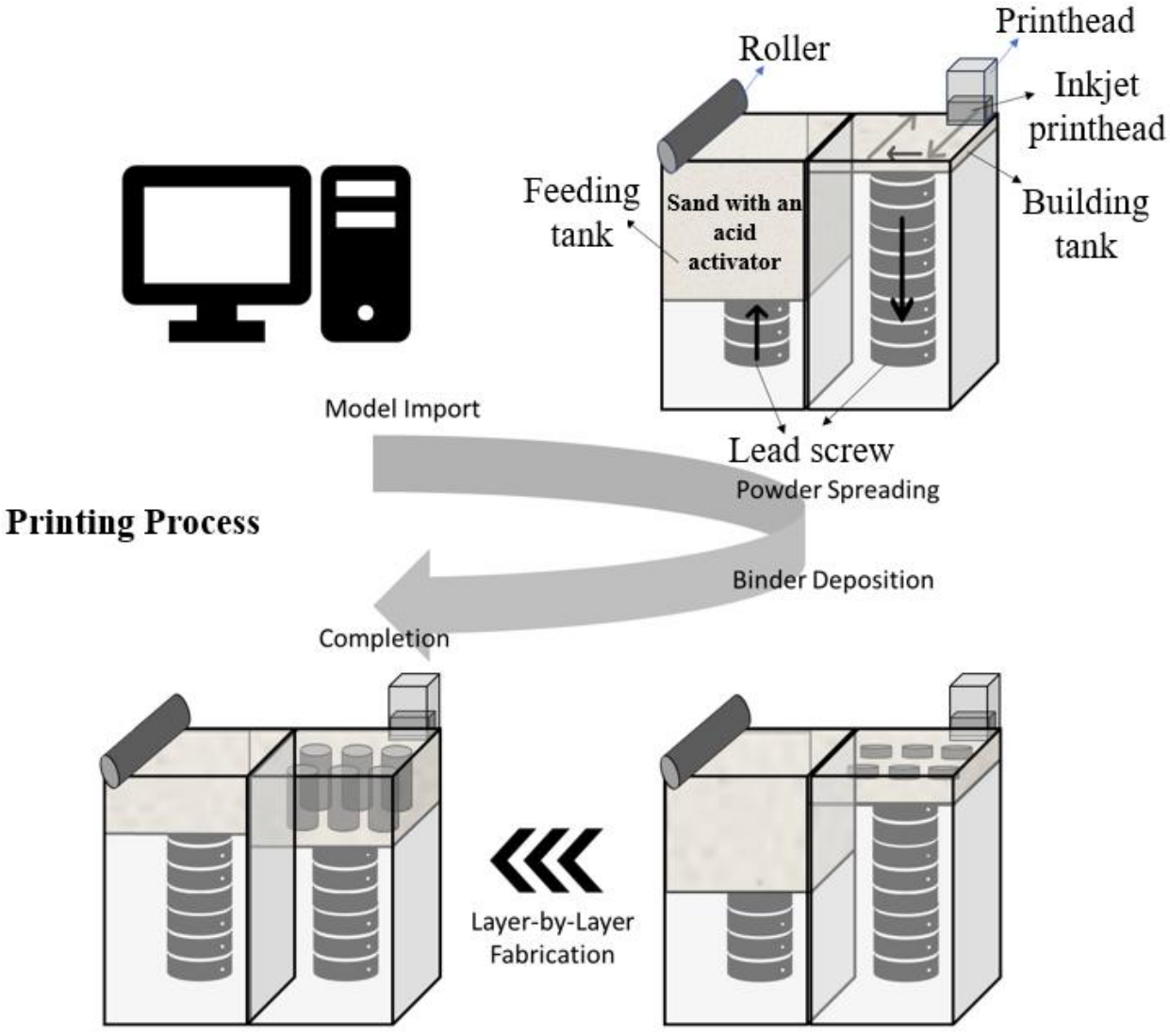

Fig. 3.4: Printing process of 3DP specimens.

3.2.3 CT-scanning set-up

In recent years, CT scanning has become an important tool for extracting and identifying the complex internal composition and structure information of solid samples more accurately, and

researchers worldwide have used CT scanning technology and regional growth algorithms to build digital models that can intuitively characterize the internal structure of natural fracture samples, improving the use of numerical simulation to quantitatively study the internal structure of complex coal and rock media encountered in engineering, especially the deformation and damage mechanisms. In-situ X-ray computed tomography (CT) was conducted using a Nikon X-ray CT system (Fig. 3.5). The apparatus consists of an X-ray source and a flat-panel detector facing each other, with a rotary stage mounted between them. An in-situ loading device was installed on the rotary stage so that the 3DP specimens could be axially loaded while being scanned. The cylindrical specimen was sandwiched between upper and lower loading plates inside a metallic fixture, and the entire fixture was fixed on the rotary stage to ensure stable rotation during imaging.

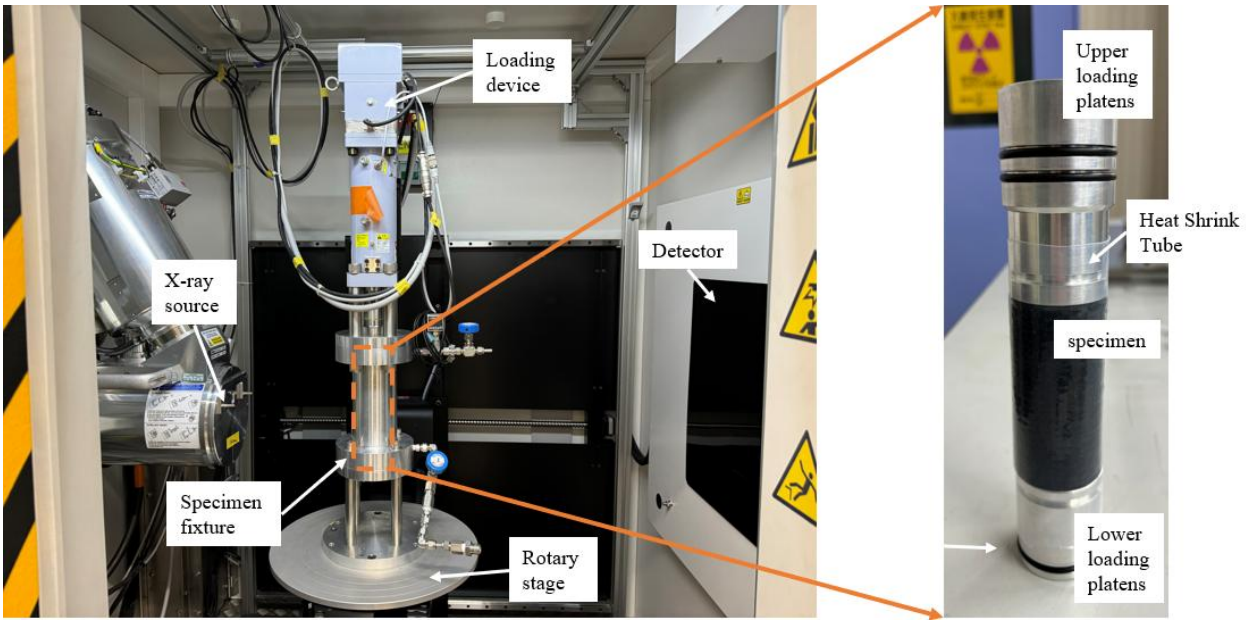

Fig. 3.5: Experimental device set-up.

Prior to scanning, each 3DP specimen was inserted into the in-situ loading device and axially aligned between the loading platens (Fig. 3.5). Axial compression was then applied in a stepwise manner. The total loading process was divided into five stages, and the axial stress was increased by 2.5 MPa at each stage, resulting in a final stress level of 12.5 MPa at Stage 5 (Fig. 3.6). This upper limit was determined from the maximum load capacity of the loading device (25 KN) and the cross-sectional area of the specimen (50 mm in diameter), corresponding to an average axial stress of approximately 12.5 MPa. The stepwise loading scheme allows the progressive closure

and deformation of the internal discontinuity to be captured under increasing stress while keeping the applied load within the safe operating range of the in-situ device and the CT system. For each loading stage, 1000 CT images were acquired to provide sufficient resolution for subsequent DVC-based displacement and strain field analysis.

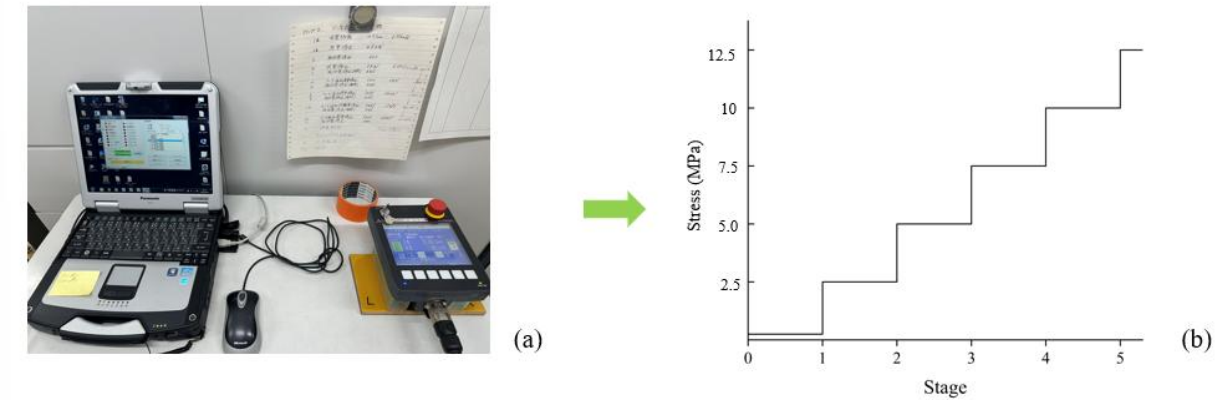

Fig. 3.6: Loading stage.

To obtain detailed information on the internal fracture geometry, a high-precision micro-focused CT mode was employed. For each scan, the specimen was imaged over its full height from top to bottom, yielding 1,000 tomographic slices at intervals of 100 µm. This resulted in a stack of grayscale images, each with a resolution of 1000 × 1000 pixels. Representative images of a longitudinal cut section are shown in Fig. 3.7. A, B, C, and D in this figure correspond to the specimen ids in Table 3.1. To enhance the extraction of fracture information, the cross-sectional images were segmented using a region-growing approach. For each region to be identified, a seed pixel was randomly selected as the initial point, and neighboring pixels with similar grayscale values were iteratively merged until a prescribed gray-level threshold was reached. In the segmented images, the filler-bearing fracture is highlighted in yellow, whereas the intact rock-like matrix appears in gray. By applying this segmentation procedure successively to all 1000 slices, the entire prefabricated fracture was extracted, and a three-dimensional CT-based model of the specimen containing the internal fracture network was reconstructed.

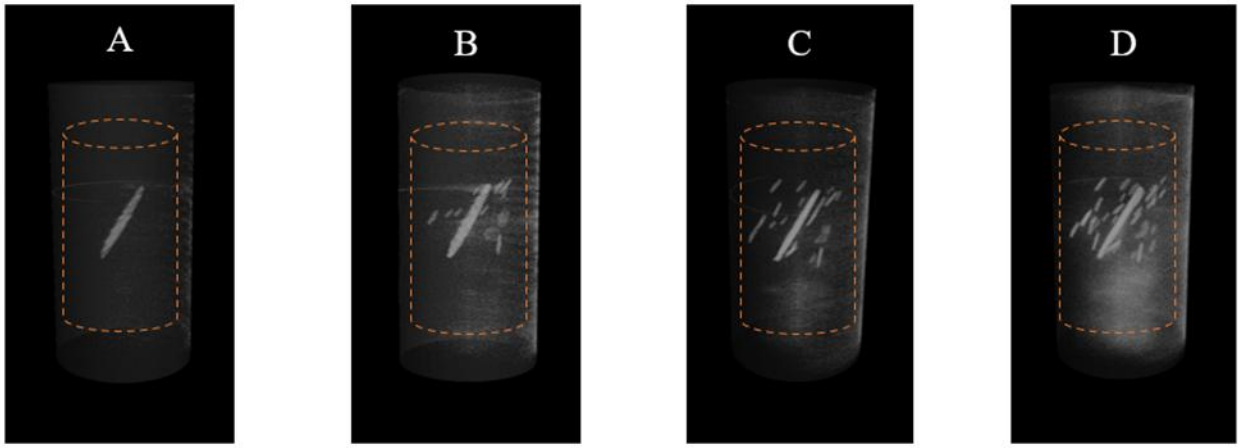

Fig. 3.7: Cross-sectional images of 3DP specimen.

3.3 Experimental results and discussion

3.3.1 Accuracy verification

The 3D-printed specimens were designed to represent simplified fault damage zone analogues, consisting of a cylindrical rock-like matrix with a single, fully embedded horizontal discontinuity at mid-height (Fig. 3.8). The specimen has a diameter of 50 mm and a height of 100 mm, and the prefabricated internal discontinuity has a diameter of 30 mm and a nominal aperture of 1.2-2.0 mm. This configuration allows deformation to preferentially localize along the internal discontinuity under axial loading, while minimizing boundary effects. During the loading tests, X-ray CT scans were acquired at each loading stage (0 to 5), providing three-dimensional grayscale images of the internal structure and deformation evolution (Fig. 3.9). These CT images serve as the input for the subsequent digital volume correlation (DVC) analysis.

Before using the CT image data for the deformation characteristics of damage zones, it is necessary to verify the reliability of the measured deformation fields. In this study, three-dimensional digital volume correlation (DVC), a well-established image-based technique for full-field internal deformation measurement (Bay. 2008; Hussein et al., 2012; Buljac et al., 2018), was performed on the CT images using the SPAM-IDIC code, which has been widely applied in previous studies for quantitative analysis of internal displacement and strain fields in geomaterials (Pan et al., 2009, 2011; Su et al., 2020). The strain field was visualized and examined to check whether the overall deformation pattern is consistent with the expected mechanical behaviour of the specimen.

To reduce the computational cost while still capturing the region of interest around the internal discontinuity, a cylindrical subvolume was extracted from the full specimen volume, as illustrated in Fig. 3.10a. The selected region has a height of 800 pixels and a diameter of 200 pixels, centred on the prefabricated horizontal fracture. This subvolume encompasses the entire fracture plane and a sufficient portion of the surrounding rock-like matrix, allowing strain localization along the discontinuity to be clearly identified without unnecessary processing of regions far from the fracture.

Fig. 3.10b presents the deviatoric strain field obtained from SPAM-IDIC within this subvolume. A pronounced band of high deviatoric strain is observed at the elevation corresponding to the internal fracture, whereas the surrounding matrix exhibits relatively low and smoothly varying strain. This pattern indicates that deformation is strongly localized along the prefabricated discontinuity, which is fully consistent with the imposed loading condition and the specimen design. No strain concentrations are observed near the specimen boundaries or at locations unrelated to the fracture, suggesting that the DVC analysis does not suffer from significant artefacts or miscorrelation.

The good agreement between the mechanically expected deformation mode and the computed deviatoric strain field confirms that the SPAM-IDIC results are physically reasonable. Therefore, the axial displacement fields obtained from the DIC analysis are considered sufficiently accurate and are used in the subsequent calculation of the equivalent normal stiffness of the internal fractures.

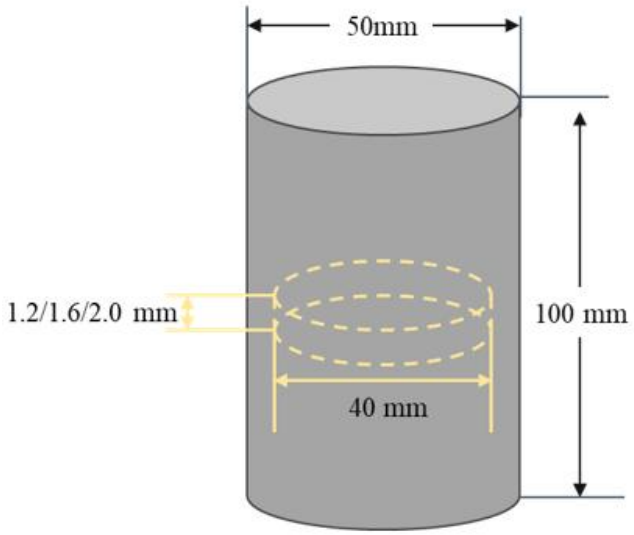

Fig. 3.8: Geometry and internal discontinuity of the 3D-printed specimen.

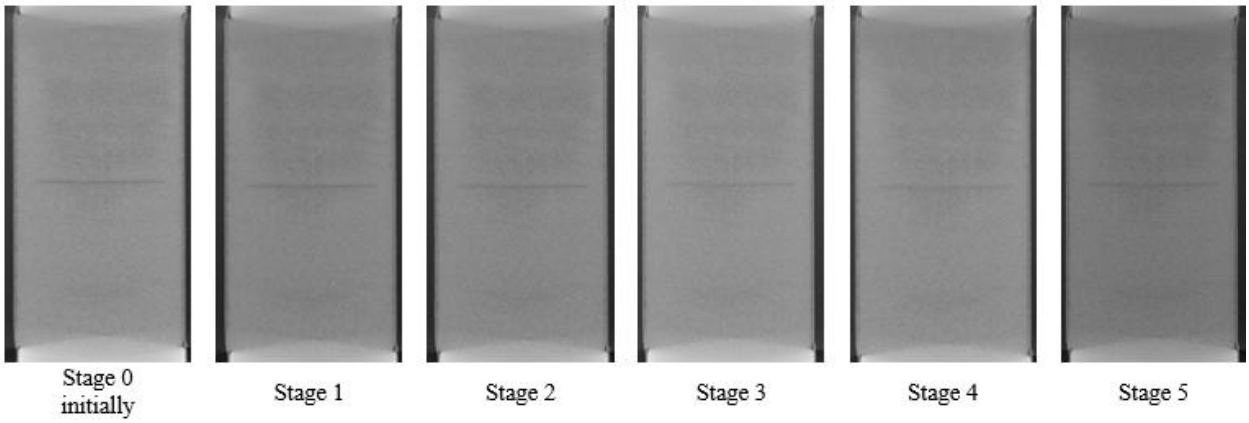

Fig. 3.9: CT images acquired at different loading stages.

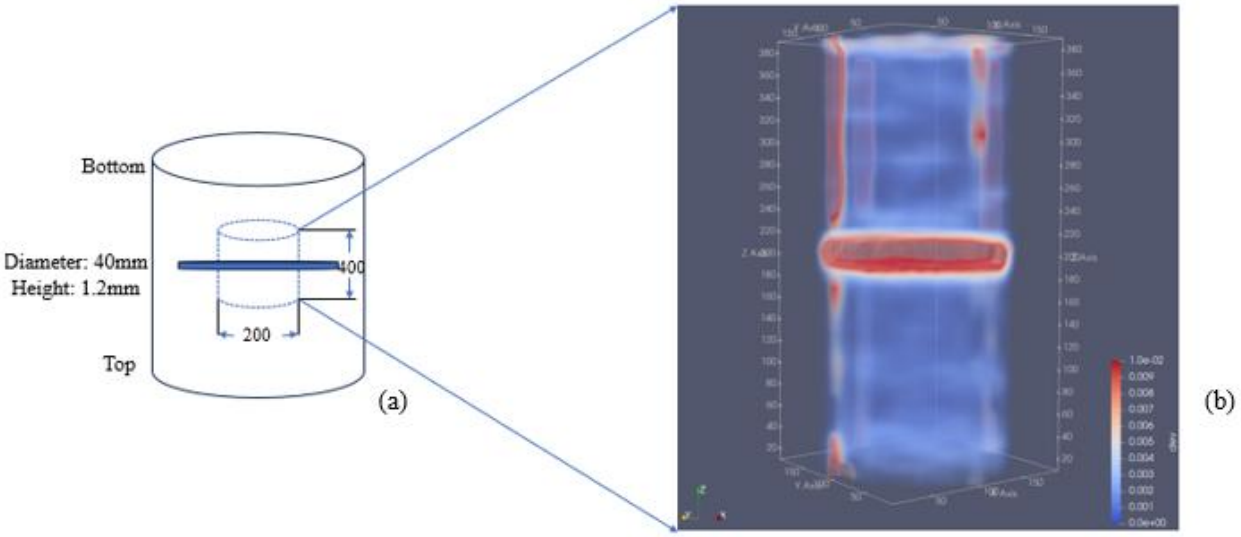

Fig. 3.10: Calculation region and deviatoric strain distribution.

3.3.2 Calculation methodology

Figure 3.11 schematically illustrates the procedure adopted for digital volume correlation (DVC) analysis based on X-ray computed tomography (CT) images. High-resolution three-dimensional CT images were first acquired for each 3D-printed cylindrical specimen under different loading stages. These volumetric datasets provide a detailed representation of the internal structure, including the prefabricated fault core and the surrounding damage-zone fractures.

To accurately resolve the internal strain field while maintaining computational efficiency, subvolumes were extracted from the original CT datasets prior to DVC analysis. Direct application of DVC to the entire specimen volume would significantly increase computational cost and may

introduce unnecessary noise from regions far from the mechanically relevant zone. Therefore, a hierarchical subvolume selection strategy was adopted. First, a cylindrical subvolume with dimensions of 700 × 700 × 1400 pixels was extracted from the central part of the specimen. This region corresponds to the portion of the specimen subjected to relatively uniform boundary conditions during loading and excludes regions influenced by end effects near the loading platens. The cylindrical geometry also preserves the original specimen symmetry, ensuring that the extracted volume remains representative of the global deformation behavior. Within the cylindrical subvolume, a smaller cubic region encompassing the fault core and the surrounding damage zone was further selected for detailed strain analysis. This cubic subvolume focuses explicitly on the mechanically active region where strain localization, displacement discontinuities, and heterogeneous deformation are expected to develop. By isolating this region, the local strain field associated with the internal discontinuities can be quantified with higher spatial resolution. Digital volume correlation was performed using the SPAM software package. The node spacing was set to 20 pixels, and a half-window size of 10 pixels was employed for the correlation analysis. These parameters were selected as a compromise between spatial resolution and correlation stability, allowing reliable strain measurements while retaining sufficient sensitivity to localized deformation features within the fractured damage zone. In addition, a gray-level threshold of 30,000 was applied to exclude low-intensity voxels corresponding to pores or background noise. This preprocessing step improves the robustness of the correlation by ensuring that only voxels with sufficient texture and contrast contribute to the displacement and strain calculations. All DVC parameters were kept constant for all specimens to ensure consistency and comparability of the measured strain fields.

The resulting three-dimensional displacement and strain fields obtained from the DVC analysis provide a quantitative basis for evaluating deformation heterogeneity and strain localization within the fault damage zone analogue. These experimentally derived strain fields are subsequently used to interpret the mechanical role of distributed internal discontinuities and to inform the apparent stiffness characteristics discussed in later sections.

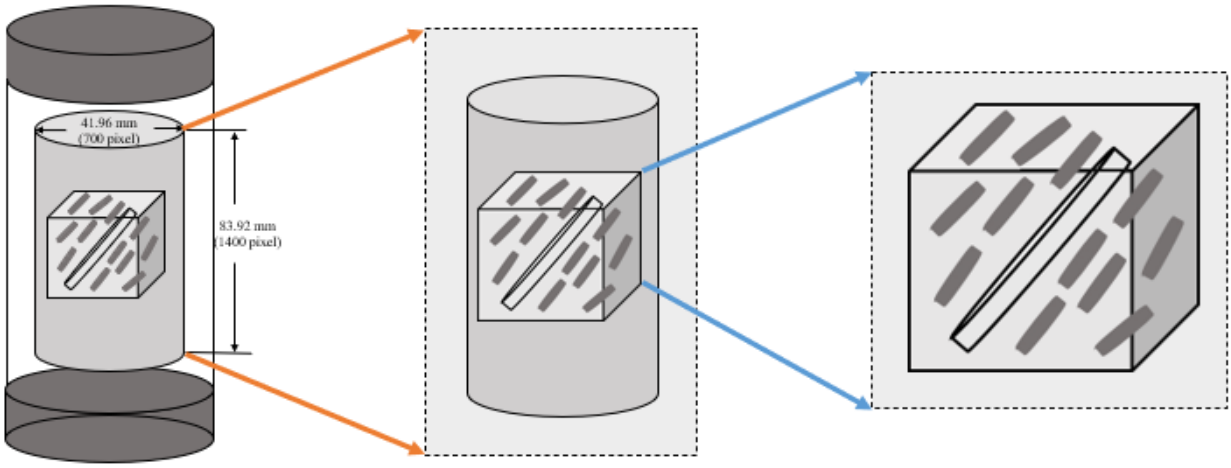

Fig. 3.11: Hierarchical subvolume selection from X-ray CT images.

3.3.3 Strain distribution in damage zone

Figure 3.12 shows the distribution of calculated strain fields using DVC results. It should be noticed that in the DVC-derived strain fields, a vertical band of unrealistically high strain is observed along the outer boundary of the cylindrical specimens, as highlighted by the red regions. This feature does not represent actual material deformation but is a numerical artifact associated with the DVC analysis. The artifact arises from the geometric mismatch between the cylindrical specimen and the cubic correlation windows employed in the DVC algorithm. Near the curved outer surface, a significant portion of the cubic subvolumes extends into the surrounding air, resulting in insufficient gray-level information and unstable correlation. Consequently, artificially large displacement gradients and spurious high strain values are produced.

In addition, the SPAM-IDIC framework places correlation nodes uniformly on a Cartesian grid. Nodes located close to the curved specimen boundary therefore do not satisfy the correlation quality requirements, further contributing to inaccurate strain estimation in these regions. Such numerical artifacts typically form a continuous high-strain band near the cylindrical surface and are absent when the region of interest is strictly cubic. Accordingly, the high-strain bands observed near the specimen boundary are excluded from the following interpretation of strain distributions within the damage zone.

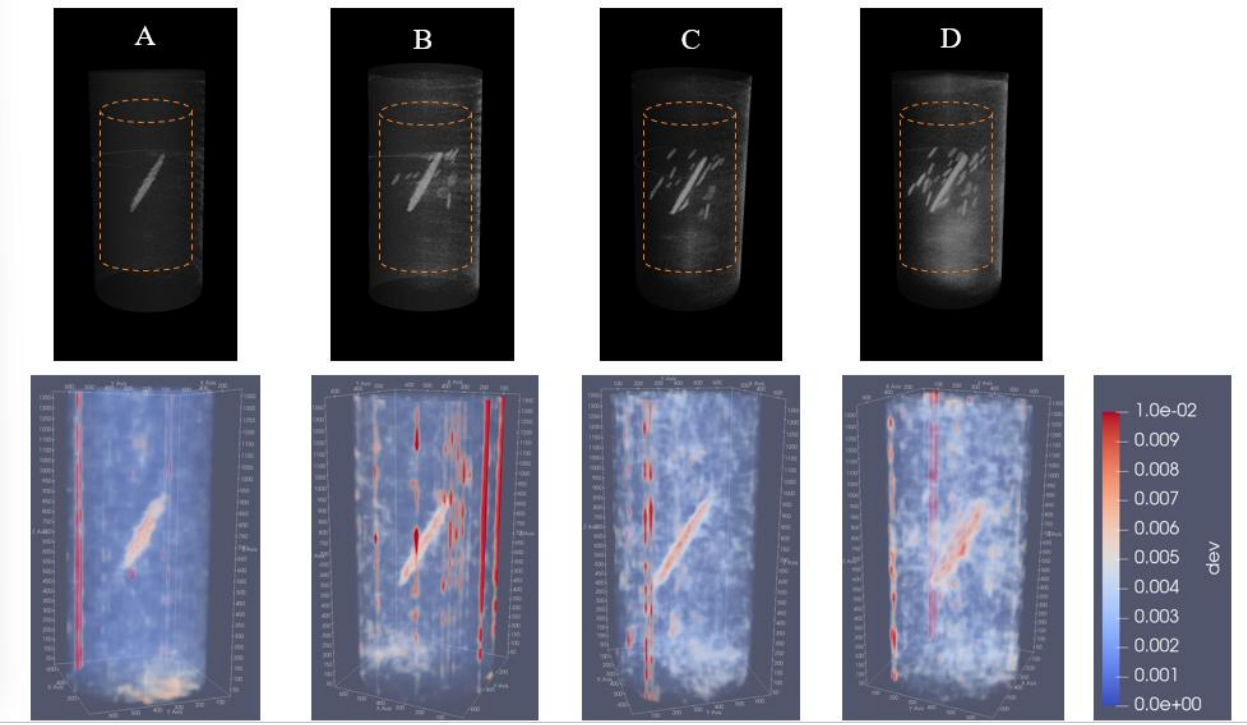

Fig. 3.12: Three-dimensional strain distributions in cylindrical specimens with different damage-zone fracture densities.

Figure 3.12 compares the three-dimensional strain distributions within the damage zone for specimens with different fracture densities. Panel A corresponds to the specimen containing only a single fault core without surrounding fractures, while Panels B, C, and D represent specimens with damage-zone fracture densities of P32 = 10, 20, and 30, respectively (shown in Table.3.1).

In the single fault-core specimen (Panel A), the strain field within the damage zone is relatively homogeneous, with deformation largely concentrated along the prefabricated fault core. Minor strain fluctuations are observed, but no pronounced strain localization develops away from the fault core, indicating a comparatively simple internal deformation pattern. With the introduction of surrounding fractures (Panels B-D), the strain distribution within the damage zone becomes progressively more heterogeneous. For P32 = 10 (Panel B), localized strain concentrations begin to appear around individual fractures, leading to a departure from the nearly homogeneous strain field observed in Panel A. As the fracture density increases to P32 = 20 (Panel C), strain localization becomes more pronounced and spatially distributed, reflecting increased mechanical interaction among neighboring fractures. In the highest fracture-density case (P32 = 30; Panel D), the entire damage zone exhibits a highly complex strain distribution. Multiple zones

of elevated strain are observed throughout the damage zone, and deformation is no longer confined to the vicinity of the main fault core. This indicates that distributed fractures play a dominant role in controlling the internal deformation behavior at high fracture densities.

Overall, the DVC results demonstrate a clear transition from relatively homogeneous deformation in the absence of surrounding fractures to strongly heterogeneous strain distributions as the damage-zone fracture density increases.

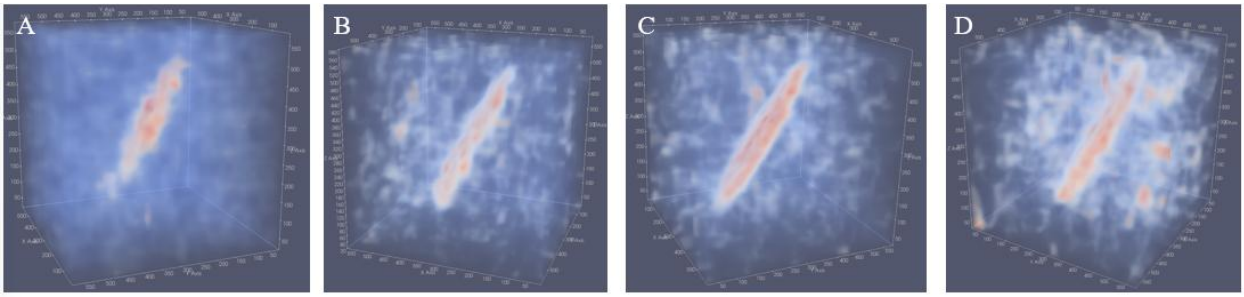

Fig. 3.13: Strain distribution within the extracted damage-zone subvolume for different fracture densities.

To facilitate a clearer comparison of strain distributions within the damage zone and to improve the robustness of subsequent quantitative analyses, the strain fields were further examined within a cropped subvolume centered on the damage zone. Specifically, a cubic region with dimensions of 600 × 600 × 600 pixels was extracted from the original DVC results, enclosing the fault core and the surrounding fractured region while excluding areas dominated by boundary-related artifacts.

Figure 3.13 presents the strain distributions within the extracted damage-zone subvolume for specimens with different fracture densities (A-D). In the specimen containing only a single fault core (Panel A), strain localization occurs almost entirely along the fault core, forming a single, sharp shear band. The surrounding region exhibits relatively low and spatially uniform strain, indicating limited deformation away from the main discontinuity. With the introduction of distributed fractures (Panels B-D), the strain field within the damage zone becomes progressively more complex. For P32 = 10 (Panel B), the fault-core–dominated shear band remains the primary deformation feature, while a small number of secondary strain concentrations appear around the core. As fracture density increases to P32 = 20 (Panel C), the shear band becomes wider and more continuous, and strain is increasingly distributed throughout the damage zone. In the highest

fracture-density case (P32 = 30; Panel D), strain localization is no longer confined to a single dominant shear band. Instead, strain becomes widely scattered within the damage zone, with multiple minor shear paths developing throughout the fractured region. This results in a highly heterogeneous deformation pattern, reflecting the strong mechanical interaction among distributed internal fractures.

Overall, the cropped damage-zone analysis reveals a systematic transition in deformation behavior with increasing fracture density, from a fault-core-dominated shear band to a broader, more distributed, and more complex strain field within the damage zone. These results clearly demonstrate that the strain distribution within the fault damage zone is highly heterogeneous and spatially complex.

3.4 Concluding marks

In this chapter, a CT- and DVC-based experimental framework was developed to investigate the internal deformation behavior of fault damage zone analogues using 3D-printed (3DP) rock-like specimens. Cylindrical specimens containing a prefabricated fault core and surrounding distributed fractures were fabricated to represent simplified fault damage zone structures. High-resolution X-ray CT imaging combined with three-dimensional digital volume correlation (DVC) enabled direct visualization and quantification of internal displacement and strain fields during loading. The main findings of this chapter can be summarized as follows:

1. The CT-DVC based analysis successfully captured three-dimensional strain localization and heterogeneous deformation within the specimens. Strain fields obtained from DVC exhibit mechanically reasonable patterns, with deformation concentrated along the fault core and distributed fractures, confirming the reliability of the adopted imaging and correlation procedures for investigating internal deformation in fractured media.

2. The strain distribution within the damage zone becomes progressively more heterogeneous and spatially complex with increasing damage zone complexity. In specimens containing only a single fault core, deformation is dominated by a narrow shear band localized along the fault core. With the introduction and subsequent increase of distributed fractures in the surrounding damage zone, strain localization broadens and multiple deformation paths develop, leading to a strongly non-uniform internal strain field.

3. These experimental observations provide direct evidence that the strain state within fault damage zones is inherently heterogeneous. The results highlight the limitations of homogeneous or simplified mechanical representations and emphasize the importance of explicitly accounting for internal structural complexity when modeling near-fault regions.

4. Numerical investigations on the impacts of fracture stiffness on seismic source parameters at the fracture scale

4.1 Introduction

Building on the experimental observations presented in Chapter 3, where pronounced strain anisotropy was identified within damage zones, it becomes evident that the heterogeneous mechanical responses of fractured rock masses cannot be represented by isotropic medium alone. In particular, the development and interaction of fractures lead to abnormal and spatially heterogeneous stress-strain states that play a critical role in fault-slip processes and seismic energy release.

To address this, Chapter 4 employed the discrete element method (DEM) using 3DEC, in which fractures are explicitly represented through a discrete fracture network (DFN) embedded with damage zones. By explicitly incorporating fracture geometry and mechanical properties, this chapter focuses on quantifying (1) how fracture stiffness and (2) variations in fracture normal and shear stiffness (K_n and K_s) influence fault-slip behavior and associated seismic source parameters under mining-induced stress perturbations.

4.2 Numerical model with discrete fracture network

The numerical model incorporating a fracture network is developed using 3DEC, a three-dimensional numerical program based on the distinct element method for discontinuous media simulation. A cubic model with dimensions of 10 meters per side is employed. Fractures are incorporated into the model following their subdivision into smaller cubic elements using vertical and horizontal planes.

The generation of discrete fracture network within the fault damage zone requires the specification of key parameters, including fracture density, length, and orientation. Fracture density can be employed with the following power law function (Agosta et al., 2010):

$$P_{10} = \alpha d^{\beta} \tag{5.1}$$

where, the coefficient α corresponds to the maximum fracture density adjacent to the fault core; β serves as a scaling factor; and d represents the distance from the fault core. Regarding fracture length, a cumulative density function is employed (Gutierrez and Youn. 2015).

$$F(l) = \frac{l_{min}^{1-a} - l^{1-a}}{l_{min}^{1-a} - l_{max}^{1-a}} \tag{5.2}$$

where a determines the ratio of small to large fractures in the network; l_{max} and l_{min} define the maximum and minimum fracture lengths, respectively. Finally, the orientation of fractures is defined using the Fisher function, as described by the following equation (Fisher. 1995).

$$f(\theta) = \frac{k \sin \theta e^{\cos \theta}}{e^{k} - e^{-k}} \tag{5.3}$$

where k and θ denote the Fisher constant and the angular deviation from the mean vector, respectively. These equations are employed to statistically generate disk-shaped fractures within the fault damage zone. The parameters employed in Eqs. (5.1) to (5.3) are as follows: $\alpha = 30$, $\beta = 0.8$, $l_{min} = 2$ m, $l_{max} = 10$ m, $a = 2.5$ and $k = 40$. These parameters are verified and their influence on the stress state within the fault damage zone is investigated (Sainoki et al., 2021). Lastly, the discrete fracture network was constructed, comprising approximately several thousand disk-shaped fractures. The fault core, centrally located in the model, is defined as a major joint set with a vertical orientation along the y-direction. The densely spaced green planes in Fig. 5.1b represent fractures, while the red plane (Fig. 5.1a) corresponds to the fault core.

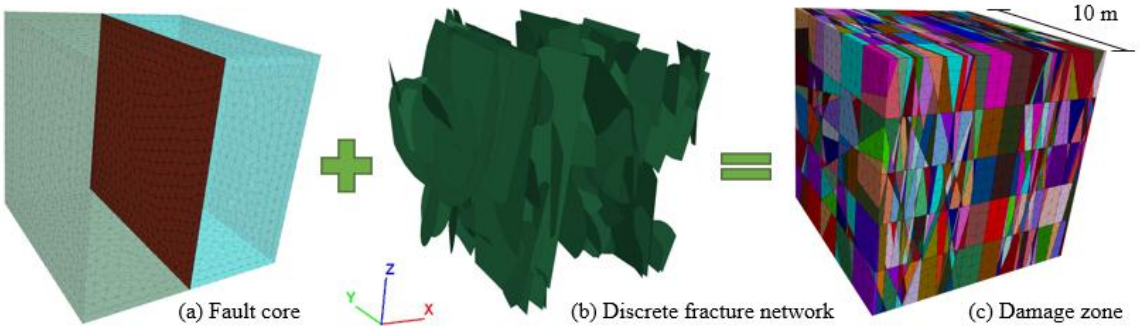

Fig. 4.1: Model construction.

However, in this study, fractures in the discrete fracture network were generated starting from a distance of 1 m away from the fault core. This modeling choice was made because preliminary analyses revealed that when fractures are constructed immediately adjacent to the fault core, increases in pore pressure within the fault do not induce slip; both shear and normal stresses on the fault remain nearly unchanged, as shown in Fig. 5.2. The id on the X-axis represents the sub-contacts on the fault core. This behavior is likely due to the direct mechanical interaction between discontinuities and the fault core, whereby the presence of closely spaced fractures restricts slip initiation along the fault plane. To eliminate this unintended stabilizing effect and to allow fault

slip to occur under pore pressure increase, the fracture network was constructed beginning 1 m away from the fault. Under this configuration, the fault responds to pore pressure changes and undergoes slip as expected. A detailed explanation of these observations and their mechanical implications is provided in the following sections.

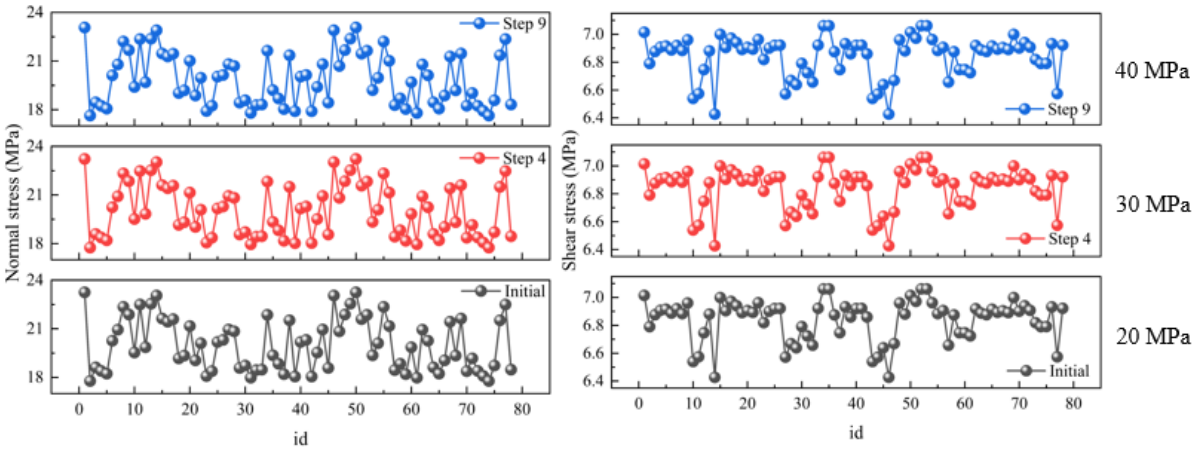

Fig. 4.2: Stress reduction on the fault for fractures attached to the fault.

4.3 Verification of the model

To verify that the numerical framework is capable of reproducing fault slip driven by pore-pressure increase, an additional validation step was conducted by systematically examining the influence of the discrete fracture network. As demonstrated in Section 5.2, when fractures in the DFN were generated immediately adjacent to the fault core, increases in pore pressure within the fault did not lead to slip. Both the normal and shear stresses on the fault remained almost unchanged, indicating that the fault was mechanically stabilized by the presence of closely spaced fractures. This behavior suggested that the DFN itself, rather than the fault or boundary conditions, was suppressing slip initiation.

To confirm that the theoretical mechanism is valid and to isolate the effect of the DFN, the model was first tested without any fractures, that is, the DFN generation step was removed while all other parameters and loading conditions were kept identical. The results of this validation are shown in Fig. 5.3. When pore pressure was increased along the fault plane, distinct fault slip was observed, accompanied by a clear reduction in shear stress within the slipping zone. This behavior is fully consistent with the expected physical response: elevated pore pressure reduces effective normal stress, thereby triggering shear failure along the fault. These results verify that the modeling framework and loading conditions are fundamentally sound, and that the fault is capable of

undergoing slip under pore-pressure increase in the absence of fractures.

Having confirmed that the fault responds correctly without the DFN, the next step is to reconsider the design of the fracture network. The comparison clearly indicates that the original fracture placement strongly constrained fault slip, preventing stress redistribution and slip development. Therefore, the DFN cannot simply be constructed in the same manner as in the continuum model. Instead, the generation of fractures must be modified to avoid direct mechanical interference with the fault core. This observation motivated the modeling decision described in Section 5.2, where fractures were generated starting 1 m away from the fault. Under this configuration, the fault is no longer mechanically locked by the DFN and is able to slip in response to pore-pressure changes, ensuring a physically realistic representation of the near-fault mechanical behavior.

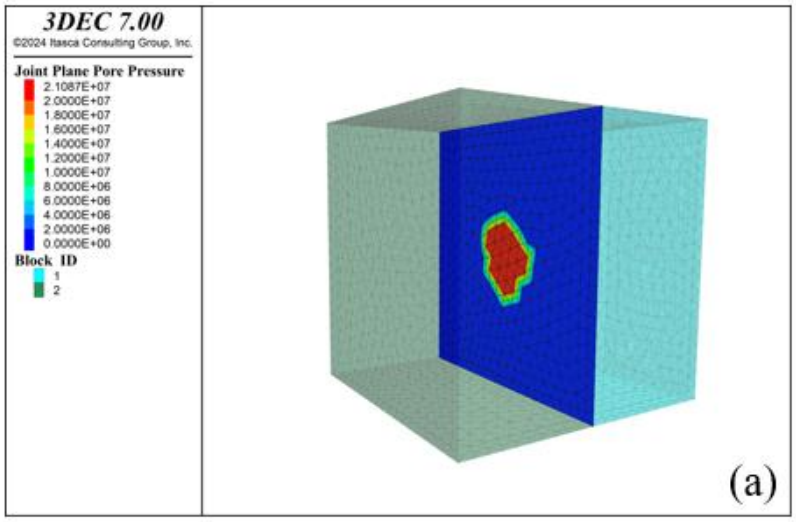

Fig. 4.3: (a) Stress reduction on the fault and (b) slip in this region.

4.4 Input parameters

The host rock within the fault damage zone is assumed to be granite. The Young's modulus of the intact rock is set to 60 GPa (Armaghani et al., 2016; Domede et al., 2019; Yang et al., 2019), with the Poisson's ratio of 0.2, which falls within the typical range of 0.17 to 0.30 (Tarkov and Vavakin. 1982; Gercek. 2007; Ji et al., 2018). A density of 2600kg/m^3 is also applied to the model (Sainoki et al., 2023). The normal and shear stiffnesses of the fractures, denoted as K_{n} and K_{s}, are set to 30 GPa/m and 10 GPa/m, respectively. This setting reflects a commonly assumed normal-to-shear stiffness ratio of 3.0, as suggested by Bandis et al. (1983). The selected stiffness values fall within a reasonable range reported in previous studies for granite and carbonate rocks (Eftekhari et al., 2014; Konstantinovskaya et al., 2014).

The fault core is assigned a friction angle of 30°, a value supported by previous studies (Barton. 1976), and zero cohesion (Barton et al., 1974). The Coulomb's shear strength model with a slip-weakening law is then adopted. Specifically, when the shear stress on the fault exceeds the shear strength defined by the Coulomb's criterion, the friction angle is instantaneously reduced from 30° to 20°. Maintaining the same normal-to-shear stiffness ratio, K_{n} and K_{s} for the fault core are assigned to 30.0 GPa/m and 10 GPa/m, respectively. The stiffness settings are the same as those of the fault because, in this case, their dimensions are similar. These values are commonly adopted in numerical simulations to represent the mechanical behaviours of fault cores and are considered to fall within a validated range reported in previous studies (Sainoki and Mitri. 2014).

4.5 Numerical analysis

4.5.1 Analysis procedure

The initial in-situ stress state is first applied to all model boundaries, while displacement at the bottom boundary is constrained in the z-direction and the four top corner nodes are fixed to prevent rigid-body movement, following the same boundary condition settings adopted in the continuum model described in Chapter 4. After establishing the initial stress equilibrium, seismic events are induced by progressively reducing the effective normal stress acting on the fault core. In this study, the reduction in effective normal stress is implemented by increasing the pore pressure within a circular region of radius 1.5 m centered on the fault plane. The pressurized region

represents the localized fluid elevation that commonly triggers fault slip.

The pore water pressure is increased in 10 stages, with an increment of 2 MPa at each stage. Previous studies have demonstrated that this magnitude of pore pressure elevation, corresponding to a sufficiently large reduction in effective normal stress, is capable of inducing fault slip within similar discrete fracture models. As shown in Fig. 5.4, with the progressive increase in pore pressure, the effective normal stress acting on the fault core systematically decreases from about 23-25 MPa to approximately 2-12 MPa, while the shear stress is strongly redistributed and locally reduced from around 5 MPa to values close to zero on the fault. This combined reduction in effective normal stress and shear-stress perturbation drives a number of fault segments to satisfy the Mohr-Coulomb failure condition, thereby promoting the onset of fault slip. Once slip is initiated, seismic source parameters, such as shear displacement, peak particle velocity, seismic moment, and seismically radiated energy are calculated for the surrounding rock mass undergoing shear failure.

Following the base-case simulation, the stiffness of fractures within the discrete fracture network is systematically increased, and the same pore-pressure increment procedure is repeated. Seismic source parameters are again computed for each stiffness condition. By comparing these results with those of the base case, the influence of fracture stiffness on fault-slip behavior and seismic source characteristics can be quantitatively assessed. This analysis framework enables the mechanical role of fracture stiffness to be isolated and evaluated with high resolution, serving as the foundation for the parametric studies presented in the subsequent sections.

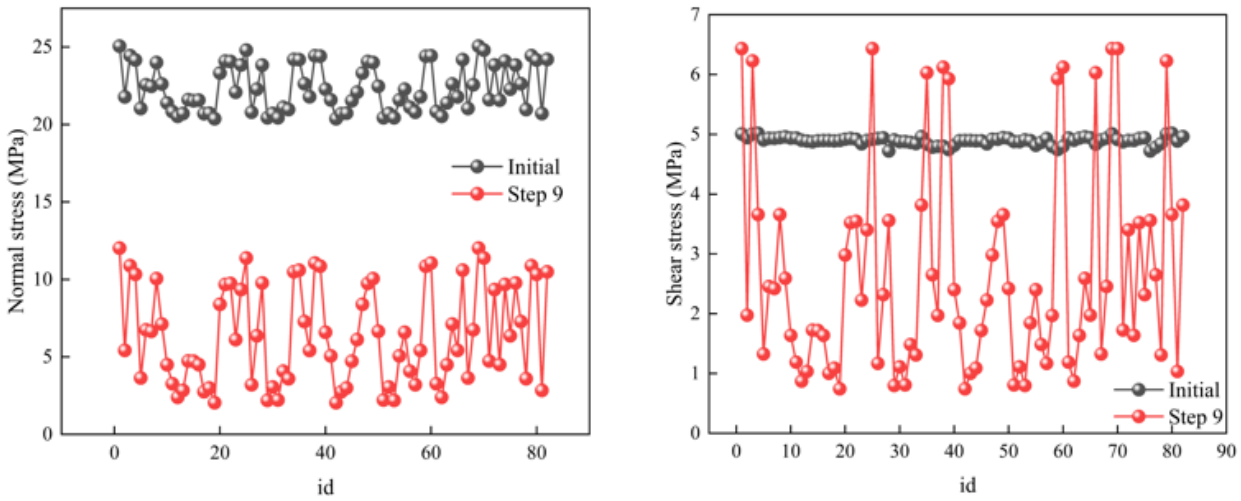

Fig. 4.4: Stress reduction on the fault for fractures located 1 m away from the fault.

4.5.2 Calculation of seismic source parameters

Seismic source parameters, such as seismically radiated energy, seismic moment, and peak particle velocity, serve as key indicators for assessing seismic damage (Trifu et al., 1995; Bormann et al., 2013; Sainoki et al., 2015; Nordström et al., 2017). A decline in these parameters indicates a potential mitigation of seismic hazards. To investigate the potential of enhancing fracture stiffness as a seismic risk reduction strategy, a parametric study is conducted to evaluate the effect of increasing fracture stiffness on these parameters.

An essential parameter in characterizing the strength of an earthquake is the seismic moment (M_0), which quantifies the energy released during fault slip (Wyss and Brune. 1968; Madariaga. 1979). The seismic moment is defined by the following equation (Aki. 1966):

$$M_0 = \mu D S \tag{5.4}$$

where μ is the shear modulus of the surrounding rock, D is the average shear displacement on the fault, and S is the fault area that slipped. In this study, the seismic moment is calculated for each induced seismic event based on the mechanical response of the model, allowing a quantitative assessment of how variations in fracture properties influence seismic source behaviour.

Another key seismic source parameter is the seismically radiated energy (E_R), which is the portion of energy released during fault slip that is radiated as seismic waves (Venkataraman and Kanamor. 2004). The seismically radiated energy can be estimated by integrating the energy flux over time and space during rupture propagation (Kanamori. 2001):

$$E_R = \left(\int \frac{\rho \beta}{2} \int \dot{u}^2 \, dt \right) dS \tag{5.5}$$

where ρ and β represent the density of the surrounding rock mass and shear wave velocity, respectively; t and $\dot{u}$ are time and slip rate, respectively. By evaluating both M_0 and E_R, this study offers a comprehensive assessment of the seismic response associated with varying fracture conditions.

4.6 Simulation results and discussion

4.6.1 Effect of fracture stiffness on seismic source parameters

Fig. 5.5 represents the variation in seismic source parameters as a function of fracture stiffness in the base case. The values are normalized with respect to those obtained when the normal and

shear stiffness of fractures are 30 GPa/m and 10 GPa/m, respectively. As shown in the figure, increasing fracture stiffness leads to a substantial reduction in all parameters. When the fracture stiffness increases fivefold, the radiated energy and seismic moment both decrease to approximately 50%-60% of their original values. This notable decrease can be attributed to the enhanced resistance to fault slip and deformation provided by stiffer fractures, which limits slip accumulation and reduces the amount of energy released. Whereas the peak particle velocity and maximum shear displacement decrease to about 65% and 84%, respectively. The reduction level of seismic source parameters obtained in this chapter is slightly weaker than that observed in the continuum simulations presented in Chapter 4, where seismic source parameters decreased to approximately 40% of their baseline values. This difference can be primarily attributed to variations in fracture density and spatial distribution near the fault between the two modeling frameworks. In the FDM model, fracture density was significantly increased in the vicinity of the fault core to represent a highly damaged near-fault zone, leading to stronger stiffness enhancement effects. In contrast, in the DEM model, fractures were generated starting at a distance of 1 m from the fault to avoid disturbance of the fault stress field, resulting in a relatively lower fracture density directly adjacent to the fault. According to the theoretical slip-weakening analysis in Chapter 2, a fivefold increase in damage zone stiffness can reduce seismically radiated energy to about 40%, but this value is sensitive to the spatial distribution of fractures surrounding the slipping region. Therefore, the results from both the continuum and discrete models are theoretically consistent, and the observed quantitative differences reflect the different representations of near-fault fracture density rather than inconsistencies in the mitigation mechanism itself. These results in this Chapter indicate that all seismic parameters are sensitive to fracture stiffness, but the seismically radiated energy and seismic moment exhibit the strongest reduction, followed by peak particle velocity, while the maximum shear displacement shows the smallest relative change. Physically, stiffer fractures increase the resistance to normal and shear deformation within the fault damage zone, thereby suppressing slip accumulation and limiting the dynamic slip rate.

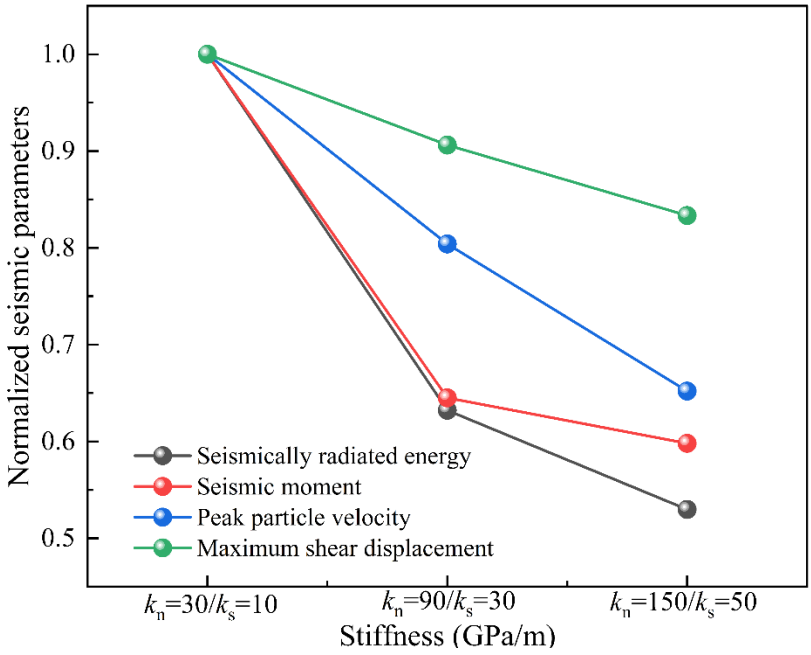

Fig. 4.5: Seismic source parameters change for the base case.

Fig. 5.6a compares the sub-contact slip states on the fault core under two different stiffness configurations. In the case of lower fracture stiffness, numerous slip events are distributed extensively across the fault core, suggesting widespread rupture failure under the condition. In contrast, when fracture stiffness is increased, the number and distribution of slip sub-contacts are considerably reduced, indicating that increased fracture stiffness effectively suppresses slip activity. Stiffer fractures within damage zones tend to mitigate rupture propagation and associated energy release. Fig 5.6b depicts the distribution of near-fault peak particle velocity (PPV). It can be seen from the figure that PPV drops significantly with increasing fracture stiffness. Considering that fracturing in intact rock initiates at a PPV of approximately 0.3 m/s and severe damage occurs beyond 0.6 m/s, the computed PPV of approximately 0.5 m/s in this study remains below the threshold for severe damage (Hedley. 1992). This suggests that the seismic events induced by fault-slip simulated in this study are unlikely to cause substantial structural damage. Nevertheless, the reduction in PPV with increasing fracture stiffness demonstrates that this approach can effectively lower the destructive potential of induced seismicity, further supporting its value as a mitigation strategy. Moreover, the decrease in PPV also implies a reduction in the maximum slip rate on the fault, as the near-field particle velocity is approximately equal to half of the maximum slip rate (McGarr et al., 2002). The consistent reduction in these parameters highlights the effectiveness of

increasing fracture stiffness in mitigating the intensity of induced seismicity.

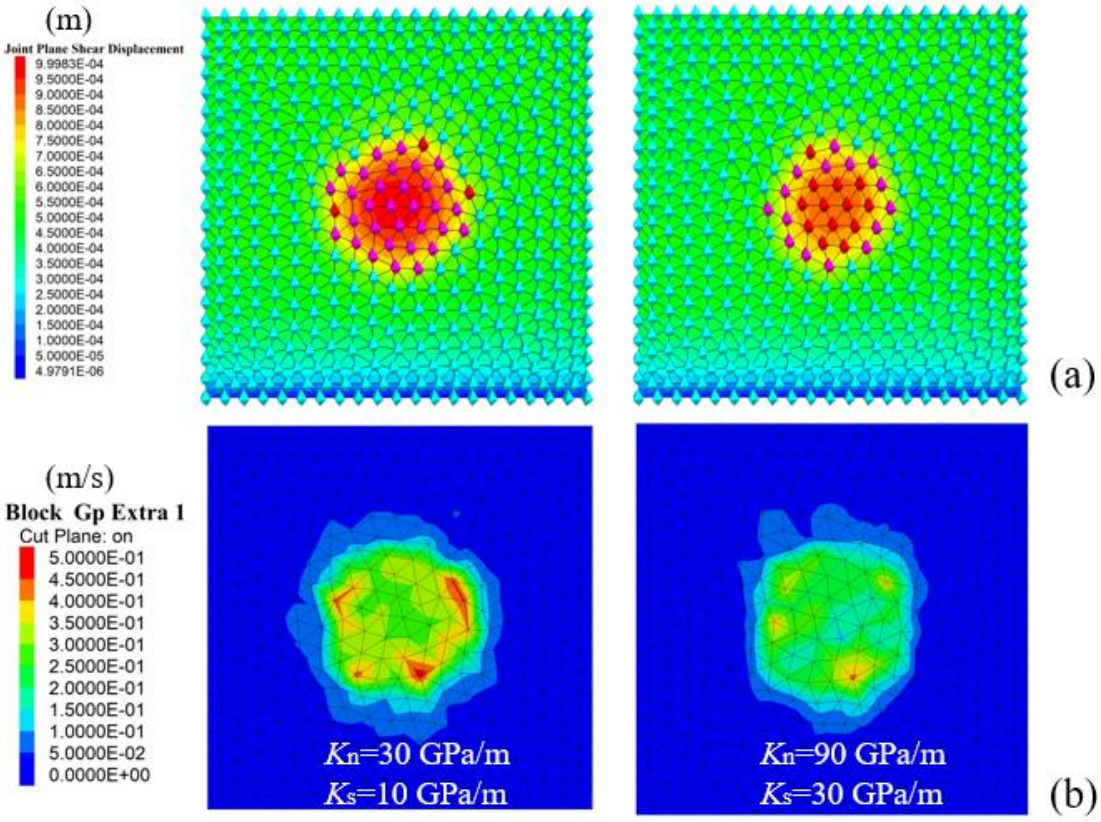

Fig. 4.6: (a) shear displacement and (b) peak particle velocity distribution on the fault.

4.6.2 Effect of fracture stiffness on slip process

Fig.4.7 highlights a clear slip-onset transition and the suppressing effect of stiffness enhancement. Before the dashed line (pre-slip stage), both cases show almost zero shear displacement increment, indicating a stable response with only minor precursory fluctuations immediately before failure. After slip initiates (post-slip stage), the signal becomes highly intermittent and oscillatory, reflecting episodic slip and dynamic weakening during rupture propagation. Importantly, compared with the lower-stiffness baseline case ($K_n = 30, K_s = 10$; black curve), the stiffer case ($K_n = 90, K_s = 30$; red curve) exhibits systematically smaller shear displacement increments and reduced peak amplitudes throughout the post-slip interval. This indicates that increasing the damage-zone stiffness effectively limits the slip rate size of individual slip episodes, thereby constraining the overall slip evolution after instability. In other words, stiffness enhancement increases the effective resistance of the fault–damage system, leading to a more restrained post-failure response and contributing to lower seismic radiation and weaker slip development.

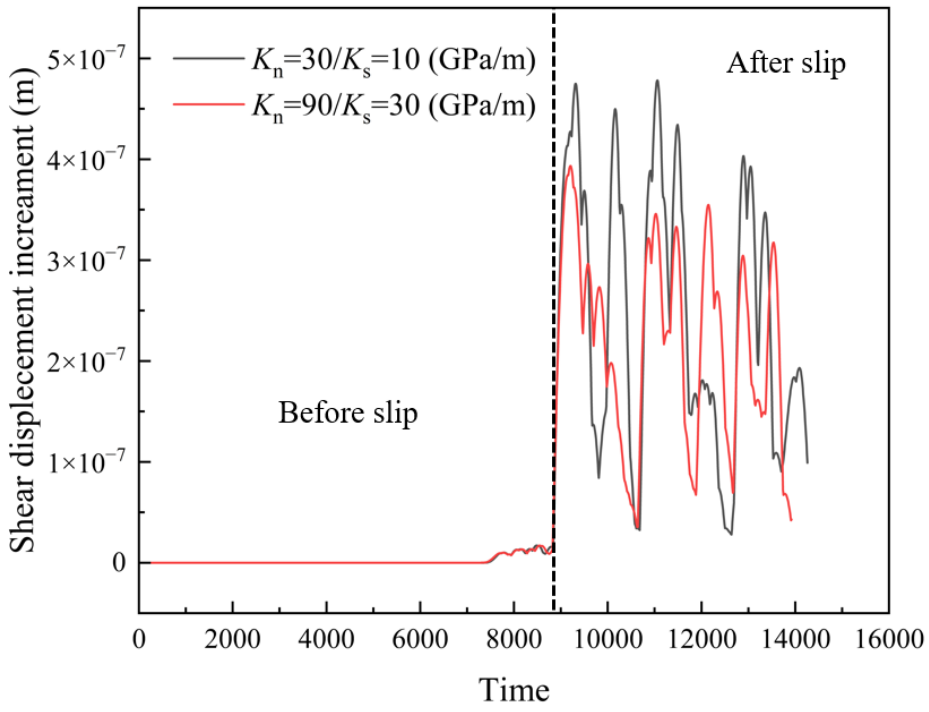

Fig. 4.7: Slip increment under different stiffness conditions.

4.6.3 Comparative influence of normal and shear fracture stiffness

Fig.4.8 compares cases where either K_n or K_s is increased individually from the baseline

($K_n = K_s = 30$), with the y-axis showing normalized seismically radiated energy. A clear contrast emerges between the two stiffness components. Increasing K_n while keeping $K_s = 30$ produces only a modest reduction in radiated energy: the normalized energy decreases from 1.0 to ~0.90 at $K_n = 90$ and to ~0.85 at $K_n = 150$ (about a 10–15% drop). In comparison, increasing K_s while keeping $K_n = 30$ yields a much stronger mitigation effect: the normalized energy drops to ~0.75 at $K_s = 90$ and to ~0.70 at $K_s = 150$ (about a 25–30% reduction). These results indicate that radiated energy is more sensitive to shear stiffness enhancement than to normal stiffness enhancement in the damage zone. Mechanistically, increasing K_s directly increases the shear resistance/constraint of the fault–damage system, limiting slip growth and rupture development and thus reducing energy radiation more effectively, whereas increasing K_n mainly affects normal compliance and closure behavior, providing a weaker direct constraint on shear weakening and slip. In addition, both trends suggest diminishing returns at higher stiffness levels, as the incremental reduction from 90 to 150 is smaller than that from 30 to 90.

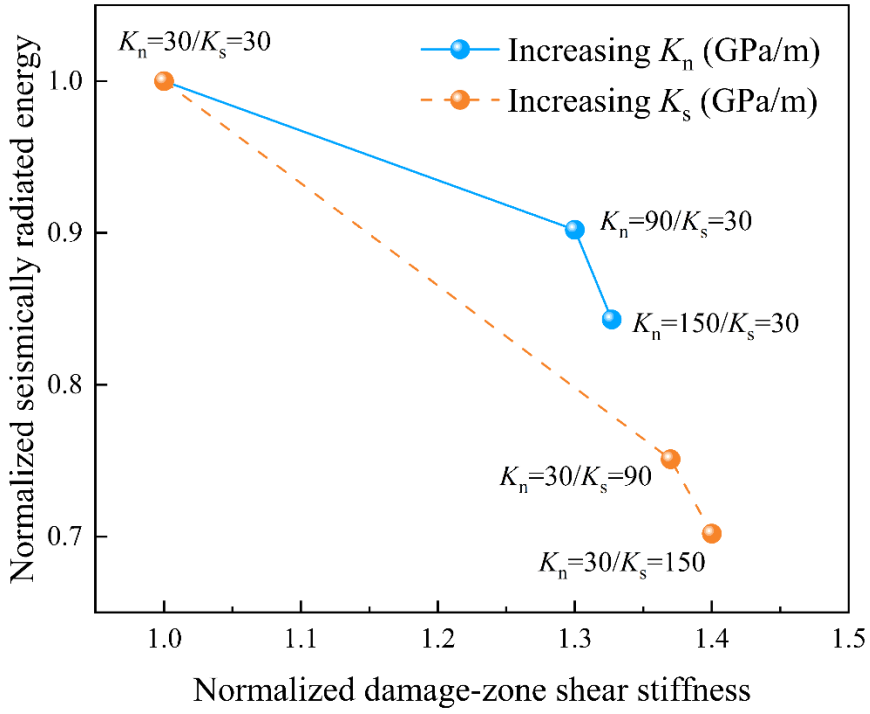

Fig. 4.8: Changes in normalized seismically radiated energy with normal and shear stiffness.

4.7 Concluding remarks

In this chapter, fracture-scale simulations are conducted using 3DEC with an explicitly generated discrete fracture network (DFN) to evaluate how fracture stiffness influences fault-slip behavior. The analyses quantify changes in seismic source parameters, peak particle velocity, and slip distribution resulting from increased fracture stiffness. Parametric studies are also performed by independently increasing the normal stiffness (K_n) and shear stiffness (K_s) to clarify their relative contributions to suppressing induced seismicity. The main conclusions are as follows:

1. Higher fracture stiffness substantially reduces seismic moment, seismically radiated energy, peak particle velocity, and slip extent. With a fivefold increase in stiffness, these seismic parameters decrease to 50% ~ of their baseline values, indicating a clear mitigation effect, as predicted by the slip-weakening framework. The comparatively smaller reduction than continuum-model results is attributed to the lower fracture density and the absence of fractures in the near-fault region, which limits the effective stiffness enhancement where fault slip is most active.
2. The degree of damage and the severity of slip failure progressively decrease as fracture stiffness increases. The stiffer fracture network limits shear displacement increments and suppresses the development of unstable slip, ultimately weakening the overall failure response.
3. A fivefold increase in K_n reduces radiated energy to about 85% of the baseline value and markedly shrinks the slip area, demonstrating strong slip suppression. In contrast, increasing K_s results in significant reductions (70% of baseline energy), and slip distribution changes more. These findings show that K_s is the primary controlling factor for reducing fault-slip intensity.

5. Numerical investigations on the impacts of near-fault fracture stiffness on seismic source parameters at the mine scale

5.1 Introduction

As discussed in Chapter 1, induced seismicity in deep underground mines is strongly influenced by heterogeneous mechanical conditions developed within fault damage zones. Experimental observations presented in Chapter 3 further demonstrate that strain states within damage zones are highly heterogeneous and spatially complex, highlighting the inadequacy of simplified homogeneous representations. While Chapter 4 employed a discrete element method to explicitly resolve fracture-controlled deformation at the local scale, the model size and computational cost inevitably limited the number of fractures that could be represented. As a result, the role of fracture density and its collective influence on mine-scale stress redistribution and fault-slip behavior could not be systematically investigated.

To overcome this limitation and to better represent realistic fault damage zones characterized by a large number of distributed fractures, this chapter adopts a continuum-based numerical approach using FLAC to construct a mine-scale model incorporating an anisotropic damage zone with a high fracture density. Through the crack tensor theory, the cumulative mechanical effects of millions of fractures are embedded into the equivalent constitutive response of the damage zone, enabling simulation of large-scale heterogeneous stress states that are unattainable in discrete fracture models.

Using this framework, the present chapter focuses on (1) quantifying the effect of fracture stiffness on the response of seismic source parameters and (2) systematically assessing the role of fracture density in controlling fault instability and seismic energy release. In doing so, this chapter provides a mine-scale perspective on stiffness-based mitigation strategies that complements the fracture-scale analyses presented in Chapter 4.

5.2 Distribution of fractures in a fault damage zone

Generally, a fault zone is composed of fault core and surrounding fault damage zone (Berg et al., 2005; Lin et al., 2007; Gudmundsson et al., 2010); fault damage zone can be further classified into inner and outer damage zones (Choi et al., 2006; De et al., 2007; Ostermeijer et al., 2020). The fault core is a narrow region typically less than tens of cm in width, whereas the fault damage

zone is a rock mass with densely distributed fractures extending in the direction sub-parallel to the fault core (Fig. 4.1). Field observations reveal that shear displacement in a fault core, mechanical properties of the protoliths, and ambient stress states significantly affect fracture formation and distribution, leading to an asymmetric and heterogeneous damage zone (Faulkner et al., 2011; Mitchell et al., 2011). It is important to note that, despite the various contributing factors, field observations demonstrate that the fracture density in a fault damage zone decreases with the distance from the fault core, indicating a characteristic that the fracture density variation can be approximated with a power low function (Schueller et al., 2013; Johri et al., 2014; O'Hara et al., 2017; Wu et al., 2019), whilst the maximum fracture density near a fault core varies, affected by many factors, such as the mechanical and physical properties of the host rock, ambient stress state, the shear displacement accumulated on the fault core, etc (Ju et al., 2014; Ostermeijer et al., 2010).

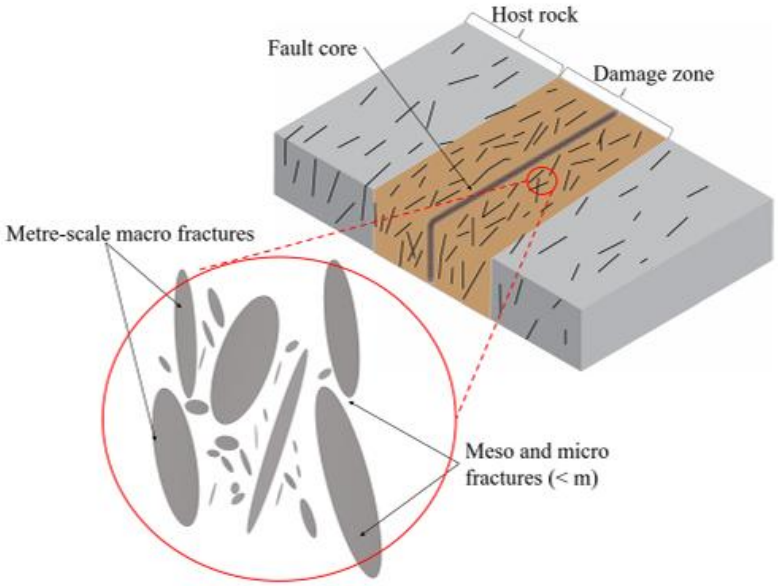

Fig. 5.1: Fault damage zone.

5.3 Generation of discrete fracture network (DFN) model

To generate a discrete fracture network in a fault damage zone, the following parameters need to be determined: fracture density, fracture length, and fracture orientation. Based on previous research, the fracture density can be generated using the following power low function (Agosta et al., 2010).

$$P_{10} = \alpha d^{\beta} \tag{4.1}$$

where α represents a coefficient associated with the maximum fracture density near the fault core; β denotes a scaling factor; d is the distance from the fault core. For the fracture length, the following cumulative density function is adopted (Gutierrez and Youn. 2015).

$$F(l) = \frac{l_{\min}^{1-a} - l^{1-a}}{l_{\min}^{1-a} - l_{\max}^{1-a}} \tag{4.2}$$

where a denotes a scaling exponent that dictates the ratio between smaller and larger fractures; l_{max} and l_{min} represent the maximum and minimum fracture lengths, respectively; Fracture orientation can be determined using Fisher function, which has been widely applied to various studies (Fisher. 1995).

$$f(\theta) = \frac{\kappa \sin\theta e^{\kappa\cos\theta}}{e^{\kappa} - e^{-\kappa}} \tag{4.3}$$

where κ and θ denote the Fisher constant and the angular deviation from the mean vector, respectively. The following parameters are used for Eqs. (4.1) to (4.3): α = 30, β = 0.8, l_{min} = 2 m, l_{max} = 10 m, a = 2.5 and κ = 40. The verification of these parameters and their influence on the stress state within a fault damage zone are detailed in the study (Sainoki et al., 2023). Based on above fracture characteristics, disk-shaped fractures are generated within the fault damage zone, as shown in Fig. 3. The mean dip angle and dip direction of these disk-shaped fractures are assumed to be consistent with those of the fault core. This assumption, however, does not account for potential variations in fracture orientation due to factors such as in-situ stress conditions and the nature of the protolith (Riley et al., 2010; Faulkner et al., 2011; Fletcher et al., 2020). It is noted that fractures generated are macro fractures with a diameter greater than 2 m and less than 10 m. The discrete fracture network (DFN) composed of these macro fractures is then to construct an equivalent continuum model. The meso- and micro- discontinuities (length < 2 m) are not explicitly generated in the DFN model because an extremely large number of discontinuities would be required if they were considered. In addition, the stiffness of large-scale fractures exerts a much greater influence on the stiffness of the fault damage zone compared with that of small-scale discontinuities. Hence, considering both the computational cost and its impact on the simulation results, only large-scale fractures with lengths greater than 2 m are generated in the DFN model. Meanwhile, when calculating equivalent anisotropic compliance matrices, the effect of meso- and micro-discontinuities is implicitly considered by reducing the elastic modulus of the host rock.

The diameters of meso- and micro-discontinuities are considered to be less than two meters, as parameter l_{min} is set to 2 m in Eq. (4.2). The density of meso- and micro-discontinuities is assumed to be constant within the fault damage zone due to insufficient field observations. The generated DFN model is shown in Fig. 4.2.

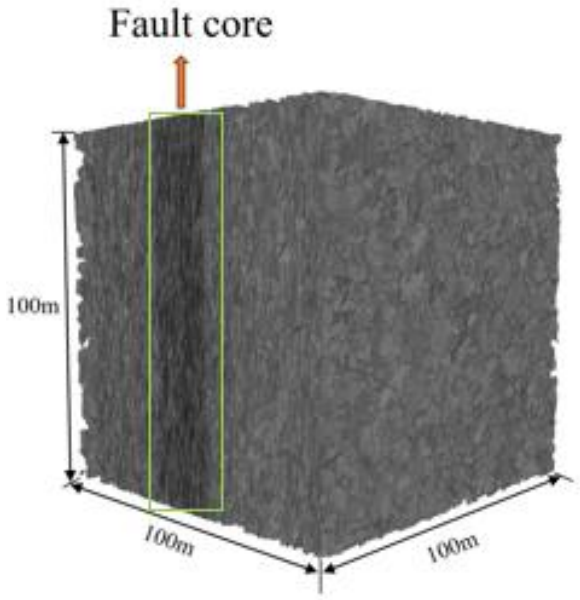

Fig. 5.2: Fracture distribution in a fault damage zone.

5.4 Overall Procedure

The initial stage in simulating heterogeneous stress conditions near a fault combines both continuum and discontinuum methodologies. In the continuum-based procedure, a three-dimensional model is developed using FLAC3D (Itasca Consulting Group) within the finite difference method (FDM) framework. The model is sufficiently large to include an extensive fault system together with the broad fault damage zone commonly observed in deep underground mining environments. This model is hereafter termed the FDM model. From the FDM simulation, a comprehensive list is compiled that specifies the coordinates and dimensions of every zone.

For the discontinuum component, the fracture system within the fault damage zone is characterized in terms of fracture orientations and densities by reviewing a wide range of studies on fault-zone fracture networks. Using these identified characteristics, a three-dimensional discrete fracture network (DFN) is generated so that it covers exactly the same spatial region as the FDM model. Following this, the fracture information corresponding to each zone of the FDM model is

extracted by matching the DFN geometry with the zone list, thereby producing a zone-by-zone dataset that describes the fractures contained within each continuum zone.

After obtaining the information, an equivalent continuum approach is employed to effectively simulate heterogeneous stress regimes. Fig. 4.3 illustrates the procedure for calculating the equivalent continuum model that represents the complex behaviour of the fault damage zone (Sainoki et al., 2023). This method was first proposed and verified by Sainoki et al. (2021). Meso- and micro-discontinuities with lengths less than 2 m are not generated in the fracture network. Instead, their effects on the near-fault rock mass are implicitly considered and calculated by reducing the elastic modulus of intact rock. Hence, the first step involves converting the elastic modulus of intact rock to the elastic modulus of the rock mass including meso- and micro-discontinuities. To this end, the geological strength index (GSI) proposed by Hoek (2007) is utilized to construct an equivalent continuum model representing the fault damage zone. This approach can also be employed to meso-scale discontinuities and the validity has been verified by Sainoki et al. (2021). In this regard, it is assumed that such meso- and micro-discontinuities are randomly oriented and distributed within the fault damage zone, resulting in isotropic elastic behaviour. Thus, the equivalent elastic compliance tensor (M_{ijkl}) of the rock mass with meso- and micro- discontinuities can be obtained.

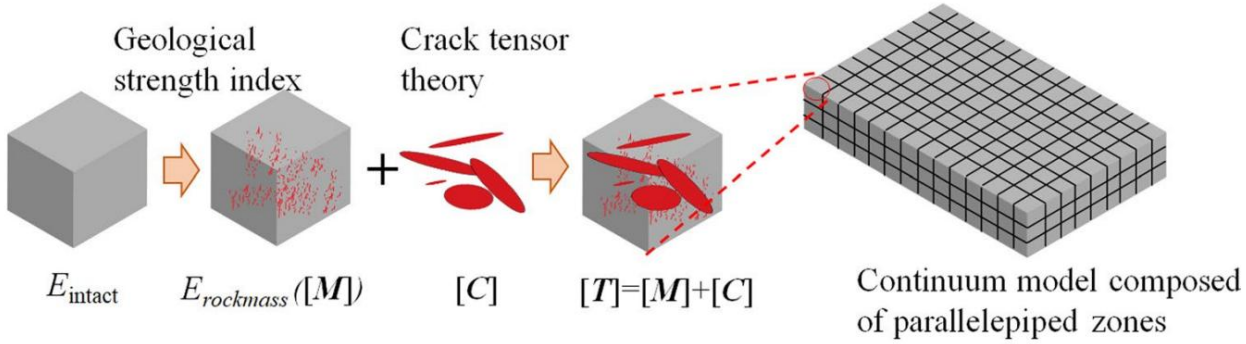

Fig. 5.3: Equivalent continuum model construction.

After calculating M, the crack tensor theory is applied to calculate the elastic compliance tensor C, which corresponds to the elasticity of macro fractures, using the following equations.

$$F_{ij} = \frac{1}{V}\frac{\pi}{4}L^3 n_i n_j \tag{4.4}$$

$$F_{ijkl} = \frac{1}{V}\frac{\pi}{4} L^3 n_i n_j n_k n_l \tag{4.5}$$

$$C_{ijkl} = \sum_{1}^{NCR}\left[\frac{1}{K_n L} - \frac{1}{K_S L}\right] F_{ijkl} + \frac{1}{4K_S L}\left(\delta_{ik}F_{jl} + \delta_{jk}F_{il} + \delta_{il}F_{jk} + \delta_{jl}F_{ik}\right) \tag{4.6}$$

$$T_{ijkl} = C_{ijkl} + M_{ijkl} \tag{4.7}$$

where F and n are the crack tensor and the unit normal vector of the fracture intersecting with the zone, respectively; Here, n_i denotes the i-th component (i=1,2,3) of the unit normal vector of a fracture. Crack tensor F is obtained by weighted averaging over all discontinuities intersecting the zone. C, M and T denote the anisotropic compliance tensor equivalent to the elasticity of discontinuities , the isotropic compliance tensor of the rock mass, and the anisotropic compliance tensor of fault damage zone, respectively; NCR is the total number of fractures intersecting with the zone; K_{n} and K_{s} are normal and shear stiffnesses of the fracture, respectively; δ is the Kronecker's delta; L is the diameter of the fracture. It should be emphasized that the effects of meso- and micro-discontinuities are implicitly incorporated through the reduction of the elastic modulus, whereas the crack tensor introduced in Eq. (4.6) explicitly represents the influence of macro-scale fractures. Therefore, these two steps address different fracture scales and do not double-count their effects. This hierarchical treatment allows the model to reasonably capture fracture-induced anisotropy across different scales in the fault damage zone.

Finally, the anisotropic compliance tensor T considering the effect of all discontinuities and fractures is input to each zone. It is noted that the characteristics of macro fracture, i.e., density, length and orientation, are spatially variable. Accordingly, the anisotropic compliance tensor T also spatially varies for each zone in the model, as T is calculated based on the crack tensor theory and the fracture distribution characteristics in the local region. Hence, a heterogeneous continuum model with anisotropic mechanical behaviour can be constructed.

Fig. 4.4 illustrates the numerical model constructed according to the procedure detailed in Fig. 4.3. The numerical model with a side length of 100 m contains a total of 1 million zone units. The fault core is simulated as a discontinuous plane with interface elements at the center of the model. In this model, the red-colored zones represent regions where the macro fractures modelled in Fig. 4.2 are located. Consequently, the anisotropic compliance tensor T is calculated and then input into these zones. On the other hand, the grey-colored zones corresponds to zones without

macro fractures. Hence, only the equivalent elastic compliance tensor M is input into the zones.

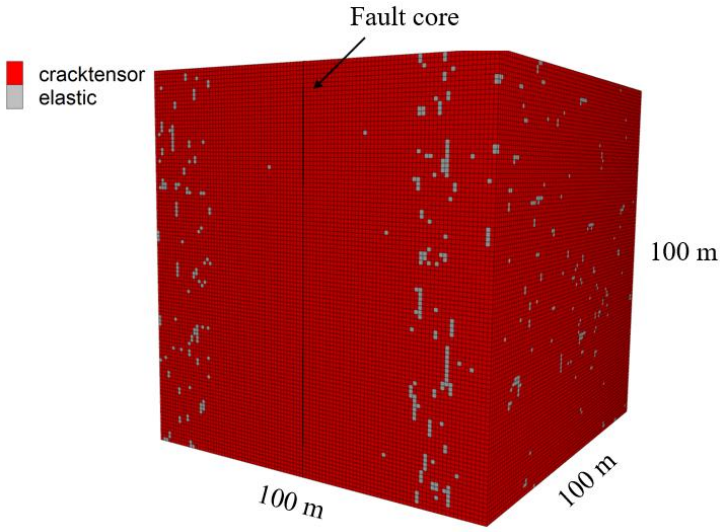

Fig. 5.4: Numerical model showing zones with anisotropic or isotropic compliance tensor.

5.5 Model input parameters

The host rock within the fault damage zone is assumed to be composed of granite. Two assumptions are adopted: (1) the elastic modulus of intact granite rock ranges from 60 to 70 GPa (Sosna. 2011; Behzadafshar et al., 2019); and (2) the GSI of the fractured rock mass, including meso- and micro-discontinuities ranges from 60 to 70 (Sainoki et al., 2021). The deformation elastic modulus of the rock mass with meso- and micro-discontinuities can be estimated using the equation proposed by Hoek and Brown (1997):

$$E_d = \sqrt{\frac{\sigma_{ci}}{100}} 10^{\left(\frac{GSI-10}{40}\right)} \tag{4.8}$$

where E_d and σ_{ci} represent the deformation elastic modulus of the rock mass and the uniaxial compressive strength of intact rock, respectively. Based on the assumed parameters, the elastic modulus of the rock mass is estimated to be 40 GPa. The Poisson's ratio of granite rock mass is assumed to be 0.2, within the typical range of 0.17 to 0.30 (Li et al., 1999). Additionally, a density of 2600kg/m^3 is applied to the model.

The normal-to-shear stiffness ratio is typically measured and/or assumed to be greater than 1.0 (Matsuki et al., 2009). For more details, the determination of shear stiffness is based on the study by Bandis et al. (1983), assuming a discontinuity with a unit length, as the fracture stiffness

is inversely proportional to the fracture diameter in the crack tensor theory. According to the study conducted by Bandis et al. (1983), the ratio of normal-to-shear stiffness was assumed to be 3. The fracture normal and shear stiffnesses are initially set at 30 GPa/m and 10 GPa/m, respectively. It is worth noting that the assumed fracture stiffnesses fall within a reasonable range based on previous studies (Eftekhari et al., 2014; Konstantinovskaya et al., 2014; Shu et al., 2019). Moreover, the values of fracture stiffnesses are varied in the model since the present study aims to investigate the effect of fracture stiffness on seismic source parameters.

For the fault core, the normal and shear stiffnesses are set at 1.0 GPa/m and 0.3 GPa/m, respectively, maintaining the same normal-to-shear stiffness ratio. The difference in stiffness between fractures and the fault core is due to their varying scales. The stiffness of the fault is assumed to fall within a plausible range for simulating the mechanical behaviour of faults in underground mines (Sainoki et al., 2014). The friction angle of the fault is assumed to be 30°, a value considered reasonable based on previous studies (Barton. 1976; Sainoki et al., 2019), and the cohesion is set at 0 Pa (Barton et al., 1974). In FLAC3D, fault core is represented by interface elements composed of triangular zones defined by three nodes. At each node, normal and shear springs are assigned, and the corresponding stresses are computed from the relative displacements of the nodes multiplied by the stiffness values. The Coulomb's shear strength model with a slip-weakening law is then employed. During dynamic analysis, the stress state along the fault core is monitored at each calculation step. Once the shear stress acting on the fault exceeds the shear strength determined by this model, sliding is initiated, and the friction angle is instantaneously reduced from 30° to 20°. This approach has been validated in previous studies as a feasible method to producing realistic dynamic behaviour of the fault (Sainoki et al., 2020). In this study, the slip-weakening distance (D_c) is assumed to be zero, which is reasonable because Eq. (2.7) indicates that D_c is sufficiently small for seismic events of this magnitude. Moreover, the validity of this assumption is supported by the consistency between the scaled energy obtained from the present simulations and the values reported in previous studies (Jost et al. 1998; Mayeda et al. 2005; Yamada et al. 2007), as further discussed in Section 4.8.1. It is to be noted that variations of these parameters qualitatively have no influence on the primary purpose of this study, i.e., investigation on the effect of fracture stiffness in the fault damage zone on the intensity of induced seismicity on the fault core. All properties of the fault damage zone are listed in Table 1.1, and it is considered the base case in this study.

Table 5.1: Damage zone mechanical properties.

	Near-fault fracture density (α)	Dip (°)	Dip Direction (°)	Depth (m)	Fracture normal stiffness (GPa/m)	Fracture shear stiffness (GPa/m)	Fault normal stiffness (GPa/m)	Fault Shear stiffness (GPa/m)
Damage zone	30	90	90	2000	30	10	1	0.3

5.6 Fault damage zone cases

Since the characteristics of fractures are governed by the lithology and structures, various fracture densities and directions exist within different fault damage zones (Gudmundsson et al., 2010; Eckert et al., 2014; Ju et al., 2014). Furthermore, the increasing demand for coal and other mineral resources has led to a gradual increase in mining depth. For example, in South Africa, there are many mines with depths exceeding 3000 m (Durrheim. 2010). Hence, it is necessary to investigate the effectiveness of increased fracture stiffness on seismic source parameters under different fault damage zone cases with various stress states.

All the cases presented in this study are listed in Table 4.2. As the base case, its parameters are shown in Table 4.1. In this study, the fracture normal and shear stiffnesses, represented by K_{n} and K_{s} in Eq. (4.6), are modified, after simulating the initial stress state for each case, by increasing their respective values to examine the effect of fault damage zone stiffness on the intensity of induced seismicity. In the case where the initial fracture normal and shear stiffnesses are 10 GPa/m and 3 GPa/m, respectively, all other parameters are the same as those in the base case, except for the initial fracture stiffnesses. When the initial fault normal and shear stiffnesses are 3 GPa/m and 1 GPa/m, respectively, all other parameters are the same as those in the base case, except for the initial fault stiffnesses. Additionally, the distance in Table 4.2 implies the location from the fault core to the fracture where the stiffness increases. As can be seen in Fig. 4.5, the distance is set to 0 m, 10m, and 30 m in this study. The black thick lines in Fig. 4.5 represent the fracture with increased stiffness and a width of 10 m. The distances were selected as part of a parametric study due to the fact that causative faults and/or shear zones are often located near

active mining areas (Sainoki et al., 2017; Cheng et al., 2019), with the aim of investigating which region's stiffness enhancement has a greater effect on controlling the intensity of seismic events. Similarly, the fracture density coefficient α was set to 5, 10, 15, and 30. These values fall within a reasonable range of the fracture density in fault damage zones (Johri. 2012; Yue et al., 2022) and are intended to examine how the effectiveness of stiffness enhancement depends on the fracture density in supressing the intensity of seismic events. The effect of fracture stiffness enhancement on seismic source parameters under different cases is quantitatively analysed in Section 4.8.

Table 5.2: Various cases of the fault damage zone.

	Near-fault fracture density (α)	Dip (°)	Dip Direction (°)	Depth (m)	Distance (m)	Initial fracture stiffness (GPa/m)	Initial fracture stiffness (GPa/m)	Initial fault stiffness (GPa/m)
Parameters	5 10 15 30	45 60 90	45 60 90	1000 2000 3000 4000	0 10 30	K_n=10 K_s=3	K_n=30 K_s=10	K_n=3 K_s=1

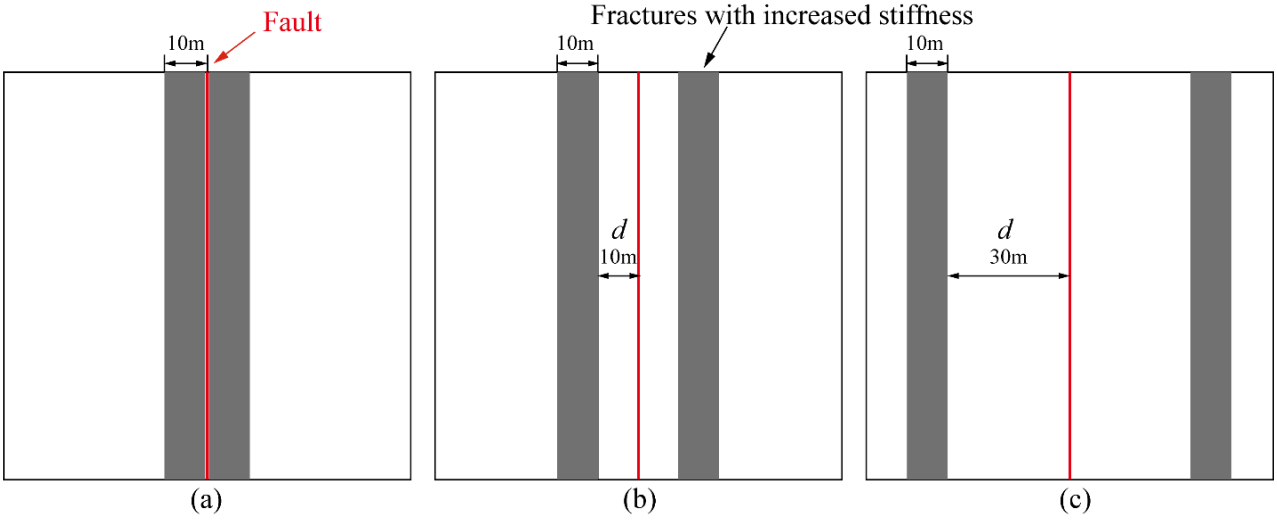

Fig. 5.5: Distance from the fault core.

5.7 Numerical analysis

5.7.1 Analysis procedure

The analysis procedure is depicted in Fig. 4.6. The initial stress state is simulated by applying regional stresses to the external boundaries in a static condition. The direction of gravity is rotated at 20° in anticlockwise direction to represent a fault dipping at 70° due to a complex procedure to generate a DFN model for dipping faults. Due to regional stress rotation, the magnitude of the stress on the left boundary differs from that on the right boundary (Fig. 4.7a). The stresses applied to the model correspond to conditions at the depths shown in Table 4.2, and a horizontal-to-vertical stress ratio is set at 0.7 to simulate a normal fault. The displacement in all the directions is fixed at the four vertices to prevent the rigid body movement due to unbalanced force. Furthermore, the displacement on the bottom boundary is constrained only in the *z*-direction (Fig. 4.7b). The initial anisotropic stress state is shown in Fig. 4.8.

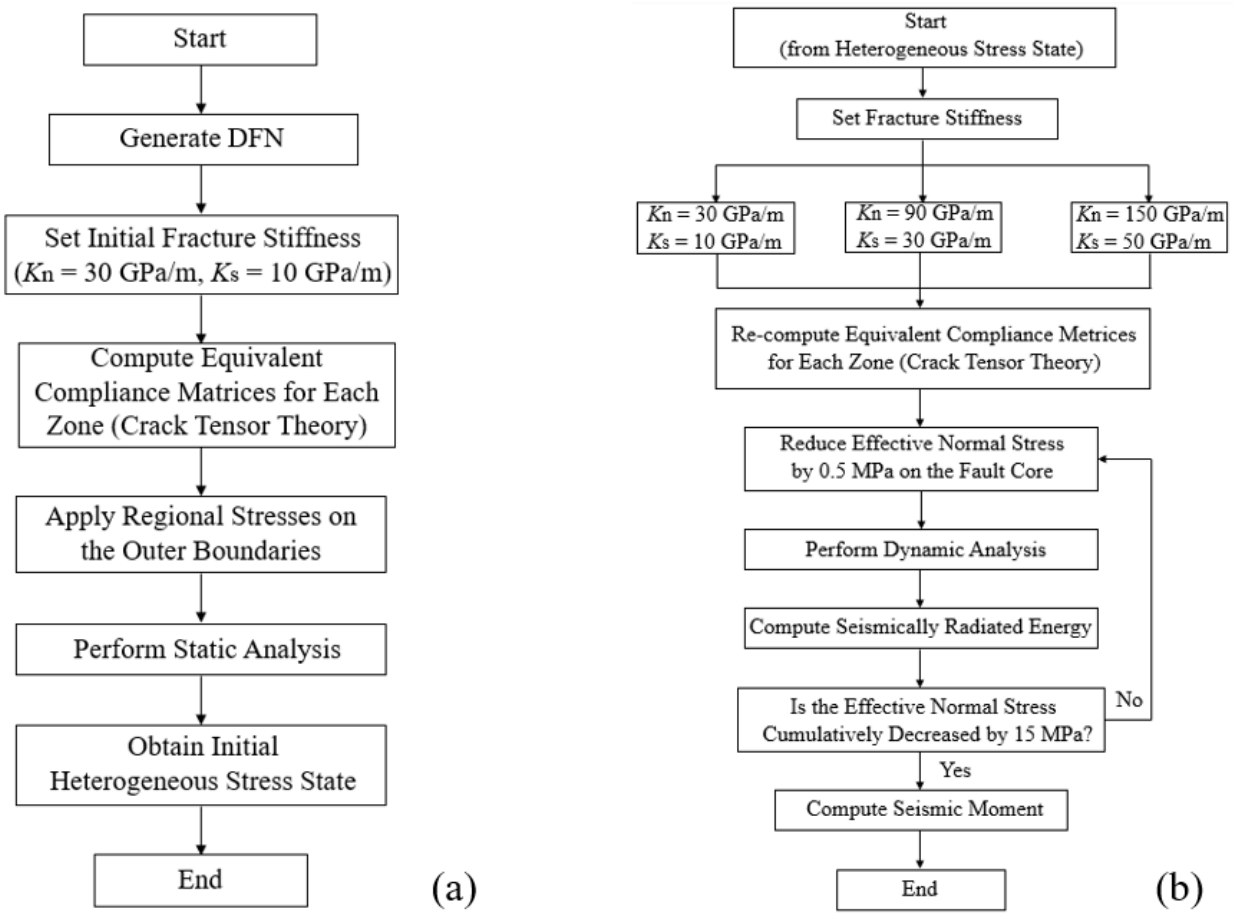

Fig. 5.6: Analysis procedure.

After simulating the initial stress state to establish a baseline condition, fracture normal and shear stiffnesses are increased by adjusting K_n and K_s in Eq. (4.6) to reflect changes in the fault damage zone. Then, a dynamic analysis is carried out to simulate induced seismicity on the fault core, assessing the influence of increased stiffness on the seismic source parameters. Sainoki et al. (2023) developed a method to simulate spatially distributed on-fault seismicity under a heterogeneous stress state within the fault damage zone. Based on their method, the effective normal stress on the fault is reduced incrementally within a circular region to induce seismic events (Fig. 4.7c). In the simulation, the effective normal stress is decreased by 0.5 MPa in each analysis stage, with a total reduction of 15 MPa over 30 stages. The total stress at the fault center is approximately 35 MPa, corresponding to a depth of 1950 m. The reduction in effective normal stress is implemented by increasing the pore water pressure within the circular zone (Fig. 4.7c). The total normal stress (σ_n) acting on the fault satisfies the following relation (Terzaghi 1943):

$$\sigma_n = \sigma_n^{'} + P \tag{4.9}$$

where $\sigma_n^{'}$ and P represent the effective normal stress and the pore water pressure, respectively. Since the applied boundary stresses remain unchanged, the total normal stress (σ_n) is constant. Accordingly, an increase in the pore water pressure results in a decrease in $\sigma_n^{'}$, which effectively weakens the fault core and facilitates slip initiation. Considering the initial pore pressure distribution in the model that varies with the depth, the reduction of the effective normal stress is large enough to cause seismic events and almost no seismic events occur with the further decrease in the effective normal stress (Sainoki et al., 2023). The method assumes that on-fault induced seismicity is triggered by fault unclamping, which involves a reduction in effective normal stress due to human activities such as mining and fluid injection. Additionally, it is to be noted that when changing the magnitude of the effective normal stress reduction in each analysis stage, source parameters of induced seismicity simulated are varied as well. However, as this study focuses on the effect of the mechanical properties of the fault damage zone, the effective stress reduction magnitude is not a key factor considering the purpose of the study.

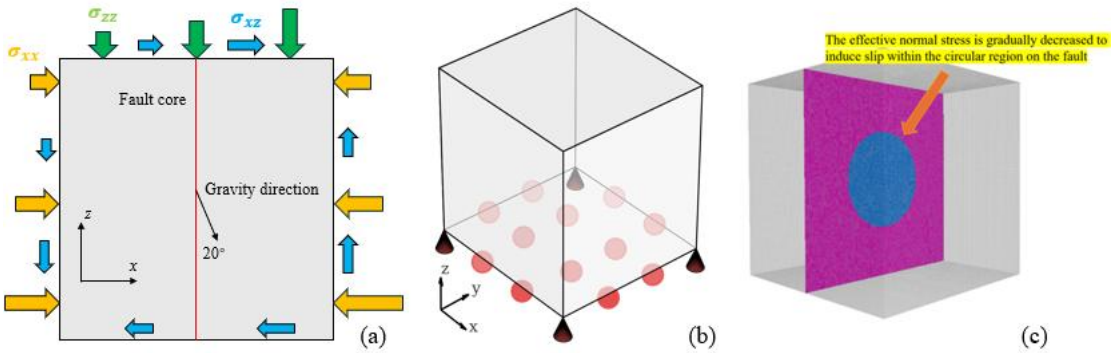

Fig. 5.7: (a) Stresses applied to the model boundaries (cross-sectional view), (b) displacement constraint conditions, (c) and effective normal stress reduction to induce seismic events on the fault

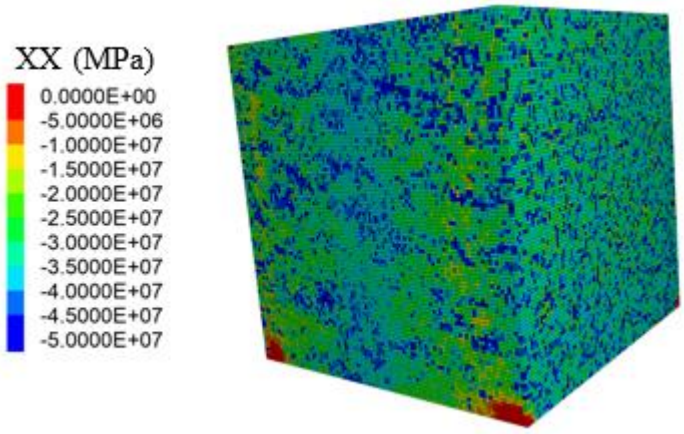

Fig. 5.8: Initial stress state of the model.

5.7.2 Calculation of seismic source parameters

The purpose of the present study is to investigate the effect of fracture stiffness within the fault damage zone on seismic source parameters of seismic events, namely seismically radiated energy, seismic moment, maximum shear displacement, and peak particle velocity. These seismic source parameters are crucial for estimating the damage caused by the fault-slip (Sainoki and Mitri. 2015). Then, a parametrical study is performed with respect to K_n and K_s in Eq. (4.6).

Seismically radiated energy is calculated based on a formula proposed by Luis and Hiroo (2005). They assumed that the seismically radiated energy is the work done by stress perturbations across a closed surface S_0 embedded in the medium, surrounding the epicenter at a far distance as follows (Fig. 4.9):

$$E_R = -\int_{t_0}^{t_1} dt \int_0^{S_0} \left(\sigma_{ij} - \sigma_{ij}^0\right) u_i n_j dS \tag{4.10}$$

where σ_{ij}^0 and σ_{ij} represent the initial stress and the stress at any time, respectively; u_i is the particle velocity; n_j is the unit vector normal to S_0 pointing outwards. t_0 denotes a reference time before the earthquake and t_1 represents a time after the earthquake when any movement has stopped within S_0. In this study, the closed surface is set to be 25 meters from the epicenter.

The moment tensor *M* of a seismic source in an anisotropic medium is calculated as follows (Aki et al. 2002):

$$M_{ij} = Y_{ijkl} D_{kl} \tag{4.11}$$

where Y_{ijkl} are the elastic parameters of the anisotropic medium surrounding the fault; *D* represents the symmetric dyadic tensor. Eq. (4.11) can equably be expressed in matrix form as (Vavryčuk et al. 2005):

$$m = Y \cdot d \tag{4.12}$$

where *Y* is the 6 × 6 matrix of the elastic parameters of rock mass surrounding the fault; *m* and *d* are the 6-vectors defined as:

$$m = \left(M_{11}, M_{22}, M_{33}, M_{23}, M_{13}, M_{12}\right)^T \tag{4.13}$$

$$d = u_s S \left(n_1 v_1, n_2 v_2, n_3 v_3, n_2 v_3 + n_3 v_2, n_1 v_3 + n_3 v_1, n_1 v_2 + n_2 v_1\right)^T \tag{4.14}$$

where u_s is the slip; *S* is the fault area; *n* and *v* denote the fault normal and slip direction, respectively. Then, the value of seismic moment *M* in an anisotropic medium can be calculated as:

$$M = \frac{1}{\sqrt{2}} \sqrt{\sum_i \sum_j M_{ij}^2} \tag{4.15}$$

In the present study, seismically radiated energy and seismic moment are the sum of 30 analysis stages. Peak particle velocity (PPV) can be considered a damage threshold for rock masses subjected to seismic waves (Brinkman. 1987) and serves as an important indicator for evaluating the induced seismicity in the dynamic analysis (Sainoki and Mitri. 2014; 2016). In the present study, the peak particle velocity is calculated as the average maximum velocity at the grid points in the vicinity of the fault core. Furthermore, since the shear displacement increases during a

seismic process, the maximum shear displacement is defined as the value at the final analysis stage (30th stage) in the simulation.

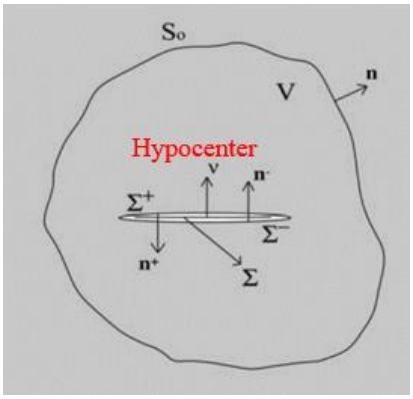

Fig. 5.9: Schematic diagram of energy during earthquake.

5.8 Simulation results

5.8.1 Effect of fracture stiffness for each case and its verification

The effect of fracture stiffness on seismic source parameters under the base case is shown in Fig. 4.10, with the parameters normalized relative to their respective values. It is found that fracture stiffness affects all the parameters significantly. To be more precise, when fracture stiffness is increased by five times, seismically radiated energy, seismic moment, peak particle velocity, and maximum shear displacement are decreased to 39.7%, 30.9%, 44.1%, and 40.8%, respectively. Fig. 4.11a depicts the peak particle velocity near the fault at 30th stage. As shown in the figure, peak particle velocity is significantly reduced as fracture stiffness increases, indicating that slip rate also decreases since peak particle velocity is a function of slip rate. Fig. 4.12a shows the shear displacement increment on the fault at 30th stage. Shear failure occurs in the circular area where the effective normal stress decreases. It is found from the figure that fault-slip area is significantly limited with increasing fracture stiffness. When the fracture stiffness is increased by a factor of five, the shear displacement becomes very small (about 2 mm from the base case of approximately 6.5 mm). These results indicate that increasing fracture stiffness can effectively control the intensity and magnitude of induced seismicity using the base case parameters.

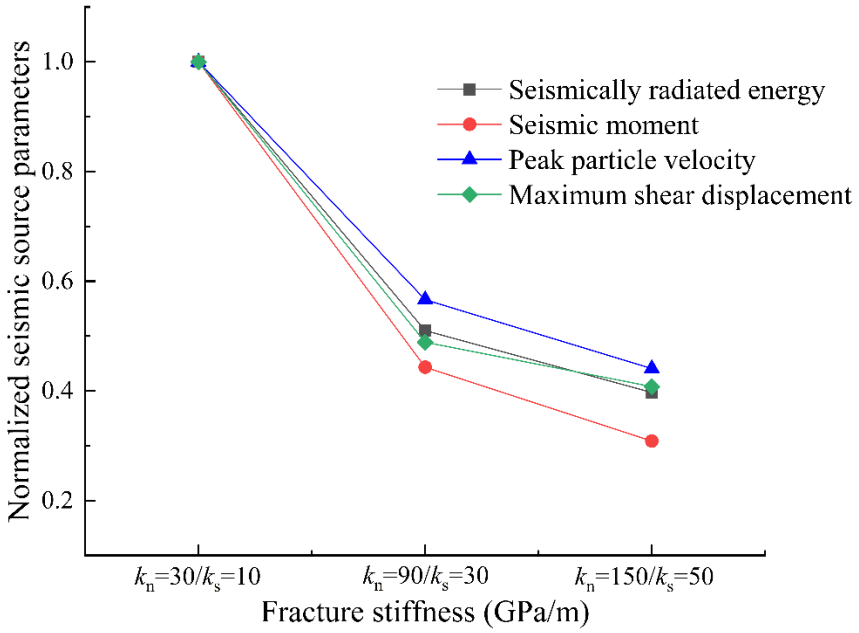

Fig. 5.10: Normalized seismic source parameters change under base case.

The validity of the numerical model has been examined in terms of the scaled energy, defined as the ratio of seismically radiated energy to seismic moment. According to previous studies on natural and induced seismicity (Jost et al. 1998; Mayeda et al. 2005; Yamada et al. 2007), the scaled energy typically ranges from 1.0×10^{-7} to 1.0×10^{-4}. The scaled energy computed from the seismic events simulated in this study is 1.5×10^{-5}, which falls within this range. Hence, the consistency of the scale energy indicates that the dynamic simulation conducted in the present study can yield reasonable seismic energy, i.e., slip rate, considering its magnitude and can reproduce the dynamic failure of the fault to a certain degree. Although the interface element and continuum-based approach employed in the present study may not fully reproduce large-scale fault slips accompanied by substantial deformation, it is suitable for simulating induced seismic events with dimensions of less than several tens of meters.

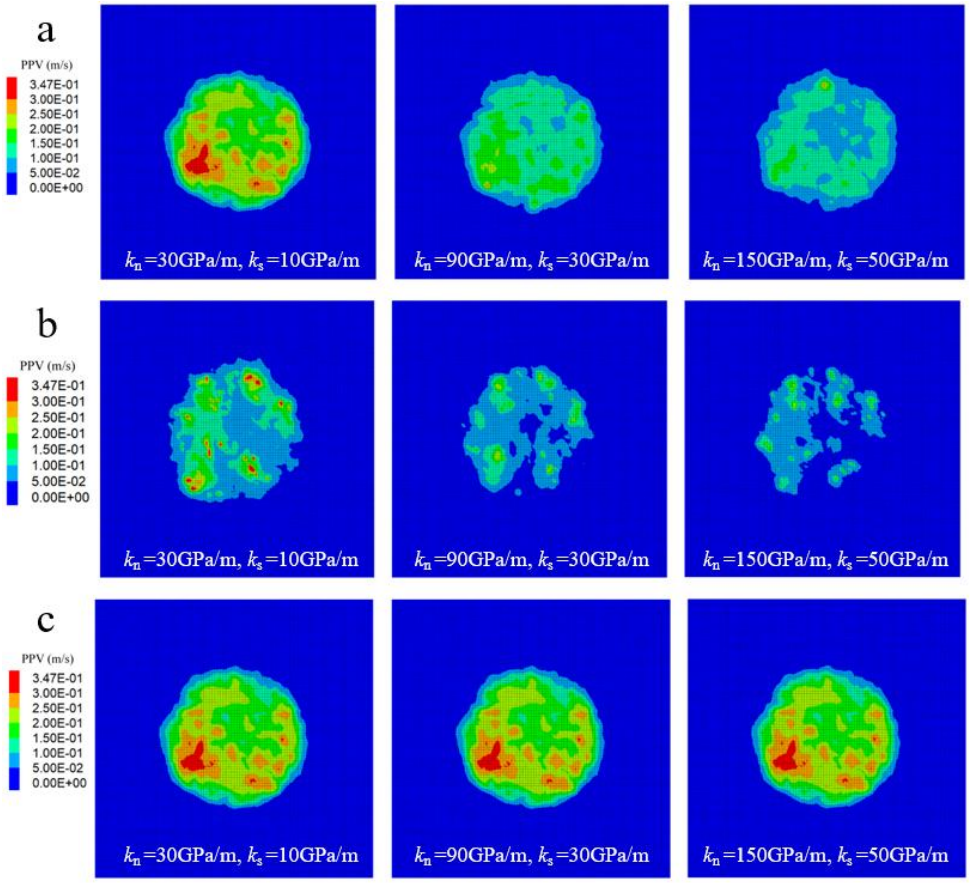

Fig. 5.11: Near-fault peak particle velocity for (a) base case, (b) near-fault fracture density coefficient of 5, and (c) distance of 30 m.

While the reduction in seismic source parameters with increasing fracture stiffness has been demonstrated, these observations alone may not provide a sufficiently intuitive understanding of the underlying mechanics. To address this limitation, the shear stiffness of the damage zone was quantified under different fracture stiffness conditions. As shown in Fig. 4.13, both seismically radiated energy and seismic moment exhibit a clear monotonic decrease with increasing damage zone shear stiffness. Specifically, when the fracture stiffness increases by a factor of 5, the damage zone stiffness increases by approximately 2.05 times, with the seismically radiated energy and seismic moment reduced to approximately 39.7% and 30.9% of their original values, respectively. This trend indicates that the increase in fracture stiffness enhances the apparent shear stiffness of the damage zone, thereby restricting slip development and reducing the energy available for release during rupture. The reduction in seismic source parameters exhibits a nonlinear trend, with the

decreasing rate becoming smaller at higher damage zone stiffness. This suggests a diminishing sensitivity of energy release to stiffness once a certain threshold is exceeded. Fig. 4.14 illustrates the spatial distribution of E_{11}, the first component of the 6×6 equivalent elastic matrix calculated using crack tensor theory, under various fracture stiffness conditions. In all cases, E_{11} is markedly lower near the fault core due to the high fracture density. With increasing fracture stiffness, the E_{11} values increase significantly, indicating a progressive enhancement of the damage zone stiffness. In more detail, when the fracture stiffness increases fivefold, E_{11} at a zone near the fault core (ID: 265049) rises from 5.7×10^{8} Pa to 2.7×10^{9} Pa, corresponding to a 4.7-fold increase, whereas a zone at the model boundary (ID: 30005) increases from 1.05×10^{10} Pa to 2.7×10^{10} Pa, a 2.6-fold increase. Although E_{11} does not directly represent the shear stiffness directly, it represents the directional stiffness of the zone, and its increase indicates the relative stiffness enhancement of the damage zone. These results further confirm the increase in damage zone shear stiffness with rising fracture stiffness, as shown in Fig. 4.13.

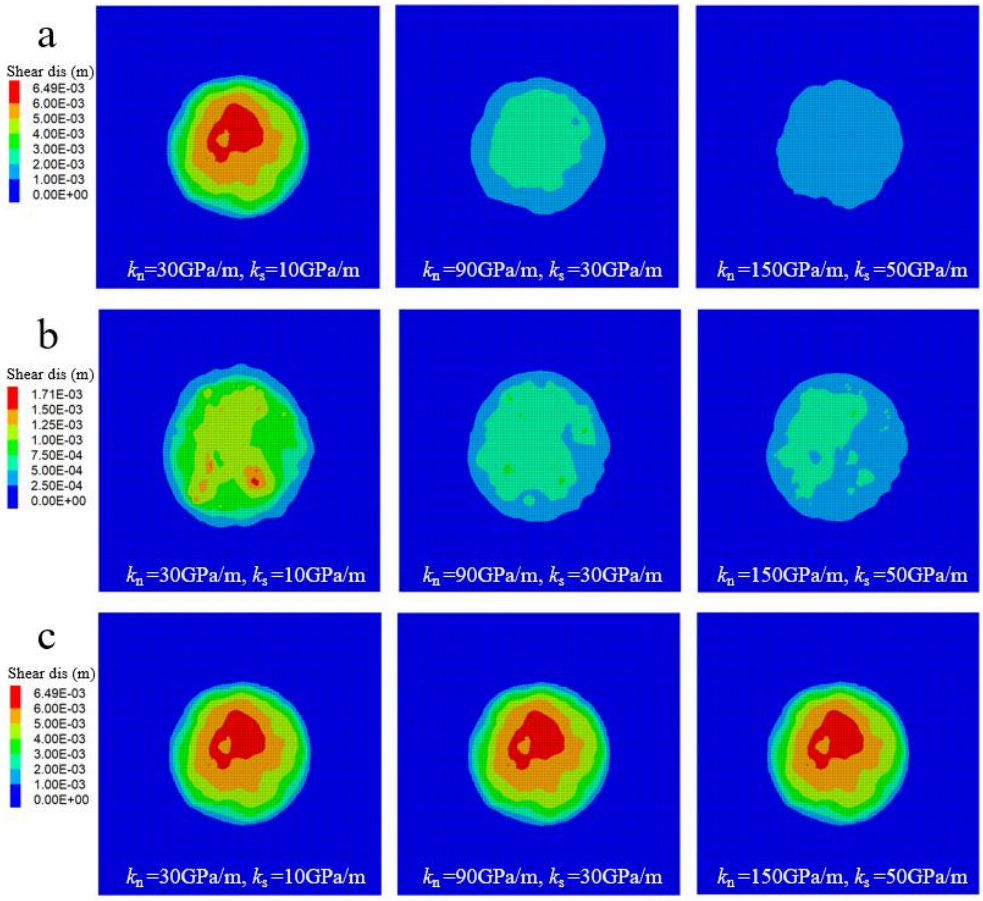

Fig. 5.12: Shear displacement increment on the fault for (a) base case, (b) near-fault fracture

density coefficient of 5, and (c) distance of 30 m.

These numerical results are consistent with the theoretical verification based on the slip-weakening model in chapter 2, which demonstrates that increased stiffness of the surrounding rock mass suppresses fault slip and consequently reduces the amount of seismically radiated energy. More specifically, as shown in the base case, the seismically radiated energy is decreased to approximately 44.4 % when the shear stiffness is doubled for a D_c of 1 mm. For the numerical model, when the apparent shear stiffness of the damage zone is doubled, the seismically radiated energy is decreased to 39.7%. As the fracture density is higher near the fault core than the outer region, it is thus deduced that the apparent shear stiffness increase is more significant near the fault core where seismic events take place. Specifically, as shown in Fig. 4.14, when the fracture stiffness increases fivefold, E_{11} near the fault core increases by 4.7-fold, whereas E_{11} at the model boundary increases by only 2.6-fold. This highlights that the stiffness enhancement is much more pronounced in the vicinity of the fault core. Hence, it is reasonable that the seismically radiated energy is more effectively reduced in the numerical model than the theoretical one, although the effectiveness of this method attenuates with the decrease in D_c. As shown in previous studies (Ohnaka, 2000; Sainoki et al., 2020), D_c scales with the magnitude of seismic events, implying that the effectiveness of increasing fracture stiffness is more pronounced for induced seismic events with larger magnitudes.

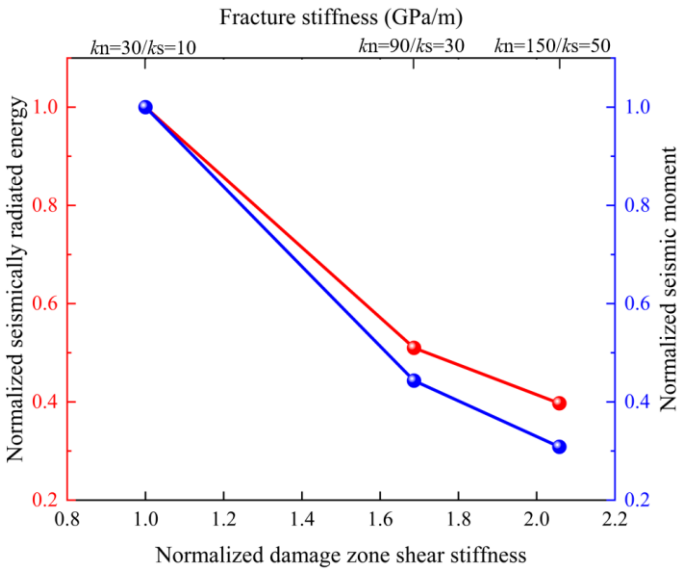

Fig. 5.13: Effect of damage zone stiffness on seismic source parameters.

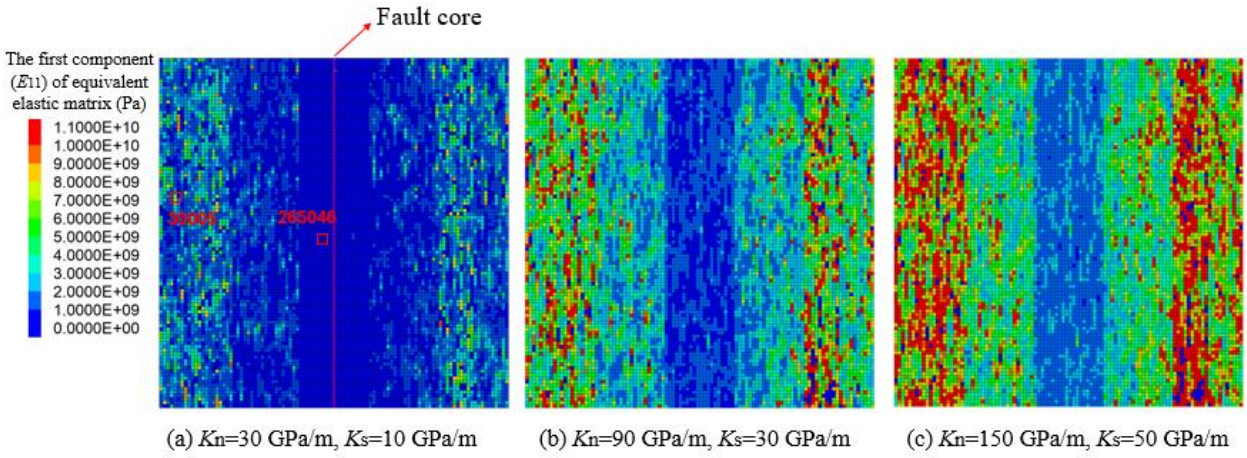

Fig. 5.14: Spatial distribution of the first component (E_{11}) of the equivalent elastic matrix calculated using crack tensor theory under various fracture stiffness conditions.

5.8.2 Results of model parametric study

Fig. 4.15 illustrates the normalized seismic source parameters under various cases described in section 4.6, with fracture stiffness increasing by a factor of five. Pattern 1 in the figure represents the case with initial fracture normal and shear stiffness of 10 GPa/m and 3 GPa/m, respectively, as described in section 4.6. Pattern 2 corresponds to the base case, while Pattern 3 represents the case with initial fault normal and shear stiffness of 3 GPa/m and 1 GPa/m, respectively. It can be noticed that in most cases, an increase in fracture stiffness has a significant and similar effect on the seismic source parameters. For example, at different depths, when the fracture stiffness is increased by a factor of five, the seismically radiated energy is reduced to 36.7%, 39.7%, 41.0%, and 35.8%, respectively. The increase in fracture stiffness has a significant and quite similar effect on seismic source parameters under different depths. However, in the cases where the distance is 10 m and 30 m, the seismic parameters remain almost constant, indicating that the effect of increased fracture stiffness is minimal under these cases. Additionally, it is found that the values of seismic source parameters decrease as the fracture density coefficient increases. This suggests that a higher fracture density in a fault damage zone results in a greater effect of increased fracture stiffness on seismic source parameters. The results for the cases of density and distance are slightly different from those of the other cases; therefore, both need to be analyzed in more detail.

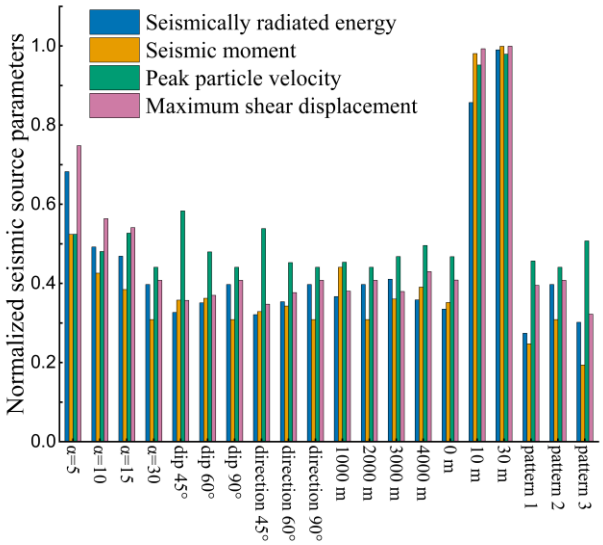

Fig. 5.15: Normalized seismic source parameters under various conditions.

5.8.3 Effect of fracture stiffness using different near-fault fracture densities

Fig. 4.16 illustrates the normalized seismic source parameters under near-fault fracture density coefficients of 5 and 30, respectively. Near-fault fracture density is varied by adjusting the parameter α in Eq. (4.1). Interestingly, there are clear differences in the effect of fracture stiffness on the seismic source parameters between the two cases of near-fault density coefficient. It is found from Fig. 4.16a that seismic moment and peak particle velocity are decreased to about 52.3% with the increase of fracture stiffness, while seismically radiated energy and maximum shear displacement are reduced to 68.2% and 74.8%, respectively. On the other hand, seismic source parameters are decreased to between 30% and 40% when near-fault fracture density coefficient is 30 (Fig. 4.16b). Fracture stiffness appears to have a more significant effect on the seismic source parameters when the near-fault fracture density is higher.

Fig. 4.11b depicts the near-fault peak particle velocity when density coefficient a is 5. It can be found from the figure that peak particle velocity decreases significantly with increasing fracture stiffness, leading to moderate ground motion in the vicinity of the fault. Fig. 4.12b shows the shear displacement increment on the fault when near-fault fracture density coefficient a is 5. As can be seen, the area undergoing shear failure decreases with the increase in fracture stiffness. Fault-slip takes place on almost the entire circular region when fracture normal and shear stiffnesses are 30 GPa/m and 10 GPa/m, respectively. When fracture stiffness is increased by 5 times, there seem to

be fewer slip patches. These results indicate that even though the effect of fracture stiffness decreases with the reduction in near-fault fracture density, fracture stiffness remains effective under low fracture density cases.

These findings motivate a further investigation into how fracture stiffness influences the overall stiffness of the damage zone under different fracture density conditions. To this end, Fig. 4.17a presents the relationship between normalized fracture stiffness and damage zone shear stiffness for various values of the density coefficient α. Although damage zone stiffness increases with fracture stiffness in all cases, the increase is more pronounced for higher fracture densities. For example, a fivefold increase in fracture stiffness leads to a damage zone stiffness increase of approximately 1.4 times under $\alpha = 5$, compared to 2.05 times under $\alpha = 30$. Hence, fracture stiffness becomes more effective at increasing overall damage zone stiffness when the fracture density is higher, further explaining the greater reduction in seismic source parameters observed under such conditions.

In addition to near-fault fracture density, this study further investigated the effect of total fracture surface area to more comprehensively capture the influence of fracture geometry distribution on the stiffness of the damage zone. As shown in Fig. 4.17b, the normalized damage zone shear stiffness increases with normalized fracture surface area, regardless of the stiffness level. This trend highlights that the total fracture surface area, which reflects both the number and the size of fractures, plays a crucial role in controlling the mechanical integrity of the damage zone. Notably, the rate of stiffness increase tends to accelerate as the normalized total fracture surface area grows from 1.9 to 3.4, especially under higher stiffness conditions, suggesting a nonlinear amplification effect. This implies that when fractures are more spatially extensive, the overall structure becomes more sensitive to changes in fracture properties. Therefore, fracture surface area is not only a geometric descriptor but also a key factor in modulating the mechanical behaviour of fractured media, offering a complementary explanation to the density-based interpretation.

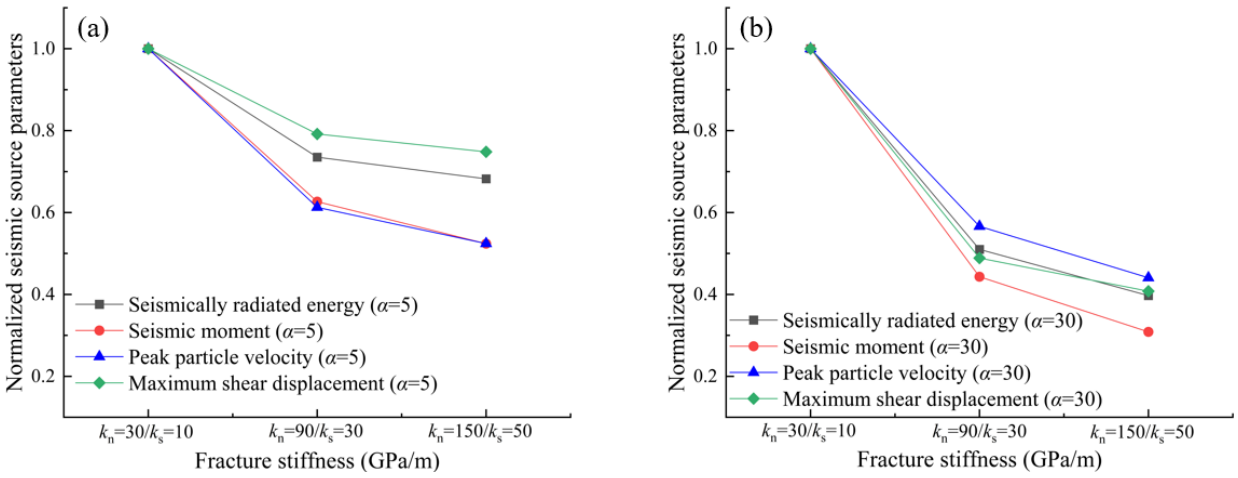

Fig. 5.16: Normalized seismic source parameters using fracture density coefficient of (a) 5, and (b) 30.

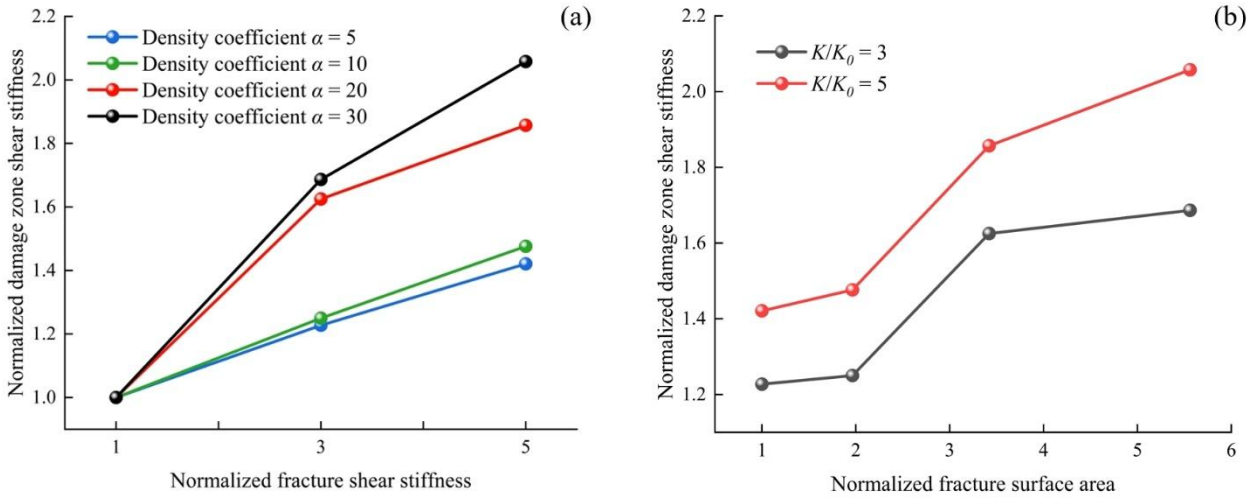

Fig. 5.17: Normalized damage zone stiffness for (a) different near-fault fracture density coefficient, and (b) fracture surface areas.

5.8.4 Effect of fracture stiffness using different distances from the fault

Fig. 4.18 illustrates the effect of fracture stiffness on normalized seismic source parameters under different distances from the fault as depicted in Fig. 4.5. Notably, there are clear differences in the effect of fracture stiffness on the seismic source parameters between the two distances from the fault. It seems that a close distance from the fault exerts a considerable influence on all seismic source parameters while a far distance does not. As shown in Fig.4.18a, when the distance is 0 m,

seismically radiated energy, seismic moment, maximum shear displacement, and peak particle velocity are reduced to 33.5%, 35.2%, 46.7%, and 40.8%, respectively. All seismic source parameters are down to less than 50%. Conversely, when the distance increases to 30 m, all seismic source parameters remain almost the same despite the increase in fracture stiffness (Fig. 4.18b). Fig. 4.11c illustrates the near-fault peak particle velocity when the distance is 30 m. It can be found from the figure that peak particle velocity shows no change with increasing fracture stiffness, indicating that the slip on the fault is constant. Fig. 4.12c depicts shear displacement increment on the fault when the distance is 30 m. As can be seen, shear displacement increment also remains unchanged with increasing fracture stiffness since it is induced by the slip on the fault. These results suggest that fracture stiffness has a much greater effect on the seismic source parameters when fractures with increased stiffness are close the fault. However, the effect of fracture stiffness decreases dramatically as the distance increases. Hence, increasing the stiffness of near-fault fractures is a better approach for controlling the intensity of induced seismicity.

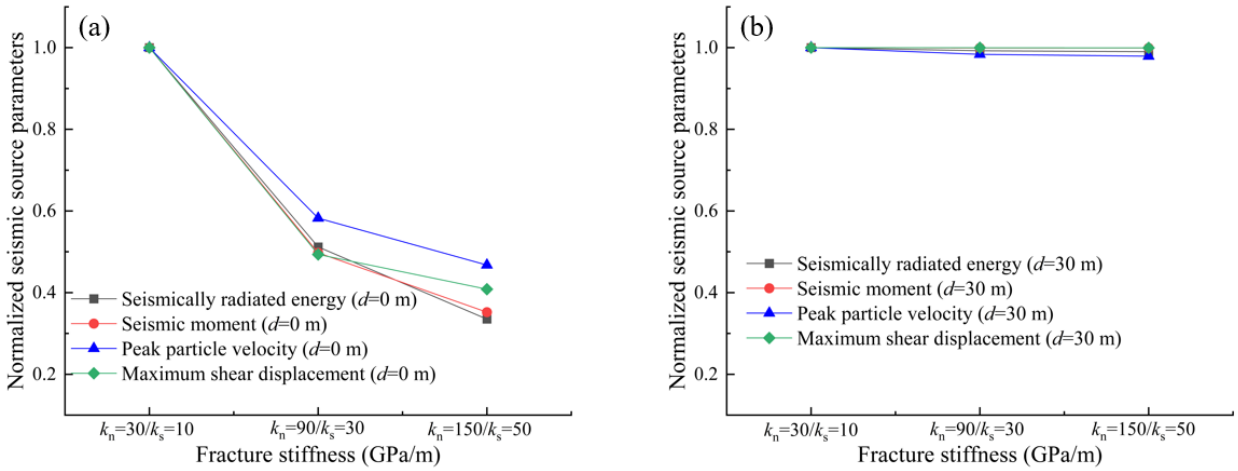

Fig. 5.18: Normalized seismic source parameters using increased fracture stiffness that are (a) 0 m, and (b) 30 m from the fault core.

5.8.5 Effect of fracture stiffness using different thicknesses of enhanced fractures

In this section, the influence of the thickness t of the region with enhanced fracture stiffness on the seismic response is investigated. As illustrated in Fig. 4.19, fractures with increased stiffness are distributed symmetrically around the fault core, and three thicknesses, $t = 10$ m, 40 mand 70 m, are considered. These values are chosen such that $t$is much smaller than, approximately equal to, and greater than the diameter of the fault slip region ($D = 50$ m), respectively. The

normalized seismic source parameters obtained for the different cases are summarized in Fig. 4.20. When $t = 10$ m, increasing the fracture stiffness by a factor of five leads to only modest reductions in the seismic parameters, all of which remain above 80% of their baseline values (Fig. 4.20a). This indicates that, when the stiffened zone is much thinner than the slip region, most of the slip occurs outside the zone of increased stiffness and the mitigation effect is limited.

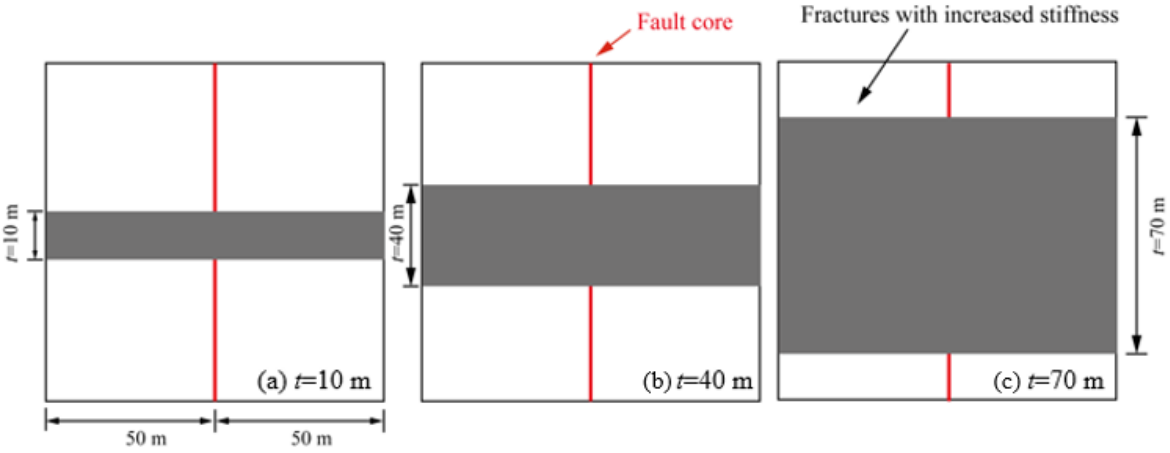

Fig. 5.19: The thickness of the fracture with increased stiffnesses.

A different tendency is observed when t is increased to 40 m. In this case, a fivefold increase in stiffness reduces the seismic moment and maximum shear displacement to 40.9% and 40.2% of their original values, respectively, whereas the reductions in seismically radiated energy and peak particle velocity (PPV) are more modest, remaining at 75.6% and 81.5% (Fig.4.20b). The strong decrease in seismic moment and displacement indicates that slip within the fault slip region is largely suppressed. However, the relatively small changes in energy and PPV can be explained by the fact that the zones used for energy calculation and the PPV observation points are located about 35 m away from the fault core, i.e., outside the region where the fracture stiffness has been increased. As a result, although slip on the fault is effectively reduced, the dynamic response in the surrounding rock mass is not fully controlled.

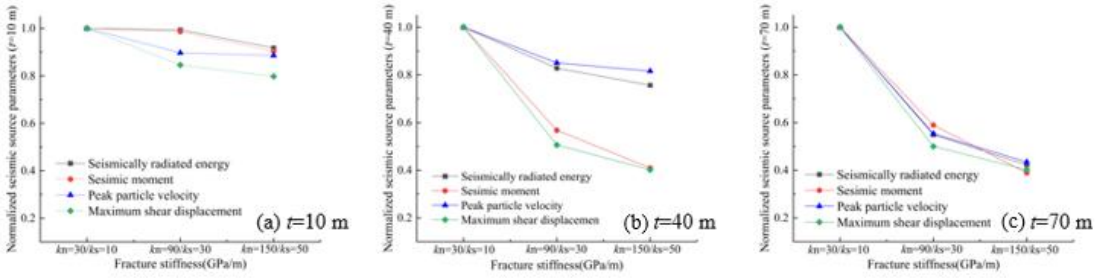

Fig. 5.20: Seismic source parameters under different thicknesses.

When the thickness is further increased to $t = 70$ m, the region of enhanced stiffness fully covers the fault slip region and extends beyond it. Under this configuration, the effect of stiffness enhancement becomes much more pronounced: a fivefold increase in stiffness reduces the radiated energy, seismic moment, maximum shear displacement, and PPV to 42.2%, 38.9%, 40.2% and 43.4% of their respective baseline values (Fig. 4.20c). The PPV distributions in Fig. 4.21 show that, in the case of $t = 10$ m, the overall PPV pattern does not change significantly, although local reductions are visible inside the narrow-stiffened band. For $t = 40$ m, high PPV values are observed mainly outside the region with increased stiffness, reflecting the partial control of wave radiation. In contrast, when $t = 70$ m, the enhanced-stiffness region coincides with and exceeds the slip region, leading to a marked decrease in PPV within and around the fault. These results demonstrate that not only the magnitude of fracture stiffness but also the spatial extent of the stiffened zone relative to the fault slip region critically controls the efficiency of seismic mitigation.

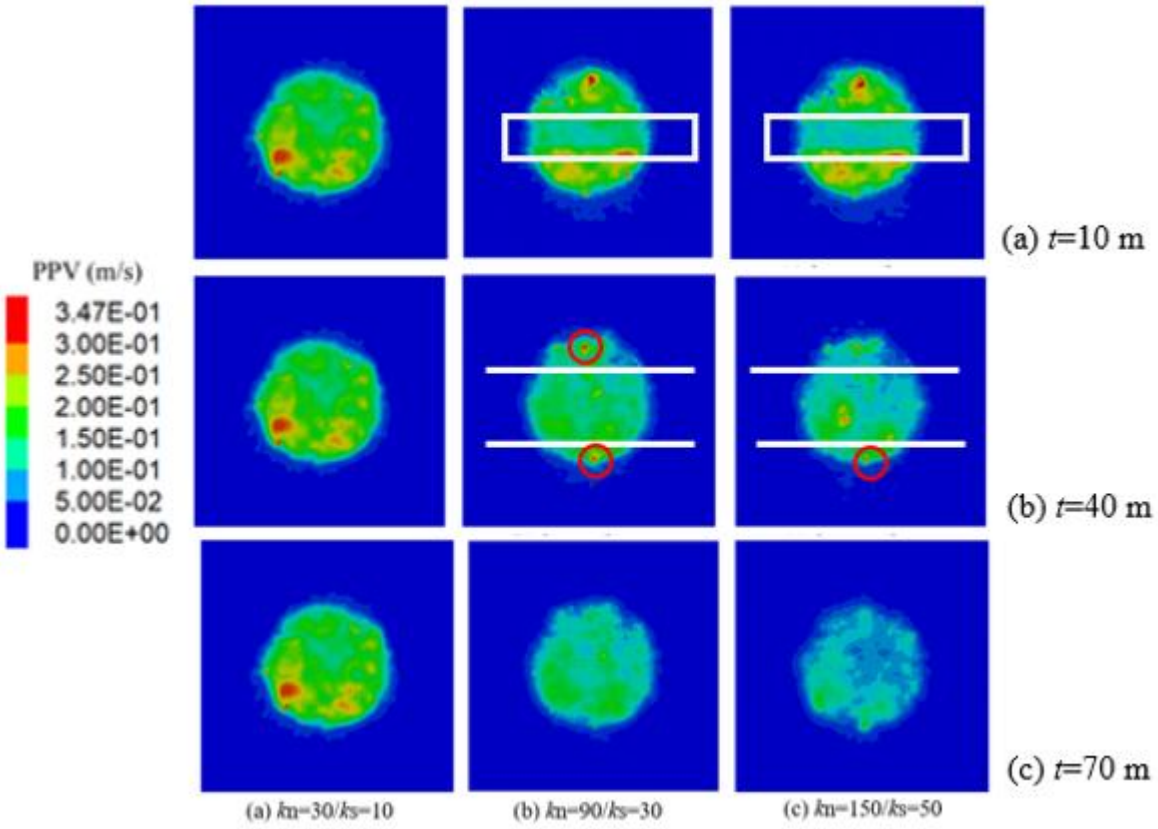

Fig. 5.21: PPV distribution under different thicknesses of the enhanced fracture.

5.9 Discussion

5.9.1 Potential for the proposed method to mitigate the intensity of seismicity

As indicated by seismic monitoring results in deep underground mines (Kozłowska et al., 2016; Urban et al., 2016; Beer et al., 2017; Ma et al., 2018; Wang et al., 2019), it is not uncommon that large seismic events take place away from regions with relatively large stress changes caused by anthropogenic activities, compared to the ambient stress state. In such a case, it is significantly challenging to predict the location and magnitude of such seismic events, as demonstrated by Sainoki et al. (2016). Hence, the effectiveness of conventional methods is limited (Dvorsky et al., 2005; Liu et al., 2019; Kang et al., 2023; Zou et al., 2024), while the proposed method allows us to control the magnitude of seismic events that could occur on an extensive region of the fault core surrounded by a fault damage zone where the stiffness of fractures is increased. This implies that the proposed method can cope with the uncertainty of inherent stress heterogeneity difficult to be predicted. As an example of its implementation, a fractured rock mass near a fault core can be pre-conditioned with grouting techniques prior to the initiation of mining activities, i.e., before the mining activity causes stress re-distribution and unclamps the fault. It is to be noted that, at any rate, the subject of ground improvement is beyond the scope of the current study.

Moreover, our method can be supported by the findings of Sainoki et al. (2015, 2020) who demonstrated that increasing the slip-weakening distance effectively reduces seismically radiated energy and promotes aseismic slip, although their model did not explicitly include the damage zone. From a mechanical perspective, this effect is equivalent to increasing the stiffness of fractures in the surrounding damage zone, which is consistent with the present results. As shown in Fig. 4.11, PPV is significantly decreased in an extensive region near the fault. A fivefold increase in fracture stiffness reduces the PPV from 0.34 m/s to 0.15 m/s, resulting in a low hazard level (Mutke et al., 2015). Furthermore, as indicated by McGarr (1984) and Kaiser et al. (1996), when the magnitude of seismic events exceeds 4.5, PPV could be larger than 1.0 m/s, which is large enough to inflict severe damage to the surrounding rock mass. However, if the PPV can be decreased by more than 50%, the damage could be significantly mitigated, considering the threshold of PPV affecting the stability of rock mass.

In terms of the feasibility of the proposed method, this method could reduce the magnitude of seismicity, irrespective of the initial stiffness of fractures in a fault damage zone. Importantly, although, in the base case, the normal stiffness of fracture from 30 GPa/m to 150 GPa/m to

demonstrate the effect of fracture stiffness on the seismic source parameters, this does not indicate the necessity of increasing the normal stiffness by 120 GPa/m. Pattern 3 shown in Fig.10, where the initial normal stiffness was set at 3 GPa/m, the similar effect has been confirmed when the stiffness was increased from 3 GPa/m to 15 GPa/m. It is plausible to conceive that the stiffness of fractures in a fault damage zone is generally low, compared to fractures in a rock mass outside of the fault damage zone because of many factors, such as fracture size, fluid flow, shear displacement that occurred during the evolution of the fault, etc (Chester et al., 1986; Gudmundsson et al., 2010). Hence, it would not be challenging to increase the stiffness of such fractures by several times, considering the mechanical properties of grouting materials.

5.9.2 The role of the damage zone strength and stiffness

When slip occurs on the fault core, the shear stress in the adjacent damage zone tends to decrease due to the slip-weakening behaviour of the fault (Bizzarri and Cocco. 2003; Mikumo et al., 2003; Ikari et al., 2013). However, shear stress may increase in the outer part of the slipping area and nearby regions of the damage zone as the stress in the slipping area is transferred and re-distributed (Stein. 1999; King and Cocco. 2000; Freed. 2005). If the strength of these regions is enhanced through grouting techniques, more strain energy might accumulate, leading to subsequent rupture. This indicates that damage zone strength can influence not only the rupture path but also the characteristics of seismic energy release.

However, since the fault core typically exhibits lower strength than the surrounding damage zone, rupture is still likely to initiate within the fault core even after reinforcement of the adjacent regions. On the other hand, if the damage zone is overly strengthened, rupture may shift outward and cause secondary failure in peripheral areas. However, due to the discontinuous nature of fractures in these outer regions, such rupture events are expected to generate smaller seismic magnitudes compared to major slips on the fault core.

It to be noted that the current model considers the role of fracture stiffness, it does not account for changes in fracture strength that typically occur during reinforcement processes such as grouting. Both stiffness and strength may increase simultaneously, and their combined effects could alter rupture behaviour in a more complex manner. Therefore, future studies should incorporate both parameters to better assess their interaction and impact on seismic source characteristics.

Overall, variations in damage zone strength can exert significant control over rupture dynamics. Their influence on both energy accumulation and release mechanisms needs further investigation through detailed modelling and parametric analysis.

5.10 Concluding remarks

In this Chapter, the heterogeneous stress condition was successfully simulated using an equivalent continuum approach. Then, the influence of increased fracture stiffness on seismic source parameters was analyzed under various damage zone cases. The main conclusions are as follows:

1. The monotonic reduction of seismically radiated energy with increasing damage zone shear stiffness is theoretically verified using the slip-weakening model. These results show that enhancing rock stiffness suppresses slip development and limits the energy available for release, providing a theoretical basis for the numerical simulations.

2. Across most cases, the contrast between the base case and the increased-stiffness cases clearly demonstrates the critical role of fracture stiffness. Increasing fracture stiffness leads to a substantial decrease in seismic source parameters, which drop to about 40% of their original values. These results confirm that increasing fracture stiffness is an effective approach for controlling the magnitude and intensity of induced seismicity.

3. When the near-fault fracture density coefficient a is 30, seismic source parameters decrease to approximately 30-40% of their original values. In contrast, at a lower density coefficient a of 5, the reduction is more moderate, with values remaining around 50%-75%. These comparative results indicate that the mitigation effect of increased fracture stiffness is more pronounced in densely fractured regions, where the enhancement of the apparent shear stiffness of the damage zone is about 1.5 times that in sparsely fractured zones.

4. When stiffer fractures are located adjacent to the fault core (distance = 0 m), seismic source parameters decrease to less than 50% of their original values. However, when the distance increases farther from the fault core (distance = 30 m), the parameters remain largely unchanged regardless of stiffness enhancement. This suggests that increasing stiffness in near-fault regions is more effective than in distant damage zones for mitigating seismic intensity.

5. Parametric analysis further reveals that both fracture density and total fracture surface area play key roles in modulating damage-zone stiffness. Damage zone shear stiffness becomes more

significant with higher fracture density or larger fracture surface area. In particular, the damage zone stiffness increases more rapidly when the normalized fracture surface area grows from 1.9 to 3.4. This nonlinear amplification highlights the importance of both fracture density and geometric distribution in modulating the mechanical response of the damage zone.

6. The effectiveness of stiffness enhancement also depends on the thickness t of the stiffened fracture zone relative to the fault slip region. When t is much smaller than the slip-region diameter ($t = 10$ m), seismic parameters remain above 80% of their baseline values, indicating limited mitigation. As t increases and the stiffened zone becomes comparable to or larger than the slip region ($t = 40$, 70 m), seismic moment, shear displacement, seismically radiated energy, and PPV are reduced to about 40% of their original values, with the strongest reductions achieved when the stiffened region fully covers the slip area.

6. Conclusions and recommendations

6.1 Conclusions

In this study, the influence of fracture stiffness within fault damage zones on induced seismicity was systematically investigated using a multiscale framework that integrates theoretical analysis, laboratory experiments, and numerical modeling. The study combined slip-weakening-based theoretical verification, CT-DVC-based experimental characterization of damage zone heterogeneity, and numerical simulations at both the mine-scale and the fracture-scale. Through this integrated approach, the role of near-fault fracture stiffness in controlling fault-slip behavior and seismic source parameters was quantitatively clarified. The main findings of this thesis are summarized as follows.

Chapter 1 outlined the background and significance of induced seismicity associated with underground excavations and subsurface engineering. The limitations of conventional mitigation approaches are reviewed, and the motivation for exploring new mitigation strategies is clarified. The objectives and overall structure of the thesis are then presented.

Chapter 2 theoretically examined the influence of damage zone stiffness on seismically radiated energy using the slip-weakening framework. A parametric analysis was conducted by systematically varying the damage zone stiffness, the slip-weakening distance, and frictional parameters. The results demonstrate that increasing the stiffness of the surrounding damage zone consistently suppresses fault slip and significantly reduces seismically radiated energy. In particular, doubling the normalized damage zone stiffness led to a reduction in radiated energy of more than 50%, while increasing the slip-weakening distance resulted in an energy reduction of up to 60%, regardless of frictional conditions. These findings provide a clear theoretical verification that stiffness enhancement in fault damage zones is an effective mechanism for mitigating induced seismicity.

Chapter 3 experimentally investigated the internal mechanical complexity of fault damage zones using a CT- and DVC-based approach applied to 3D-printed rock-like specimens. The experiments demonstrated that deformation within damage zones is highly heterogeneous and strongly controlled by internal structural features. While specimens containing only a fault core exhibited deformation dominated by a narrow, localized path, whereas specimens with distributed fractures showed broader strain localization and the multiple deformation paths. These

experimental findings clearly indicate that simplified or homogeneous representations are insufficient for describing damage zones and highlight the necessity of explicitly accounting for internal structural complexity when modeling fault damage zones.

Chapter 4 constructed a discrete element model incorporating an explicitly generated discrete fracture network (DFN) to investigate stiffness effects at the fracture scale. The results showed that increasing fracture stiffness led to a clear reduction in induced seismicity at the fracture scale and significantly suppressed fault slip processes, demonstrating that stiffness enhancement directly suppresses fault slip. A parametric comparison further revealed that shear fracture stiffness has a much stronger influence on reducing seismically radiated energy than normal stiffness, indicating that shear stiffness plays a dominant role in suppressing fault slip. These results provide direct mechanical evidence that stiffness enhancement within the damage zone can effectively suppress unstable fault slip and reduce seismic intensity.

Chapter 5 developed an equivalent continuum model using the crack tensor theory to represent a mine-scale fault system under heterogeneous stress conditions, which cannot be explicitly resolved by discrete element models in Chapter 4 due to scale and fracture-density limitations. Parametric simulations showed that enhanced fracture stiffness leads to systematic decreases in seismic source parameters, including seismic moment and seismically radiated energy, etc. In most cases, when the stiffness is increased by a factor of five, these parameters were reduced to approximately 40% of their baseline values, exhibiting trends consistent with those observed in Chapter 4 and confirming the strong mitigating effect of stiffness enhancement. The results further revealed that this mitigation effect is most pronounced when fracture density is high and when stiffened fractures are located close to the fault core. In contrast, stiffness enhancement applied far from the fault core produced little change in seismic response. These findings indicate that near-fault stiffness enhancement is a key factor controlling induced seismic intensity.

6.2 Recommendations

The present study clarified the fundamental role of near-fault fracture stiffness in controlling induced seismicity, but several simplifying assumptions were made in both the numerical models and the laboratory experiments. To further develop the concepts and methods proposed in this thesis, the following topics are recommended for future work:

1. In this study, fracture stiffness was varied independently of pore-pressure evolution, frictional properties, and hydraulic behaviour. Future numerical models should incorporate constitutive laws in which normal and shear stiffness evolve with effective stress level, shear slip, and permeability changes, and should consider more realistic friction laws, including slip-weakening with evolving critical distance or rate-and-state friction. This would allow assessment of how stiffness enhancement interacts with fluid migration, dilation and weakening during induced seismic events.

2. Future experimental work should consider specimens containing more complex and interacting fracture networks, including inclined, non-planar, and spatially variable discontinuities, as well as different loading paths such as cyclic loading. Such experiments would provide deeper insight into the evolution of heterogeneous deformation within damage zones and help bridge the gap between laboratory-scale observations and field-scale fault behavior.

3. It is recommended to explore how the idea of increasing near-fault fracture stiffness can be translated into concrete engineering measures, such as targeted grouting, reinforcement, or other treatments aimed at stiffening critical portions of the damage zone. Combining such measures with microseismic monitoring and, where possible, inversion of apparent damage-zone stiffness could support adaptive control of induced seismicity during mining, fluid injection, or other subsurface operations.

References

Aki K (1966) Generation and propagation of G waves from the Niigata earthquakes of June 16, 1964. II. Estimation of earthquake moment, released energy, and stress–strain drop from the G wave spectrum. Bull Earthq Eng 44:73–88

Agosta F, Alessandroni M, Antonellini M, Tondi E, Giorgioni M (2010) From fractures to flow: A field-based quantitative analysis of an outcropping carbonate reservoir. Tectonophysics 490:197-213

Aki K, Richards PG (2002) Quantitative Seismology. Sausalito. Calif: University Science Books.

Andrews DJ (2005) Rupture dynamics with energy loss outside the slip zone. J Geophys Res Solid Earth 110(B1).

Bachu S (2008) CO2 storage in geological media: Role, means, status and barriers to deployment. Prog Energy Combust Sci 34:254-273

Bandis S, Lumsden AC, Barton NR (1983) Fundamentals of rock joint deformation. Int J Rock Mech Min Sci Geomech Abstr 20(6):249-268

Barton, N., Lien, R., Lunde, J.J.R.M., 1974. Engineering classification of rock masses for the design of tunnel support. Rock Mech 6:189-236

Barton N (1976) Rock mechanics review the shear strength of rock and rock joints. Int J Rock Mech Min Sci Geomech Abstr 13:255-279

Bizzarri A, Cocco M (2003) Slip-weakening behavior during the propagation of dynamic ruptures obeying rate-and state-dependent friction laws. J Geophys Res Solid Earth 108(B8)

Beer W, Jalbout A, Riyanto E, Ginting A, Sullivan M, Collins DS (2017) The design, optimisation, and use of the seismic system at the deep and high-stress block cave Deep Mill Level Zone mine. In: UMT 2017: Proceedings of the First International Conference on Underground Mining Technology:233-245

Berg SS, Skar T (2005) Controls on damage zone asymmetry of a normal fault zone: outcrop analyses of a segment of the Moab fault, SE Utah. J Struct Geol 27:1803-1822

Bickle MJ (2009) Geological carbon storage. Nat Geosci 2:815-818

Blake W, Hedley DGF (2003) Rockbursts: case studies from North American hard-rock mines. SME

Bommer JJ (2006) Control of hazard due to seismicity induced by a hot fractured rock geothermal

project. Eng Geol 83:287-306

Brinkman JR (1987) Separating shock wave and gas expansion breakage mechanisms. In: 2nd international symposium on rock fragmentation by blasting:6-15

Behzadafshar K, Sarafraz ME, Hasanipanah M, Mojtahedi SFF, Tahir MM (2019) Proposing a new model to approximate the elasticity modulus of granite rock samples based on laboratory tests results. Bull Eng Geol Environ 78:1527-1536

Bizzarri A (2011) On the deterministic description of earthquakes. Rev Geophys 49(3)

Bay BK (2008) Methods and applications of digital volume correlation. J Strain Anal Eng Des 43: 745-760

Buljac A, Jailin C, Mendoza A, Neggers J, Taillandier T, Bouterf A, Roux, S (2018) Digital volume correlation: review of progress and challenges. Exp Mech 58(5):661-708

Chester FM, Logan JM (1986) Implications for mechanical properties of brittle faults from observations of the Punchbowl fault zone, California. Pure Appl Geophys 124:79-106

Choi JH, Edwards P, Ko K, Kim YS (2006) Definition and classification of fault damage zones: A review and a new methodological approach. Earth Sci Rev 152:70-87

Cheng G, Li L, Zhu W, Yang T, Tang C, Zheng Y, Wang Y (2019) Microseismic investigation of mining-induced brittle fault activation in a Chinese coal mine. Int J Rock Mech Min Sci 123:104096

De Joussineau G, Aydin A (2007) The evolution of the damage zone with fault growth in sandstone and its multiscale characteristics. J Geophys Res 112:B12

Durrheim RJ (2010) Mitigating the risk of rockbursts in the deep hard rock mines of South Africa: 100 years of research. Extracting the science: A century of mining research:156-171

Dvorsky P, Konicek P (2005) Systems of rock blasting as a rock burst measure in the Czech part of Upper Silesian Coal Basin. In*:* Proceedings of the sixth international symposium on rockburst and seismicity in mines:493-496

Eckert A, Peter C, Liu X (2014) Large-scale mechanical buckle fold development and the initiation of tensile fractures. Geochem Geophys 15:4570-4587

Eftekhari M, Baghbanan A, Bagherpour R (2014) The effect of fracture patterns on penetration rate of TBM in fractured rock mass using probabilistic numerical approach. Arab J Geosci 7:5321-5331

Ellsworth WL (2013) Injection-induced earthquakes. Science 341(6142):1225942

Evans KF, Zappone A, Kraft T, Deichmann N, Moia F (2012) A survey of the induced seismic responses to fluid injection in geothermal and CO2 reservoirs in Europe. Geothermics 41: 30-54

Freed AM (2005) Earthquake triggering by static, dynamic, and postseismic stress transfer. Annu Rev Earth Planet Sci 33(1):335-367

Faulkner DR, Mitchell TM, Jensen E, Cembrano J (2011) Scaling of fault damage zones with displacement and the implications for fault growth processes. J Geophys Res 116:B05403

Fisher NI (1995) Statistical analysis of circular data. Cambridge university press

Foulger, G.R., Wilson, M.P., Gluyas, J.G., 2018. Julian BR, Davies RJ. Global review of human-induced earthquakes. ESR. 178, 438-514.

Fletcher JM, Teran OJ, Rockwell TK, Lynch DK (2020) An analysis of the factors that control fault zone architecture and the importance of fault orientation relative to regional stress. GSA Bulletin 132(9-10):2084-2104

Grigoli F, Cesca S, Priolo E, Rinaldi AP, Clinton JF (2017) Current challenges in monitoring, discrimination, and management of induced seismicity related to underground industrial activities: A European perspective. Rev Geophy. 55(2):310-340

Gábor Somodi, Krupa G, László Kovács, Balázs Vásárhelyi (2018) Comparison of different calculation methods of geological strength index (GSI) in a specific underground construction site. Eng Geol 243

Gudmundsson A, Simmenes TH, Larsen B, Philipp SL (2010) Effects of internal structure and local stresses on fracture propagation, deflection, and arrest in fault zones. J Struct Geol 32:1643-1655

Gutierrez M, Youn DJ (2015) Effects of fracture distribution and length scale on the equivalent continuum elastic compliance of fractured rock masses. J Rock Mech Geotech Eng 7:626-637

Gao F, Yuan G, Liu W, Peng X (2023) Experimental study of strainbursts caused by stress concentration and local mine stiffness decrease as mining proceeds. Rock Mech Rock Eng 56(10):7495-7507

Häring MO, Schanz U, Ladner F, Dyer BC (2008) Characterisation of the Basel 1 enhanced geothermal system. Geothermics 37(5):469-495

Hoek E (2007) Practical rock engineering

Hoek E, Diederichs MS (2006) Empirical estimation of rock mass modulus. Int J Rock Mech Min Sci 43(2):203-215

Hoek E, Brown ET (1997) Practical estimates of rock mass strength. Int J Rock Mech Min Sci 34(8):1165-1186

Hussein AI, Barbone PE, Morgan EF (2012) Digital volume correlation for study of the mechanics of whole bones. Procedia Iutam 4: 116-125

Ikari MJ, Marone C, Saffer DM, Kopf AJ (2013) Slip weakening as a mechanism for slow earthquakes. Nat Geosci 6(6):468-472

Johri M (2012) Fault damage zones–observations, dynamic modeling, and implications on fluid flow. Stanford University

Johri M, Dunham EM, Zoback MD, Fang Z (2014) Predicting fault damage zone by modeling dynamic rupture propagation and comparison with field observations. J Geophys Res Solid Earth 119:1251–1272

Ju W, Hou G, Zhang B (2014) Insights into the damage zones in fault-bend folds from geomechanical models and field data. Tectonophysics 610:182-194

Jost ML, Büßelberg T, Jost Ö, Harjes HP (1998) Source parameters of injection-induced microearthquakes at 9 km depth at the KTB deep drilling site, Germany. Bull Seismol Soc Am 88(3):815-832

Kaiser PK, Mccreath DR, Tannant DD (1996) Canadian Rockburst Support Handbook. Canadian Rockburst Research Program 1990–1995

King GCP, Cocco M (2001) Fault interaction by elastic stress changes: New clues from earthquake sequences. In Adv Geophys 44:1-VIII

Kanamori H, Rivera L (2006) Energy partitioning during an earthquake. Geophys Monogr Ser 170:3-13

Kanamori H (1978) Quantification of earthquakes. Nature 271(5644):411-414

Kang H, Jiang P, Feng Y, Gao F, Zhang Z, Liu X (2023) Application of large-scale hydraulic fracturing for reducing mining-induced stress and microseismic events: a comprehensive case study. Rock Mech Rock Eng 56(2):1399-1413

Konicek P, Saharan MR, Mitri H (2011) Destress blasting in coal mining–state-of-the-art review. Procedia Eng 26:179-194

Konicek P, Soucek K, Stas L, Singh R (2013) Long-hole destress blasting for rockburst control

during deep underground coal mining. Int J Rock Mech Min Sci 61:141-153

Konstantinovskaya E, Rutqvist J, Malo M (2014) CO_2 storage and potential fault instability in the St. Lawrence Lowlands sedimentary basin (Quebec, Canada): Insights from coupled reservoir-geomechanical modeling. Int J Greenh Gas Control 22:88-110

Kozłowska M, Orlecka-Sikora B, Rudziński Ł, Cielesta S, Mutke G (2016) Atypical evolution of seismicity patterns resulting from the coupled natural, human-induced and coseismic stresses in a longwall coal mining environment. Int J Rock Mech Min Sci 86:5-15

Larsson B, Kristina (2004) Mining induced seismicity in sweden. Lule Tekniska Universitet.

Leśniak A, Isakow Z (2009) Space–time clustering of seismic events and hazard assessment in the Zabrze-Bielszowice coal mine, Poland. Int J Rock Mech. Min Sc. 46(5):918-928

Li HB, Zhao J, Li TJ (1999) Triaxial compression tests on a granite at different strain rates and confining pressures. Int J Rock Mech Min Sci 36:1057-1063

Li T, Cai MF, Cai M (2007) A review of mining-induced seismicity in China. Int J Rock Mech Min Sci 44:1149-1171

Li VC (1986) Mechanics of shear rupture applied to earthquake zones

Lin A, Maruyama T, Kobayashi K (2007) Tectonic implications of damage zone-related fault-fracture networks revealed in drill core through the Nojima fault, Japan. Tectonophysics 443:161-173

Liu JP, Xu SD, Li YH, Lei G (2019) Analysis of rock mass stability based on mining-induced seismicity: A case study at the Hongtoushan copper mine in China. Rock Mech Rock Eng 52:265-276

Malek F, Suorineni FT, Vasak P (2009) Geomechanics strategies for rockburst management at Vale Inco Creighton Mine. In: Diederichs M, Grasselli G (eds) ROCKENG09, Toronto

Mirabedini ME, Haghshenas E, Ganjian N (2022) Estimating the Geological Strength Index (GSI) in Regional Seismic-Landslide Zonation Using the Empirical Regression Model. Adv Civ Eng 2022(1):4798523

Mikumo T, Olsen KB, Fukuyama E, Yagi Y (2003) Stress-breakdown time and slip-weakening distance inferred from slip-velocity functions on earthquake faults. Bull Seismol Soc Am 93(1):264-282

Marinos VIII, Marinos P, Hoek E (2005) The geological strength index: applications and limitations. Bull Eng Geol Environ 64(1):55-65

Marinos P, Hoek E (2000) GSI: a geologically friendly tool for rock mass strength estimation. In ISRM international symposium.

Ma J, Dineva S, Cesca S, Heimann S (2018) Moment tensor inversion with three-dimensional sensor configuration of mining induced seismicity (Kiruna mine, Sweden). Geophys J Int 213(3):2147-2160

Ma J, Dong L, Zhao G, Li X (2019) Focal mechanism of mining-induced seismicity in fault zones: a case study of yongshaba mine in China. Rock Mech Rock Eng 52:3341-3352

Majer EL, Baria R, Stark M, Oates S (2007) Bommer J, Smith B, Asanuma H. Induced seismicity associated with enhanced geothermal systems. Geothermics 36:185-222

Matsuki K, Nakama S, Sato T (2009) Estimation of regional stress by FEM for a heterogeneous rock mass with a large fault. Int J Rock Mech Min Sci 46:31-50

Maxwell SC, Zhang F, Damjanac B (2015) Geomechanical modeling of induced seismicity resulting from hydraulic fracturing. Lead Edge 34(6):678-683

McCreary R, McGaughey J, Potvin Y, Ecobichon D, Hudyma M, Kanduth H, Coulombe A (1992) Results from microseismic monitoring, conventional instrumentation, and tomography surveys in the creation and thinning of a burst-prone sill pillar. Pure Appl Geophys 139:349-373

McGarr A (1984) Scaling of ground motion parameters, state of stress, and focal depth. J Geophys Res Solid Earth 89:6969–6979

Mena B, Wiemer S, Bachmann C (2013) Building robust models to forecast the induced seismicity related to geothermal reservoir enhancement. Bull Seismol Soc Am 103(1):383-393

Mitchell TM, Ben-Zion Y, Shimamoto T (2011) Pulverized fault rocks and damage asymmetry along the Arima-Takatsuki Tectonic Line, Japan. Earth Planet Sci Let. 308:284-297

Mutke G, Dubiński J, Lurka A (2015) New criteria to assess seismic and rock burst hazard in coal mines. Arch Min Sci 60(3):743–760

Ma Q, Liu X, Tan Y, Wang R, Xie W, Wang E, Shang J (2024) Experimental study of loading system stiffness effects on mechanical characteristics and kinetic energy calculation of coal specimens. Rock Mech Rock Eng 57(11):9941-9957

Mayeda K, Gök R, Walter WR, Hofstetter A (2005) Evidence for non-constant energy/moment scaling from coda-derived source spectra. Geophys Res Lette 32(10).

Norini G, De Beni E, Andronico D, Polacci M, Burton M, Zucca F (2009) The 16 November 2006

flank collapse of the south-east crater at Mount Etna, Italy: Study of the deposit and hazard assessment. J Geophys Res Solid Earth 114(B2).

O'Hara AP, Jacobi RD, Sheets D (2017) Predicting the width and average fracture frequency of damage zones using a partial least squares statistical analysis: Implications for fault zone development. J Struct Geol 98:38-52

Oda M (1986) An equivalent continuum model for coupled stress and fluid flow analysis in jointed rock masses. Water Resour Res 22:1845-1856

Ohnaka M (2000) A physical scaling relation between the size of an earthquake and its nucleation zone size. Pure Appl Geophys 157(11):2259-2282

Ostermeijer GA, Mitchell TM, Aben FM (2020) Dorsey MT. Damage zone heterogeneity on seismogenic faults in crystalline rock; a field study of the Borrego Fault, Baja California. J Struct Geol 137:104016

Panel ML (2006) The future of geothermal energy. Impact of enhanced geothermal systems [EGS] on the United States in the 21st century. Geothermics 17:881-882

Pan B, Asundi A, Xie H, Gao, J (2009) Digital image correlation using iterative least squares and pointwise least squares for displacement field and strain field measurements. Opt Laser Eng 47: 865-874

Pan B (2011) Recent progress in digital image correlation. Exp Mech 51:1223-1235

Rivera L, Kanamori H (2005) Representations of the radiated energy in earthquakes. Geophys J Int 162(1):148-155

Rubinstein JL, Mahani AB (2015) Myths and facts on wastewater injection, hydraulic fracturing, enhanced oil recovery, and induced seismicity. Seismol Res Lett 86(4):1060-1067

Richardson E (2002). Seismicity in deep gold mines of south Africa: implications for tectonic earthquakes. Bull Seismol Soc Am 92(5):1766-1782

Stein RS (1999) The role of stress transfer in earthquake occurrence. Nature 402(6762):605-609

Scholz CH (1998) Earthquakes and friction laws. Nature, 391(391):37-42

Sainoki A, Hirohama C, Schwartzkopff AK (2020) Dynamic modelling of induced seismicity by using seismic efficiency constraints and a new scaling law for slip-weakening distance. Pure Appl Geophys 177(2):637-659

Sainoki A, Hirohama C (2019) Methodology to Back-Analyze the Slip-Weakening Distance of Induced Seismicity, Considering Seismic Efficiency. ISRM Rock Dynamics Summit. ISRM.

Sainoki A, Mitri HS, Chinnasane D, Schwartzkopff AK (2019) Quantitative energy-based evaluation of the intensity of mining-induced seismic activity in a fractured rock mass. Rock Mech Rock Eng 52:4651-4667

Sainoki A, Mitri HS, Yao M, Chinnasane D (2016) Discontinuum modelling approach for stress analysis at a seismic source: case study. Rock Mech Rock Eng 49:4749-4765

Sainoki A, Mitri HS (2016) Back analysis of fault-slip in burst prone environment. J Appl Geophys 134:159–171

Sainoki A, Mitri HS (2014) Dynamic modelling of fault-slip with Barton's shear strength model. Int J Rock Mech Min Sci 67:155-163

Sainoki A, Mitri HS (2015) Effect of slip-weakening distance on selected seismic source parameters of mining-induced fault-slip. Int J Rock Mech Min Sci 73:115-122

Sainoki A, Schwartzkopff AK, Jiang L, Mitri H (2023) Numerical modelling of spatially and temporally distributed on-fault induced seismicity: implication for seismic hazards. Int J Coal Sci Technol 10:4

Sainoki A, Schwartzkopff K, Jiang L, Mitri HS (2021) Numerical modeling of complex stress state in a fault damage zone and its implication on near-fault seismic activity. J Geophys Res Solid Earth 126:e2021JB021784

Sainoki A, Tabata S, Mitri HS, Fukuda D, Kodama JI (2017) Time-dependent tunnel deformations in homogeneous and heterogeneous weak rock formations. Comput Geotech 92:186-200

Sainoki A, Mitri HS, Chinnasane D (2017) Characterization of aseismic fault-slip in a deep hard rock mine through numerical modelling: case study. Rock Mech Rock Eng 50:2709-2729

Schueller S, Braathen A, Fossen H, Tveranger J (2013) Spatial distribution of deformation bands in damage zones of extensional faults in porous sandstones: Statistical analysis of field data. J Struct Geol 52:148–162

Suckale J (2009) Induced seismicity in hydrocarbon fields. Adv Geophys 51:55-106

Shu J, Jiang L, Kong P, Wang Q (2019) Numerical analysis of the mechanical behaviors of various jointed rocks under uniaxial tension loading. Appl Sci 9(9):1824

Sosna K (2011) Laboratory determination of the mechanical properties of granite rocks. In J Geo-Eng New Horizons:306-311

Su Z, Lu L, He X, Yang F, Zhang D (2020) Recursive-iterative digital image correlation based on salient features. Opt Eng 59:034111-034111

Terzaghi K (1943) Theoretical soil mechanics.

Urban P, Lasocki S, Blascheck P, Do Nascimento AF, Van Giang N, Kwiatek G (2016) Violations of Gutenberg–Richter relation in anthropogenic seismicity. Pure Appl Geophys 173:1517-1537

Urbancic TI, Trifu CI (2000) Recent advances in seismic monitoring technology at Canadian mines. Appl Geophys 45(4):225-237

Vavryčuk V (2005) Focal mechanisms in anisotropic media. Geophys J Int 161(2):334-346

Venkataraman A, Kanamori H (2004) Observational constraints on the fracture energy of subduction zone earthquakes. J Geophys Res Solid Earth 109(B5)

Wang H, Ge M (2008) Acoustic emission/microseismic source location analysis for a limestone mine exhibiting high horizontal stresses. Int J Rock Mech Min Sci 45:720-728

Wagner H (2019) Deep mining: a rock engineering challenge. Rock Mech. Rock Eng 52(4).

Wang Z, Li X, Shang X (2019) Distribution characteristics of mining-induced seismicity revealed by 3-D ray-tracing relocation and the FCM clustering method. Rock Mech Rock Eng 53:183-197

Wang J, Ning J, Qiu P, Yang S, Shang H (2019) Microseismic monitoring and its precursory parameter of hard roof collapse in longwall faces: a case study. Geomech Eng 17(4):375-383

Warpinski NR, Du J, Zimmer U (2012) Measurements of hydraulic-fracture-induced seismicity in gas shales. SPE Prod Oper 27(3):240-252

Wu G, Gao L, Zhang Y, Ning C, Xie E (2019) Fracture attributes in reservoir-scale carbonate fault damage zones and implications for damage zone width and growth in the deep subsurface. J Struct Geol 118:181-193

Yin Y, Zheng W, Tang X, Xing M, Zhang Y, Zhu Y (2022) Test study on failure and energy supply characteristics of rock under different loading stiffness. Eng Fail Anal 142:106796

Yue G, Wang G, Ma F, Zhu X, Zhang H, Zhou J, Na J (2022) Fracture Characteristics and Reservoir Inhomogeneity Prediction of the Gaoyuzhuang Formation in the Xiong'an New Area: Insights From a 3D Discrete Fracture Network Model. Front Earth Sci 10:849361

Yamada T, Mori JJ, Ide S, Abercrombie RE, Kawakata H, Nakatani M, Ogasawara H (2007) Stress drops and radiated seismic energies of microearthquakes in a South African gold mine. J Geophys Res 112(B3)

Zang A, Oye V, Jousset P, Deichmann N, Gritto R (2014) Analysis of induced seismicity in

geothermal reservoirs–An overview. Geothermics 52:6-21

Zang A, Zimmermann G, Hofmann H, Stephansson O, Min KB (2019) How to reduce fluid-injection-induced seismicity. Rock Mech Rock Eng 52:475-493

Zhu JB, Kang JQ, Elsworth D, Xie HP, Ju Y (2021) Controlling induced earthquake magnitude by cycled fluid injection. Geophys Res Lett 48(19):e2021GL092885

Zhao TB, Yin YC, Tan YL (2022) Development of a rock testing system with changeable stifness and its application in the study on the rock failure mechanical behaviour. Chin J Rock Mech Eng 41(9):1846–1857 (in Chinese)

Zou J, Zhang Q, Jiang Y, Jiao YY, Zhu S, Zhang G (2024) Mechanism of hydraulic fracturing for controlling strong mining-induced earthquakes induced by coal mining. Int J Rock Mech Min Sci 181:105840